Broadband Nested Antenna

A thesis submitted in fulfillment of the requirements for
the degree of Doctor of Philosophy

Wei Fu

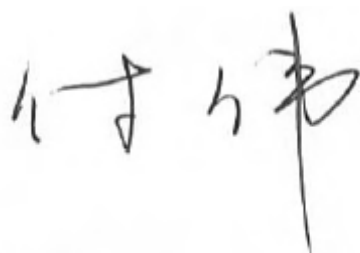(M.Sc.)

School of Electrical and Computer Engineering

RMIT University

2010

Declaration

I certify that except where due acknowledgement has been made, the work is that of the author alone; the work has not been submitted previously, in whole or in part, to qualify for any other academic award; the content of the thesis is the result of work which has been carried out since the official commencement date of the approved research program; any editorial work, paid or unpaid, carried out by a third party is acknowledged; and, ethics procedures and guidelines have been followed.

Wei Fu

28/10/2010

Acknowledgement

To my mother, my father and my son.

Abstract

This thesis investigates a novel dual frequency range low profile antenna system containing two nested spiral antennas operating over 2 – 18 GHz and 30 – 40 GHz respectively. The exploration and development of a broadband microstrip spiral without cavity backing has been implemented in the range of 2 - 18 GHz. The relationship between the structural parameters of equiangular spirals and their performance is investigated by simulating a variety of spiral structures. The input impedance, gain, axial ratio and radiation patterns of spiral antennas on a grounded dielectric substrate are compared with that of a spiral in free space to demonstrate the shortcomings of such a structure (i.e. narrow impedance bandwidth and poor gain).

An effective way to achieve a broad bandwidth is proposed by introducing an impedance profile to remove the residual current along the spiral arms. Initially a Thin Film Resistive Layer (TFRL) was incorporated into a microstrip equiangular spiral antenna to absorb the residual current along the arms. Four spiral antennas with TFRLs of different thickness were developed to explore the TFRL application technique. Measured results and the difficulties in both simulation and fabrication experienced are demonstrated, analysed and addressed.

An alternative to the use of a TFRL as an impedance profile on microstrip spirals, an exploration of spirals with embedded chip resistors had been conducted. The radiation physics of microstrip equiangular spirals are examined in the time domain using the XFDTD simulation package. XFDTD is used to analyse the current density distribution on the spiral arms under the excitation of pulse and harmonic waves. An analysis of the current density distribution at steady state provides guidelines for arranging the chip resistors efficiently. Chip resistor loading rules have been developed from these outcomes. A two dual arm equiangular spiral antennas with embedded chip resistors has been simulated, fabricated and measured. The antenna has a compact tapered balun which is horizontally placed inside the spiral antenna substrate to reduce the volume of the completed spiral/feed structure.

The spiral with embedded chip resistors and a compact balun is selected as the low frequency element (2 – 18 GHz) for a nested antenna system. A dual arm Archimedean spiral antenna with cavity backing (operating over 30 – 40 GHz) is developed to be nested within the aperture of the low frequency spiral. The high frequency antenna was integrated into the substrate of the low frequency element, in the opening between the spiral arms. Electronic Band Gap (EBG) architecture was applied to the rim of the nested antenna substrate to mitigate the consequences of surface waves. The entire nested antenna system was fabricated and measured, and the results are presented and discussed.

Statement of Originality

This thesis demonstrates the original contributions to the integration of the loaded spiral antenna concept using, EBG, thin film resistor, and chip resistor as well as the approach used for analysing radiation physics of microstrip spiral antennas while attempting to solve a practical problem. – The design of a novel compact nested antenna system is also presented.

Firstly, thin film resistive layer which are employed in the microstrip spiral is a novel idea which has not been reported elsewhere. Secondly, chip resistors loaded to the microstrip equiangular spiral arms change the standing wave characteristics of the microstrip antenna and thus achieve 9:1 impedance bandwidth with a reasonable gain.. Thirdly, current distribution analysis on microstrip equiangular spiral antenna was employed as guidelines to optimise chip resistor loading locations. Fourthly, the nesting structure of the antenna system is a novel compact configuration and it has great significance in military and commercial applications in which low profile is advantageous.

Contents

List of Figures

List of Tables

Chapter 2

Chapter 3

Chapter 1 Introduction

1.1 Background

Radar guidance systems may utilise several RF frequency bands. Lower frequencies are used for broad area, long distance scanning [1], while higher frequencies are used once a lock on a particular target is achieved. Millimetre wave frequencies have recently been explored for close range targeting, allowing pin-point accuracy of guided munitions [2]. Therefore, it is crucial that a radar warning receiver be capable of monitoring the complete range of 'threat' signals simultaneously.

Monitoring the full range of threat signals generally requires the use of multiple antennas tuned to the various frequency bands. A conceptual diagram of a receiver and photonic link ('photonic antenna') capable of providing such monitoring is presented in Figure 1.1. The signals from multiple antennas operating over different frequency bands are independently amplified and combined using a broadband RF combiner. These combined signals are then input to a broadband optical modulator and transmitted down an optic fibre. A wide range of possible threat signals must be accommodated in the frequency range from 2 to 18 GHz, as microwave radar systems in this band are in a mature state. Other more specific threats exist at higher frequencies, in the range of 30 – 40 GHz.

In airborne applications, size is of critical importance, so any improvements in the compactness of receiver modules are of great value. This thesis describes the development of such a receiver - photonic antenna system. The objective of the photonic antenna is to integrate two RF antennas and a photonic modulator into one small package which aims to perform over a wide frequency band (preferably 2 – 40 GHz).
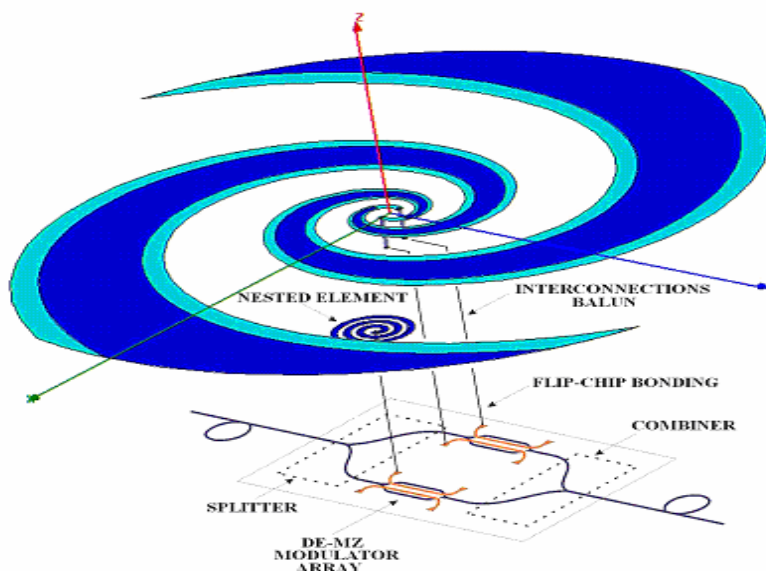
Figure 1.1   The profile of the proposed antenna system for the project

Figure 1.1 shows the schematic of how to achieve these goals. Two RF antennas are required to cover the intended frequency band (2-40GHz) however they work independently over their own frequency range

sharing the exposure face and their receiving signals will be combined through the photonic device underneath. Antenna II, working at high end of 2-40GHz, is about to be nested to the system of Antenna I which covers the low end of the frequency range. This novel nesting configuration of two wideband antennas is advantageous for airborne applications. As a result, the nesting configuration demands Antenna I to be a non-cavity spiral and allow enough space for the nested element- Antenna II. Thus a new feeding structure is required for the non-cavity structure and also the novel structure has to be compatible with the microwave-photonic solution proposed to combine multiple RF signals into a single optic fibre broadband spiral antennas This thesis presents the investigation and development of this photonic broadband antenna system involving with the study of radiation physics of microstrip spiral antennas, simulation, optimisation and fabrication and techniques of microstrip spiral antennas.

1.2 Literature review

The history of antennas dates back to the time when James Clerk Maxwell developed Maxwell's equations in 1897 [3]. Over the last 60 years, antenna research and development has been accelerated by rapid advancement of computer technology, particularly as part of the communication revolution. The following section contains a review of the literature on the development of modern compact broadband antenna design technology, high-frequency electromagnetic problem simulation technology and antenna fabrication techniques.

1.2.1 A brief history of the development of broadband, frequency-independent and spiral antennas

The impedance bandwidth of antennas was not greater than 2:1 until the 1950s when the breakthrough in antenna evolution was made which extended bandwidth to as great as 40:1 or more. The antennas introduced by the breakthrough of expanding bandwidth were referred to as Frequency-Independent (FI) [4-5]. Wideband antennas are finding increased application in the areas of detection of EM interference, signal surveillance, the transmission and reception of short duration pulses, frequency hopping radar systems, and multi-channel discrete frequency communications. The principal broadband radiating elements used to date are spiral antennas, end-fire log-periodic arrays (Vivaldi or microstrip patch [6]), tapered slot line geometries and radial slot lines [7].

Rumsey stated that FI antennas belonged to the class of antenna with shape specified only by angles [8]. It had been shown in theory that if all the dimensions of a lossless FI antenna are increased by a factor K, the pattern and impedance remain fixed if the operating wavelength is also increased by the factor K. The Log-periodic geometry that all the elements of antenna system form, which can be considered as a perturbation of a uniform periodic structure [9], is a typical configuration of FI antenna. A planar equiangular spiral antenna is another form of log-periodic geometry and a FI antenna as well. In theory, an Archimedean spiral is not strictly a FI antenna as it is not specified by any one angle. However, if an Archimedean spiral has many closely spaced turns it is a very close approximation to a tightly wound equiangular spiral [10]. Spiral antennas are widely employed in many industries such as satellite

communication [11], mobile communication [12], Electronic Support Measures (ESM) [13] and medical treatment [14]. More importantly for the purposes of this thesis they have key roles in military applications such as radar direction-finding systems [15], Ground Penetrating Radar (or subsurface radar) [16], unmanned air vehicles [17] and radar imaging [18]. Most are circular spirals but some are square spirals [19]. Spiral realisation can be performed by printing on a substrate [11] or creating slot spiral antennas [20]. In these applications, the spiral antennas usually have multiple arms: such as dual arm [4-5] [13], four-arm [21] and even three-arm [22].

Microstrip spiral antennas belong to the special family which inherits the features from both FI and microstrip antennas, however they tend to suffer from narrow bandwidth, low gain and distorted radiation patterns [23-24]. Nevertheless, the studies were focused on increasing bandwidth, improving antenna gain [25] and mitigating distortion in radiation patterns had accelerated the use of microstrip spiral antennas [26], and even wireless systems such as terrestrial communications, satellite communications and radar with [7].

1.2.2 Radiation physics of spiral antennas and microstrip spiral antennas

The scaling characteristic of FI antennas ensures that their performance is independent of frequency [8]. To make infinite structures more practical, the designs usually require that the current on the structure decreases with distance from the input terminals. After a certain point the current is negligible, and the structure beyond that point to infinity can be truncated and removed. Practically, then, the truncated antenna has a lower cut-off frequency above which its radiation characteristics are the same as those of the infinite structure. The lower cut-off frequency is that for which the current at the point of truncation becomes negligible. The upper cut-off is limited to frequencies for which the dimensions of the feed transmission line cease to look like a 'point' (usually about 1/8 of the wavelength at the highest desirable frequency) [3]. In other words, the inner radius R_{in} and outer radius R_{out} of a spiral determines the upper and lower limit of its operation frequency range [5].

$$
\begin{aligned}
R_{in} &= \frac{\lambda_H}{2\pi} = \frac{c}{2\pi f_H} \\
R_{out} &= \frac{\lambda_L}{2\pi} = \frac{c}{2\pi f_L}
\end{aligned}
\tag{1.1}
$$

In free space, the travelling current on spiral arm decays gradually and its phase changes progressively along the arm. From the centre of the spiral until the rim of the circle which is called the first active zone, the travelling current decreases greatly and its phase changes by 2π. In the far zone the radiated field is mainly contributed by the current within this first active zone, therefore when designing a spiral its maximum length is usually determined according to the designed frequency range.

In free space, when a spiral is in self-complementary structure it has stable impedance characteristics depending on the number of arms and its working mode [27]:

3

$$Z_{0m} = \frac{\frac{\eta_0}{2}}{\sin\left(\frac{m\pi}{N}\right)} \qquad (1.2)$$

m denotes the eigenvalue or characteristic mode (m=1,2,…N-1) and N is the number of arms of the structure.

Huffman and Cencich extended the theory to non-complementary planar N-fold symmetric antennas at various modes [28]. For the dual arm Archimedean spiral with non-unity arm-to-gap width ratio w/g, which is a non-complementary planar antenna like, its Z_0 is a function of w/g.

In many applications the spiral antenna is required to radiate to one side only. The conical spiral [29] solved the bidirectional radiating problem at a cost of extra volume. Another effective solution was to place a conducting reflector or cavity on the back of the antenna. Although a spiral can easily achieve broad bandwidth, even up to 100:1, its impedance bandwidth and radiation performance may not be retained. Nakano attempted [30] to describe the theoretical radiation characteristics of a spiral antenna with a conducting reflector, and his findings were cited repeatedly by subsequent researchers. Analysis of current distribution on a spiral is an effective way to predict far-zone radiated field distribution, gain and polarisation characteristics. In Nakano's study, numerical analysis of the performance of an Archimedean spiral antenna showed that his spiral backed by a plane reflector had two distinct regions of current distribution, which explained the radiation of a circularly polarised wave for the outer circumference, C, ranging over about 1.3λ<C<1.5 λ and C>2.9 λ (λ is a free-space wavelength). Further consideration was given to a truncated spiral antenna with C in the order of 1.4 λ. Nakano's truncated spiral antenna maintained a decaying current distribution and radiated a circularly polarized wave over a 1:1.2 frequency bandwidth. This study also revealed that reflectors may significantly limit the bandwidth of impedance, axial ratio and cause deterioration in radiation characteristics due to coupling between currents on the real spiral and its image in ground plane. Therefore designs of spirals backed by a cavity have been attracting attention and that design technology is now very mature. In early incarnations the cavity was required to be a quarter of a wavelength deep and filled with microwave absorber so that it suffered 50% energy loss and was very large. Later designs have lower volume by adopting thinner [31] or stepped cavities [32-33]. One of the thinner-cavity designs increased the axial gain about 3dB at 4 GHz as well as improved the axial ratio [34].

A broadband (2 – 18 GHz) cavity-backed Archimedean spiral antenna has been comprehensively analysed [33]. The radiation mechanism of the spiral is visualised by observing the current distribution on the spiral arms for both pulsed and harmonic excitation modes. This method provides deeper insight into the radiation mechanism on the spiral antenna, including the coupling effect between windings and the influence of the thin substrate. When the spiral is excited with a single pulse, broadening of the pulse representing frequency dispersive behaviour is explained as the energy associated to a certain frequency component is radiated from a ring-like region with a circumference approximately equal to a full wavelength. Higher frequency components are radiated from regions located closer to the feed than lower frequency components. Besides the propagation of currents along the spiral arms, mutual coupling

between the adjacent windings of the spiral represents another propagation path on the spiral, in the radial direction. This becomes apparent in the oscillations (ringing) that extend to the outer windings of the spiral.

The Spiral-Mode Microstrip Antenna (SMM), invented by Wang in 1989 [26], is a special configuration of a spiral with a cavity that features reliability and low Radar Cross Section (RCS). The SMM antennas are finding applications in various commercial and military systems, such as ELINT (Electronic Intelligence Gathering), CNI (Communications, Navigation, and Identification), Radar Warning Receivers (RWR), ESM. It is a hybrid of two mature antenna types: the microstrip patch antenna and the cavity-backed FI antenna. Its structural geometry is simple - a spiral about 1/10 of a wavelength above ground plane with the absorbing rings at the open end of the spiral arms. In particular, the half-power bandwidth of the peak gain is about 6:1 and the impedance and pattern bandwidth performance is better than 10:1. Usually, radiation modes 0, 1 and 2 are the dominant modes and these are exploited in many applications. Figure 1.2 shows the theoretical unidirectional radiation patterns of spiral at these different modes [36]. Mode 1, the main beam is directed to broadside and most of the radiation occurs near a circle around the centre of the spiral with circumference of about one wavelength (This circle is called the first active zone), was described in [26], [13]. Mode 0 [36] and mode 2 [31] are similar. In either mode, there is a null in the normal direction and two symmetric tilt lobes. However, the implementation of an antenna operating in mode-0 experiences lower loss and cost than that in mode 2 [36].
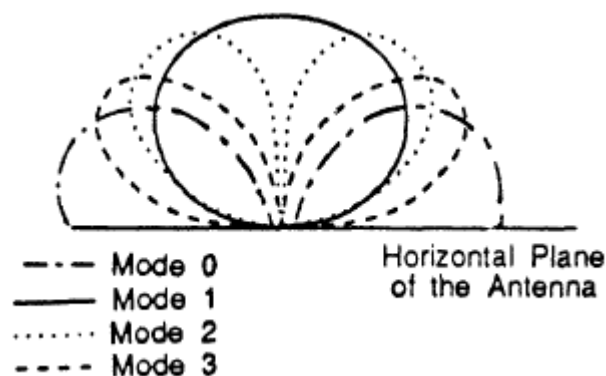
Figure 1.2 Theoretical radiation patterns (source: [36])

Microstrip or printed spirals are heavily researched due to the demands for antennas with low profile conformal configurations in many industries, such as the automotive and aerospace. Due to the presence of a grounded dielectric material, the previously travelling-wave type spiral may change to a resonating antenna [37] leading to a narrow impedance bandwidth. One way to expand bandwidth is to remove the standing wave characteristics by introducing resistive loading profile [39] to absorb residual current so that the flowing current decays to zero before it reaches the end of the spiral. An Archimedean spiral with chip resistors loaded every 90° along its arm, which can achieve 9:1 bandwidth but will suffer low gain [39].

The Z_0 of any planar self-complementary structure on substrate can be expressed using Brooker's relation [21]:

$$Z_0 = \frac{\eta_0}{2\sqrt{\varepsilon_{eff}}} \qquad\qquad (1.3)$$

η_0 is the wave impedance in free space and ε_{eff} is the effective relative permittivity which equals to $(\varepsilon_r+1)/2$ when half of the space is filled with the dielectric material. In practice, the thickness of dielectric material h is finite but there is still approximate expression for Z_0. When g/h (the ratio of the gap width g of the spiral arm to h) at the feeding point is small the real part of impedance converges to the expected value of a self-complementary structure in a half-space of dielectric. The Z_0 decreases when ε_r increases.

When on grounded dielectric substrate, if h is small enough compared to wavelength of lowest frequency of the interested frequency range, the ground plane underneath changes electric field distribution on the spiral and the spiral shows standing wave characteristic thus the impedance bandwidth decreases significantly. In addition to changing the Z_0 of spiral, grounded dielectric substrate also dramatically changes its radiation pattern shape and HPBW, the power level of the main lobe and side lobes, and directivity and polarization properties [40]. In fact, so far there are no generalized expressions of radiated field distribution like those for the microstrip patch antenna [41].

In this research, a nested antenna operating over the 30 – 40 GHz band is integrated into the system. Most radars working at Ka band (24 – 40 GHz) are used for mapping, short range or airport surveillance. The radiation efficiency of a microstrip antenna deteriorates almost by 15% as the frequency rises from C band (2-4GHz) to X band (8-12GHz) [42] caused by dielectric loss and surface wave. Although for much higher frequency ranges the degree of the radiation efficiency deterioration for a microstrip antenna has not yet been quantified [42], the relevant losses at frequencies ranging from 30 to 40 GHz are expected as following: conductor losses are around 0.15 to 0.2 dB per wavelength, dielectric losses are around 0.04 to 0.05 dB per wavelength for a 50 ohm line on a 10 mil Roger Duroid substrate with ε_r=2.2 [43]. Thus radiation efficiency or antenna gain of microstrip element working on this frequency range should be an issue. One of the solutions is to develop a premium microstrip antenna array with optimised feeding network. However, in this research wide radiation beamwidth is required for Antenna II. Thus single microstrip spiral on thin substrate should be the preliminary design. Unfortunately there are very few publications about this topic. Nevertheless, the recognition of the common issues with millimetre wave such as losses caused by discontinuities, surface wave, and bends [44] helps to initiate the design of Antenna II.

1.2.3 Antenna analysis methods

In the 1960s, antenna analysis for complex practical cases like an Archimedean spiral was very difficult. Eventually 'band theory' extracted from the experimental observations became capable of explaining the radiation physics of Archimedean type spiral antennas. Numerical analysis of antennas has been advancing ever since and the radiation physics of Archimedean type spiral antennas are now well known. One analytical method is the integral equation method. The solution for the unknown current density which is induced on the surface of the radiator is cast in the form of an integral equation where the unknown induced current density is part of the integrand. The integral equation is then solved for the unknown induced current density using numerical techniques such as Method of Moment (MOM) [49-50].

In practice, integral equation method may be combined with other theory or techniques. For example, PO-MOM (physical optics MOM) hybrid method is used to analyse large and complex geometries. Theory of Maxwellian Circuits (TMC) is implemented to solve the integral equation, and is more efficient than conventional full matrix solutions without any accuracy sacrifice [52]. Once current density distribution on an antenna is known all the other performance parameters may be calculated such as far zone electric field, antenna gain and axial ratio if it is a circularly polarised antenna.

Another method is to solve the differential form of Maxwell's equations, such as FDTD (Finite Differential Time Domain), FEM (Finite Element Method) and FVTD (Finite Volume Time Domain). These techniques do not use Green's functions, so they are well suited to take into account the effect of finite-sized ground planes and substrates. For instance, FVTD modelling was used to predict the current density distribution on a spiral backed by the cavity [53]. B-spline FEM showed that the printed Archimedean spiral antenna displayed standing wave characteristics [38]. FDTD analysis for the radiation pattern and input impedance of a printed dual arm square spiral antenna displays its feasibility for the design and performance evaluation of this class of antennas [53].

1.2.4 Other relevant technology

In microstrip antennas, surface wave activity is of primary interest since the fundamental transverse magnetic (TM_0) surface wave mode has zero cut-off and may be present at all frequencies. The next higher surface wave mode is the fundamental transverse electric (TE_1) mode with a cut-off frequency usually in the high GHz range. In general the cut-off frequencies fc of TM and TE modes on a grounded dielectric substrate of height h and relative permittivity ε_r can be calculated by [55?]:

$$f_c = \frac{nc}{4h\sqrt{\varepsilon_r - 1}} \tag{1.4}$$

where c denotes the speed of light, and n is the mode number which is odd such as 1, 3, 5 for TE_n waves and even for TM_n modes such as 0, 2, 4.

The spurious free space radiation is given particular attention in previous studies of printed circuit antenna performance [52-53]. In Schuster and Fichtner's study of backscattering of TM_0 surface wave using FDTD [53], the dispersion characteristics were calculated from FDTD results. The surface waves are partly scattered back and partly radiated from the truncations and the reflection coefficient of TM_0 wave scattered at the truncation was predicted. This study also revealed there is a frequency threshold at which surface wave mode changes its behaviour from quasi plane wave to "trapped" in substrate. The value of this threshold depends mainly on permittivity of the substrate.

Due to the propagation and scattering characteristics of surface waves in a dielectric material, the efficiency of a planar antenna in dielectric substrate reduces and the undesired coupling between the proximity antennas may be produced if an antenna array needs to be considered. In addition, because of scattering and radiating at the truncations, surface waves may distort the radiation patterns of the microstrip antenna. A popular solution is to employ an electromagnetic band-gap (EBG) [54] or photonic band-gap (PBG) structure [55] to stop the propagation of the surface wave. An EBG array forms a perfect

magnetic conductor with a high impedance surface for electric fields over a narrow bandwidth due to its periodic combination of capacitance and inductance. The traditional EBG configuration is an array of probes and patches [56] in which the probe act as inductor and patch forms a capacitor with the ground plane. The EBG performance range has been extended by using microstrip-based elements - spiral inductors and inter-digital capacitors connected through transmission lines to provide a wide, higher order surface wave suppression band [57]. Practically EBG structures have been employed to suppress the propagation of surface waves and improve radiation pattern of the Archimedean spiral antenna [58].

PBG structures [59] have been used as a reflector for spiral antennas to enhance the directive gain and to suppress the surface wave mode. Periodic dielectric structures (PBG crystals) have been developed in which electromagnetic wave propagation in any direction is completely prohibited for all frequencies within a stop band [60].

The PBG crystal has immense potential in improving the performance of antennas and antenna arrays especially at higher millimetre wave frequencies. The perfectly reflecting and dissipationless properties of the PBG crystal eliminate the problem of radiation losses of a planar antenna mounted on a dielectric substrate, and provide an enhancement of the radiation intensity of directional antennas and antenna arrays [55].

A chip resistor loading technique is often employed in the designs of microstrip antennas to optimize their performance characteristics, such as enhance bandwidth, reduce the antenna size [61] and improve axial ratio [62]. An axial ratio of 6.7 dB for the open arm ends of the Archimedean spiral antenna is improved to 2.0 dB with resistive load terminations [63]. The absorbing rings placed at the end of both arms of the spiral-mode microstrip antenna [26] absorb residual current by introducing ohmic loss to the antenna and change current distribution on the antenna. This is the same working mechanism as that of chip resistors.

1.3 Organisation of thesis

In Chapter 1 this thesis begins with a review of the history, design technology and practical applications of frequency-independent antennas, spiral antennas and microstrip antennas as well as surface wave suppression and resistive loading techniques. The novel dual frequency range low profile antenna system proposed contains two nested spiral antennas, and is designed to operate at 2 – 18 GHz and 30 – 40 GHz. To realise the low profile antenna system, research has been focused on investigation and development of microstrip spiral without cavity covering the 2 - 18 GHz range.

Chapter 2 starts from the specifications of the two RF spiral antennas. The relationship between the structural parameters of equiangular spirals and their performance is investigated by simulating many different spiral structures. The frequency responses of input impedance, gain, axial ratio and radiation patterns of the spiral antennas on dielectric material and grounded substrate are compared with that in free space and demonstrate the drawbacks such as narrow impedance bandwidth and poor gain of microstrip spirals. However, an effective way is to remove the residual current along the spiral arms to achieve intended bandwidth by introducing an impedance profile. Initially a Thin Film Resistive Layer (TFRL)

was incorporated into the microstrip equiangular spiral antenna to absorb the residual current along the arm. Four spiral antennas with TFRL of different thickness are developed to explore TFRL application technique. The measured results and the difficulties in both simulation and fabrication experienced are demonstrated, addressed and analysed.

Chapter 3 describes the exploration of equiangular microstrip spiral antennas with embedded chip resistors. The radiation physics of microstrip equiangular spirals are examined in the time domain using the XFDTD simulation package to analyse the current density distribution on spiral arms under the excitation of pulse and harmonic waves. The analysis of the current density distribution at steady state provides guidelines for arranging the chip resistors efficiently. Chip resistor loading rules have been developed from these outcomes. A spiral loaded by one pair of chip resistor has been developed to validate chip resistor simulation and repeatable fabrication. Based on the chip resistor loading and a tapered balun design technique, two dual arm equiangular spiral antennas with embedded chip resistors have been simulated, fabricated and measured. The second fabricated antenna has a compact tapered balun which is horizontally placed inside the spiral antenna substrate. The spiral with compact balun is selected as Antenna I for the nested antenna system.

Chapter 4 explains the design of Antenna II (operating over 30 – 40 GHz) as well as how the nested antenna system is designed. The dual arm Archimedean spiral with cavity is developed based on the study of its structural parameters. The integration proposal of Antenna I and Antenna II as well as all other facilities including baluns has been simulated and optimised. Electric band gap (EBG) technology is also applied to the system to mitigate surface wave issue. The entire nested antenna system has been fabricated, measured and the measured results are presented and analysed.

Chapter 5 summarises the thesis and outlines avenues for further work based on its outcomes.

Chapter 2 Low profile microstrip spiral antennas

2.1 Introduction

The aim of this research called for two circularly polarised broadband antennas operating as one low profile warning radar receiver monitoring the complete range of 'threat signals' in the range of 2 – 40 GHz. These two antennas are to be arranged as a 'nested' structure in order to achieve the goal of low profile. One antenna - a dual arm equiangular spiral, which is supposed to operate at low end (2 - 18 GHz) of the specified frequency range, is a potential option as it allows enough exposure space for a nested antenna- the other antenna- performing over high end (30 – 40 GHz). The specifications of these two antennas are listed in Table 2.1.

Table 2.1   The specifications of the two antennas

Specification	Desired parameter value	Minimum parameter value
Frequency range	2 – 40 GHz	Dual band: 2 – 18 GHz (Antenna I) 30 – 35 GHz (Antenna II)
Beamwidth (3dB)	120º	110º
Gain	+2 dBic	0 dBic
VSWR	2:1 (MAX)	2.5:1(MAX)
Axial Ratio	< 1 dB on axis < 3 dB max at ± 60º	< 2 dB on axis < 4 dB max at ± 45º
Polarisation		RHCP or LHCP
Dimension	100 mm*100 mm*20 mm	

In addition to these criteria of radiating performance and dimension, the proposed antenna system was required to radiate towards one side.

Based on the specifications the proposed Antenna I is a dual arm equiangular spiral on a grounded dielectric substrate operating over 2–18 GHz and there is enough space between its arms for exposing Antenna II. This chapter is focused on the investigation into the key structural parameters of a dual arm equiangular spiral and how they are associated with the radiation performance of the spiral.

2.2 Structural parameters

The dual arm equiangular spiral antennas shown in Figure 2.1 (a) and (b) are planar logarithmic spirals and their curves are defined by (2.1):

$$\rho_1 = \rho_0 e^{a(\phi-\phi_0)} \quad \phi_0 \leq \phi \leq \phi_{ed}$$
$$\rho_2 = \rho_0 e^{a(\phi-\phi_0-\delta)} \quad \phi_0 \leq \phi \leq \phi_{ed} \qquad (arc\ truncation) \hspace{2cm} (2.1)$$
$$\phi_0 \leq \phi \leq \phi_{ed} + \delta \quad (straight-line\ truncation)$$

(a)   (b)
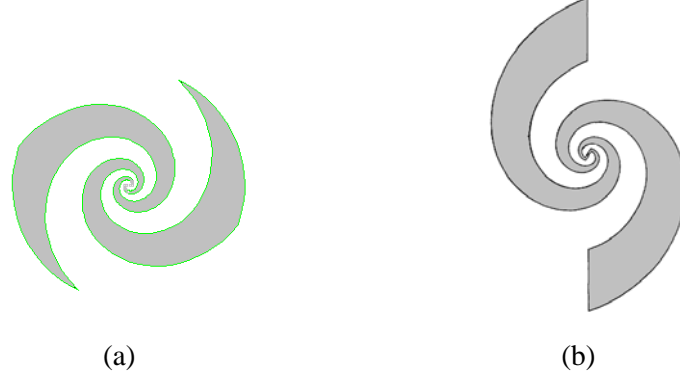
Figure 2.1   Planar equiangular spirals with external truncation (a) of arc (b) of straight line

Where ρ and ϕ are the conventional polar coordinates: ρ_1, ρ_2 are the radial distances from the origin in the direction given by the angle ϕ on both curves which varies from ϕ_0 (staring angle) to ϕ_{ed} (ending angle) or $\phi_{ed}+\delta$; a is a positive constant describing expansion rate of the spiral; δ is the angle of one of the two log–spiral curves rotate through and ρ_0 is the inner radius of spiral. The truncations at both ends determine the upper and lower limit of the frequency range [f_L, f_H] as following according to 'band theory' [4]:

$$R_{in} = \frac{\lambda_H}{2\pi} = \frac{c}{2\pi f_H}$$
$$\hspace{8cm} (2.2)$$
$$R_{out} = \frac{\lambda_L}{2\pi} = \frac{c}{2\pi f_L}$$

R_{in}, R_{out} are inner and outer radius of a spiral when the spiral is working within the frequency range [f_L, f_H]. In this case, $R_{in}=\rho_0$ and $R_{out}=\rho_1(\phi_{ed})$. Thus the intended frequency range limits the value range of ρ_0, ϕ_0 and ϕ_{ed}. When δ is equal to 90º, the equiangular spiral is a so-called self-complementary structure which may achieve the consistent characteristics impedance and better circular polarisation [38] over a wide frequency range in free space. Dyson [4] concluded that the equiangular spirals with 1.25 - 1.5 turns and an expansion rate meeting $0.2 < a < 0.5$ would achieve better radiation patterns. However, Antenna I is proposed as a microstrip spiral antenna whose performance may be relevant to with these basic structural parameters in a more complex way. Under the specifications of this project, it is essential to find out how ground dielectric substrate affects antenna parameters (input impedance and its directional characteristics, including gain, polarisation and radiation beam) thus thickness and permittivity ε_r of substrate should also be taken into account. In this chapter, the investigation starts from studying the spirals in free space and concludes with the microstrip spirals.

2.2.1 In free space

For any spiral in free space, at any frequency within the operating frequency range there is a circle with circumference equal to one wavelength can be defined, and called the first active zone [5]. The travelling current decays gradually along the spiral arm and its phase changes progressively. From the centre of the spiral until the rim of the circle, the travelling current decreases greatly and its phase changes 2π. Therefore, in the far zone the radiated field is mainly contributed by the current within this first active zone.

In free space, the following expression shows the relationship between the characteristic impedance Z_0 and Z_r [30]:

$$Z_0 \cdot Z_r = \frac{\eta_0^{\;2}}{4} \tag{2.3}$$

Z_0 is the characteristic impedance of the planar metallic object and Z_r is the characteristic impedance of the rest of plane. η_0 is wave impedance in free space which is 377 Ω.

Equation 2.3 can be used to describe the relationship between Z_0 and Z_r of the dual arm spirals displayed in Figure 2.1. When the spiral is rotated along the normal axis by 90° its two arms would almost cover the previous blank space. This structure is called self-complementary and in this case Z_0 roughly equals Z_r. Therefore from Equation 2.3, Z_0 of the dual arm spiral is about 188.5 Ω.

The initial values of the three parameters of Antenna I were determined to ensure enough space between the spiral arms for Antenna II. They are: a=0.35, ρ_0=0.508 mm and δ=90° and different ϕ_{ed} which changed from 360° (1 turn) to 720° (2 turns) every 45°. Figure 2.2 displays the real and imaginary parts of the input impedance of the spiral models with ϕ_{ed} changing from 360° (1 turn) to 720° (2 turns). From 2 GHz to 10 GHz, most of the spiral models show evident resonance - e.g. at resonance frequency, f_r, the real part of input impedance is very high and its imaginary part is close to 0. Also f_r gradually becomes lower as the length of spiral increases. When ϕ_{ed} is 675°, the frequency response of the real part of the input impedance is very flat and it approaches 174 Ω as frequency increases. Accordingly, in Figure 2.2 (b) when ϕ_{ed} is 675° the variation line of the imaginary part of the input impedance is nearly a straight line as well. While the frequency is between 8 GHz and 18 GHz, the reactance value remains stable around 0. As mentioned above, a typical feature of self-complementary frequency-independent (FI) antenna has consistent characteristics impedance which is a pure resistance of about 188.5 Ω. Therefore, the spiral model with ϕ_{ed} =675° can be labelled a self-complementary FI antenna. This implies that while a spiral may be long enough to make the resonant frequency move out of the intended frequency range; if so it becomes a travelling wave antenna. To produce more information about this boundary of length, ϕ_{ed} was varied between 630° and 675° with steps of 5°. While ϕ_{ed} was 660°, the impedance locus of the spiral at any frequency within 2–18 GHz were all located within in the circle $|\Gamma|=1/3$ in smith chart (normalised to Z_0=177 Ω), as seen in Figure 2.3, this impedance locus represents S_{11} of the spiral was below –10 dB for all the frequencies within the range 2-18 GHz when it was fed with 177 Ω. The progressive length of each

arm of the spiral was about a half of the wavelength at 2 GHz (λ_{2GHz}). Thus it can be concluded that in free space a dual arm spiral started to act as a travelling wave antenna only when its total length exceeded half of the wavelength at the lowest frequency of the intended frequency range.
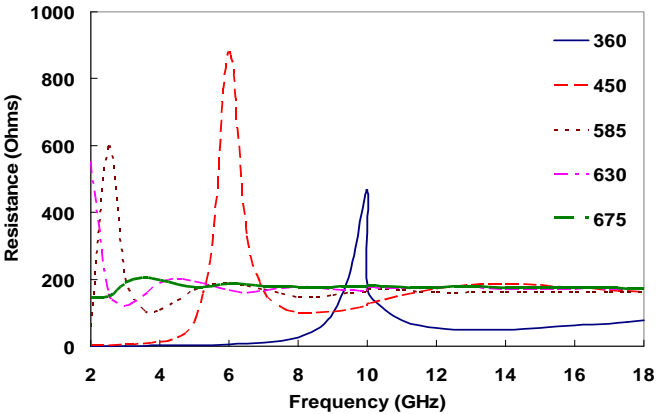
(a)
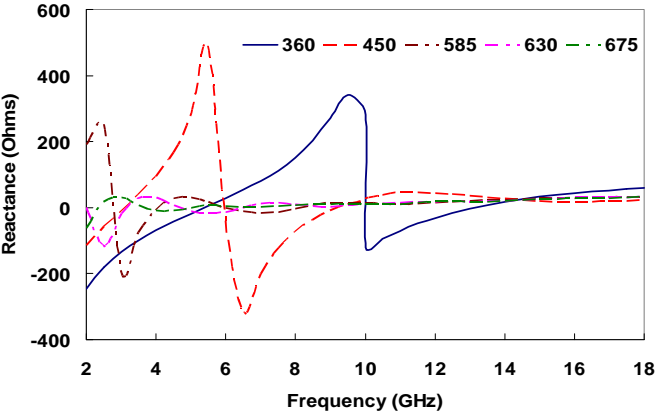
(b)

Figure 2.2   Input impedance of the spirals with varying ϕ_{ed} in free space (a) resistance (b) reactance
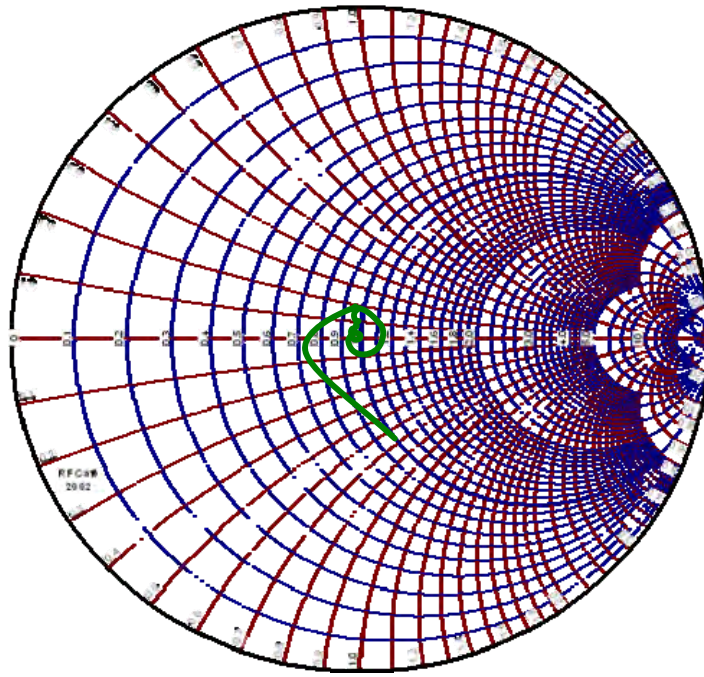
Figure 2.3   Input impedance of the spiral with $\phi_{ed} = 660°$

(a)   (b)
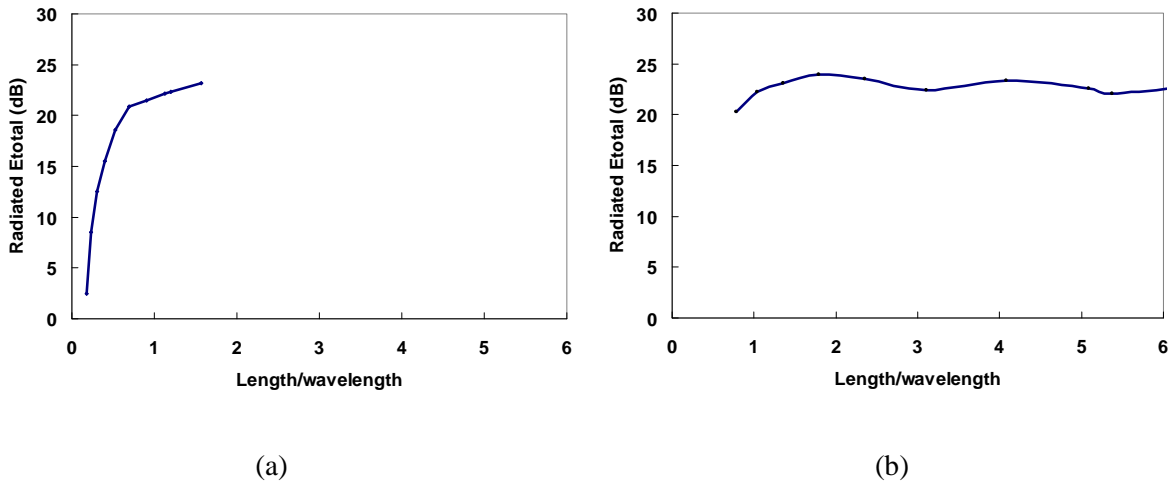
Figure 2.4   Far zone total radiated field E_{total} (dB) vs L/λ_0 at $\phi = 0°$ $\theta = 0°$ of the spirals with varying length (a) at 4 GHz (b) at 18 GHz

Figure 2.4 summarises the simulated total radiated electric field E_{total} ($\phi = 0°$, $\theta = 0°$) (dB) of the spirals with $\phi_{ed} \sim$ [360°, 720°] within which each sample was taken every 5°. It can be seen that in free space the level of the radiated field along the maximum radiation direction varied versus the ratio of spiral length to the wavelength. When the total length of the spiral increased up to ½ λ_0 of any particular frequency the strength of its radiated field increased linearly. In Figure 2.4 (a), when L/λ_0 changes from 0.17 to 0.7, the magnitude of total electric field E_{total} increases from 2 dB to 21 dB. In both (a) and (b), when L/λ_0 varies from 0.7 to 2, E_{total} continues growing but at a slower rate and it increases by 3 dB when reaching

14

maximum at $L/\lambda_0 \approx 2$. The increment of spiral length L/λ_0 beyond 2 does not increase the radiated power any further.

Figure 2.4 reveals how radiated electric field changed with L/λ_0. While the total length is above $1\lambda_0$ its radiated electric field E_{total} (ϕ =0º, θ=0º) changed every $3\lambda_0$ and the ripple was about 3 dB. In order to show the detailed radiation pattern which contains the radiated power at other azimuth angle θ, several plots are shown in Figure 2.5 in which "1 lambda", "2 lambda", "3 lambda" denote the spiral with length of $1\lambda_0, 2\lambda_0, 3\lambda_0$.

(a)   (b)
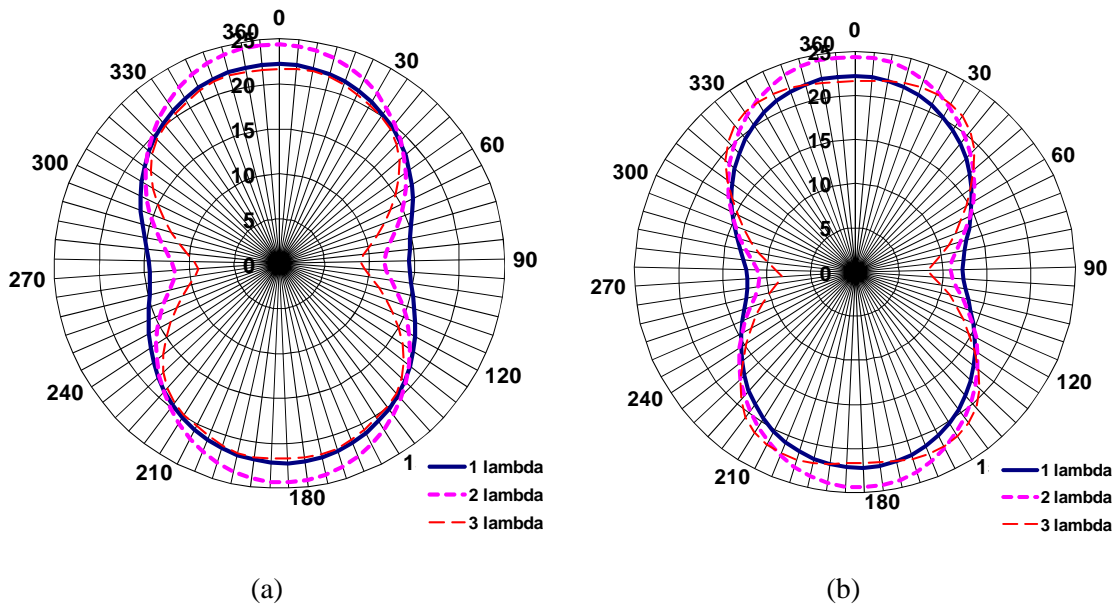
Figure 2.5   Far zone E_{total} versus θ of a $1\lambda_0, 2\lambda_0, 3\lambda_0$ long spiral in free space (a) ϕ=0º (b) ϕ=90º

In free space the spiral radiates to both sides of the spiral plane symmetrically, as seen in Figure 2.5, and the radiation patterns contain two identical main beams directing at θ = 0º and 180º. The bore-sight radiated field of the spiral with length of $2\lambda_0$ is about 3 dB higher than that of $1\lambda_0$ or $3\lambda_0$. In addition, at end-fire direction radiation of the $1\lambda_0$ case is stronger than that of $2\lambda_0$ or $3\lambda_0$ by 3-5 dB in both ϕ cut planes. Figure 2.5 shows that the progressive length *L* of the spiral changes the strength of far zone radiated electric field and shape of radiation beam insignificantly.

The next criterion for evaluating performance of a circularly polarised antenna is axial ratio. In free space a spiral antenna usually has low axial ratio. Figure 2.6 demonstrates the generalised pattern of the axial ratio of the spirals with varying ϕ_{ed} when their total lengths are normalised by the wavelength in which (a) is for 4 GHz and (b) for 18 GHz.

(a)   (b)
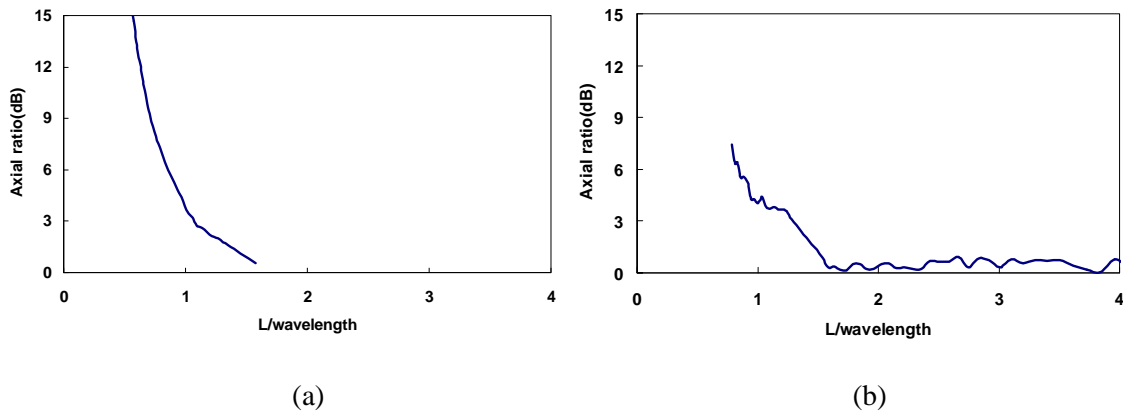
Figure 2.6   Axial ratio of the spirals with $\phi_{ed} \sim [360°, 720°]$ vs. L/λ_0 at (a) 4 GHz (b) 18 GHz

Figure 2.6(a) displays when L/λ_0 changes from 0.7 to 1, the axial ratio drops dramatically until it reaches 3 dB (when L/λ_0 is between 0 and 0.5 the axial ratio has enormously high value - in excess of 40 dB - hence it is not shown). When L/λ_0 changes from 1.1 to 1.5, the axial ratio of the spiral reduces slowly. Figure 2.6 (b) also shows similar pattern at 18 GHz. From the axial ratio patterns it can be concluded that in free space when the progressive length of a dual arm equiangular spiral reaches 1.3 wavelengths at the lowest frequency its axial ratio would go below 3 dB which means the spiral has a good circular polarisation.

The investigation described above was particularly focused on the set of spirals with constant expansion rate *a* but varying ϕ_{ed}. A change in *a* has been considered and studied. Generally when *a* is much more than 0.35 the spiral expands outward rapidly. As concluded above, the consistent input impedance only can be reached when the progressive length exceeds half of the wavelength for lowest frequency of the range. According to the specification of the two RF antennas the outer radius of Antenna I should not exceed 50 mm. Thus the requirement of spiral length and the restriction for outer radius determined what range *a* should be within. In addition, the requested exposure space between arms of Antenna I for nested Antenna II narrowed this range further. Eventually *a* = 0.35 was determined.

2.2.2 Microstrip spiral

Generally a thick substrate has advantages over a thin one such as stronger mechanical support and improved impedance bandwidth in a microstrip antenna. However, it also contributes extra weight and more dielectric loss, surface wave loss and extraneous radiations from probe feeds [41]. For 3.175 mm thick Rogers RT/Duroid 5880 (ε_r=2.2) substrate, the TE_1 mode surface wave may be excited at 21.5 GHz, and for 1.574 mm thick material it occurs at 43.5 GHz. Because the TM_0 has zero cutoff frequency, it will be always excited at the open end of the microstrip antenna. It is impossible to avoid the TM_0 surface wave, however, it is still necessary to select thinner substrate for purpose of avoiding higher modes of surface wave.

16

Besides thickness, the relative permittivity ε_r also affects the radiation performance of a microstrip antenna. For example, in the case of a microstrip patch antenna a substrate with lower relative permittivity ε_r increases the fringing field at the patch periphery and then strengthens its radiated power. Relative permittivity ε_r of a material determines modes of surface wave excited on the substrate, as seen in Figure 2.7. This diagram (cited from [64]) gives the list of TE/TM mode surface waves possible in the substrate with respect to thickness (normalised by wavelength) for substrates with three different ε_r. It can be observed that thicker substrate or substrate with higher ε_r is likely to induce more modes of surface waves. For a microstrip spiral, low ε_r is preferred if it is required to mitigate the surface waves.
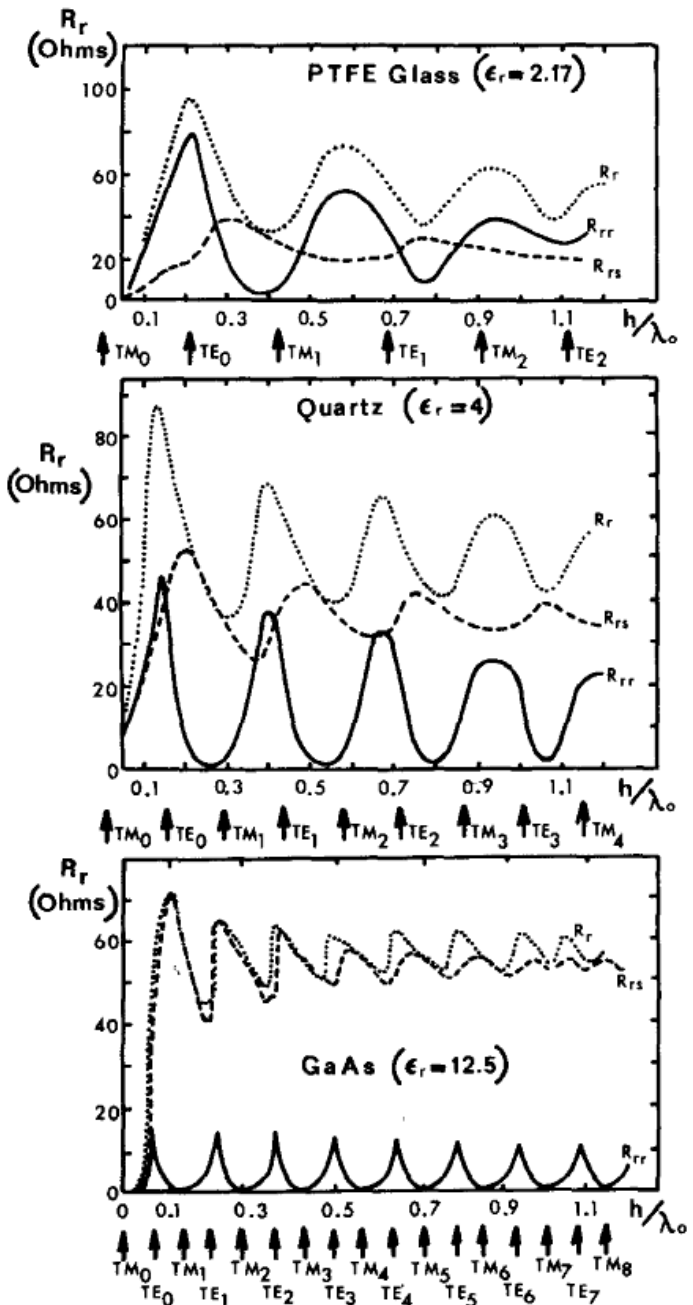
Figure 2.7   Diagram of TE_1,TM_1… TE_7,TM_8 appearance pattern with thickness of different substrate [64].

17

A third substrate parameter of concern is dielectric loss. A large dielectric loss tangent (tan δ) means high dielectric loss and thus reduces the radiation efficiency of the microstrip antenna. RT/duroid 5880 manufactured by Rogers Corporation [65-66], was selected as the substrate for the spiral antennas. It has ε_r of 2.2, tanδ of 0.0009 and thickness options including 0.127 mm, 0.254 mm, 0.508 mm, 1.575 mm and 3.175 mm.

As shown in Figure 2.3, in free space the dual arm equiangular spiral has a consistent input resistance of about 177 Ω over a broad frequency range when its progressive length is above 0.55 of wavelength of lowest frequency. When such a spiral is placed on a substrate, its input impedance Z_0 can be modified to include the effect of the substrate [28]:

$$Z_0 = \frac{\eta_0}{2\sqrt{\varepsilon_{eff}}} \qquad\qquad (2.4)$$

η_0 is the wave impedance in free space and ε_{eff} is the effective relative permittivity which is approximately $(\varepsilon_r+1)/2$ when half of the space is filled with the dielectric material. In most of cases the thickness of dielectric material h is finite. Thus Z_0 is also a function of g/h (g: gap width between the spiral arms). At the feeding point the real part of impedance converges to the value of a self-complementary structure in a half-space of dielectric as g is small. In addition, Z_0 decreases as ε_r increases.

From Section 2.2.1 it is known that the spirals with $\phi_{ed} \geq 665°$ are able to achieve consistent impedance in free space. When the spiral with $\phi_{ed} = 665°$ is placed on RT/Duroid 5880 dielectric board of thickness either 1.575 mm or 3.175 mm, their impedance responses are similar, as shown in Figure 2.8. In the same Figure the response in free space is provided for comparison. The solid lines represent the input resistance of spiral and the dashed lines indicate reactance response. The plot demonstrates that the input resistance of the spiral converges to about 130 Ω which is much lower than 177 Ω in free space but the reactance of the three cases are similar.
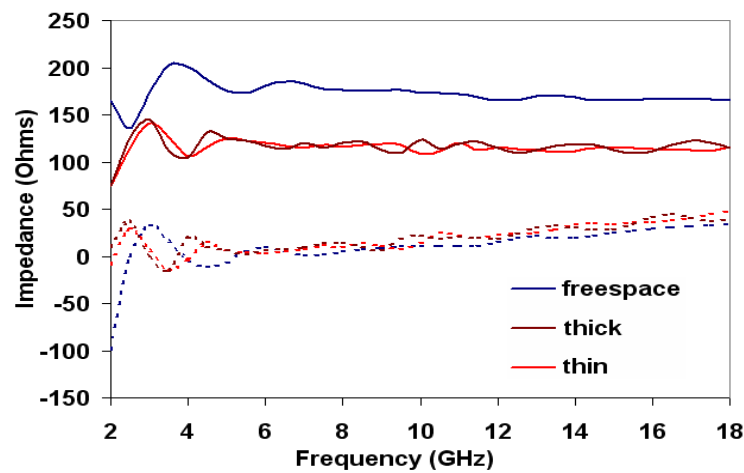
Figure 2.8   The input impedance of a spiral with $\phi_{ed} = 665°$ (solid lines represent resistance, dashed lines represent reactance) in free space; on a thick substrate; on a thin substrate

The expression (2.4) can be extended to the case of grounded substrate. In this case ε_{eff} is no longer a constant. Instead, it is a function of the width of the transmission line; for the equiangular spiral, since its arm expands, its width is a function of the expansion angle ϕ. The characteristics impedance of the spiral on such a substrate can be expressed as:

$$Z(\phi) = \frac{\eta_0}{2\sqrt{\varepsilon_{eff}(\phi)}} \tag{2.5}$$

So at the feeding point the input impedance Z_{in} results from cascade of this impedance series:

$$Z_{in} = \sum_{\phi=0}^{\phi_{ed}} \frac{\eta_0}{2\sqrt{\varepsilon_{eff}(\phi)}} = \frac{\eta_0}{2\sqrt{\varepsilon_{oa}}} \tag{2.6}$$

ε_{oa} – the overall effective permittivity of the dielectric substrate – is equal to the square of the ratio of characteristic impedance of the spiral in free space and on substrate. Take the spiral with $\phi_{ed} = 665°$ as an example: its ε_{oa} is 2.045, which is closer to 2.2 (ε_r) than to 1.6 (ε_{eff}) for half space dielectric material [40].

Besides input impedance, the addition of the dielectric material also changes the radiation patterns of the spiral. The radiation patterns of the spiral with $\phi_{ed}=665°$ at 2, 6, 10, 14, 18 GHz in both planes (azimuth angle $\phi=0°$ and $\phi=90°$) were simulated and analysed using Ansoft HFSS for the three cases, in free space, on a thin substrate and on a thick substrate.

(a) 2GHz

(b) 6GHz

(c) 10GHz

(d) 14GHz

(e) 18GHz

$\phi =0°$ $\phi =90°$
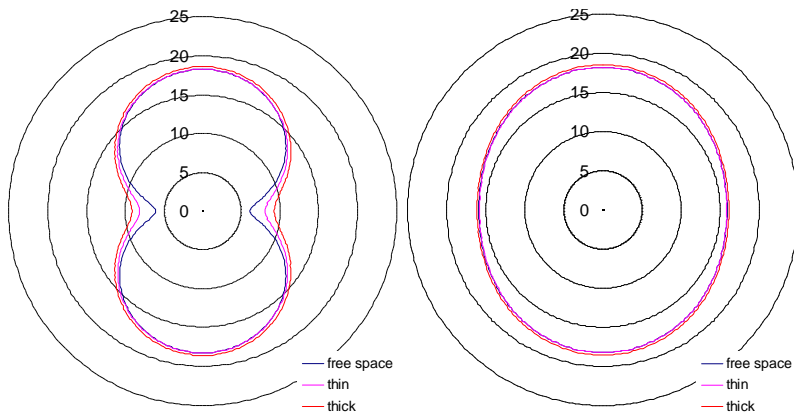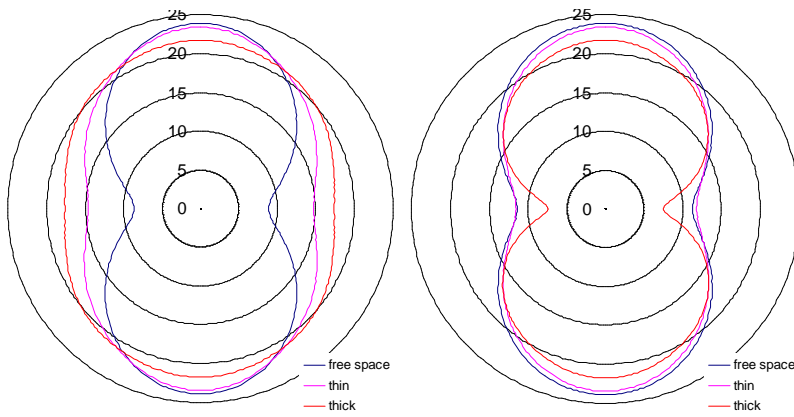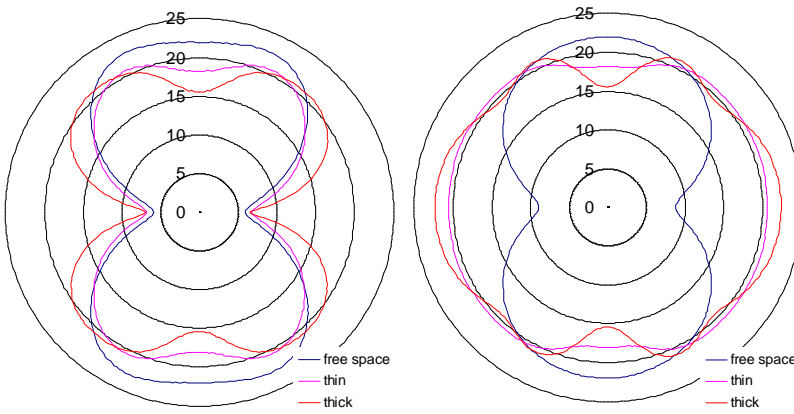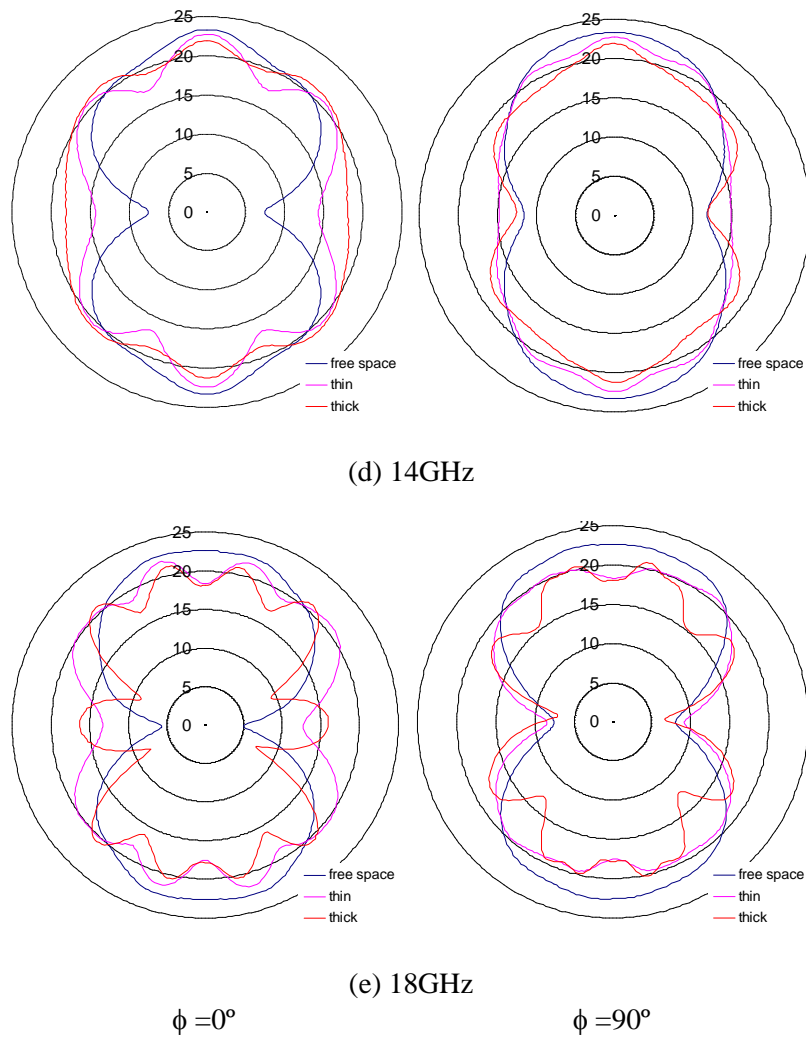
Figure 2.9   The simulated radiation patterns (a) 2GHz (b) 6 GHz (c) 10 GHz (d) 14 GHz (e) 18GHz

As shown in Figure 2.9(a), at 2 GHz, no obvious different was found. Figure 2.9 (b) depicts that at 6 GHz the main lobe becomes wider and a portion of energy deflects into the broadside angular ranges (θ ~ ±45 – ±90 °) and contributes to side lobes especially the ones along the end-fire directions. Figure 2.9 (c) is for 10 GHz. A dip of about 5 dB appeared in the main lobe in both ϕ cut planes and when frequency went higher, more and more ripples appeared θ is within (45 ° ~ 135 °). The deflection of energy to the side lobes is caused by surface waves excited on substrate as they carry away a portion of energy and propagate along other directions and finally experience diffraction or scattering so that they change distribution of energy along azimuth angle in fixed ϕ planes. In this situation, the radius of the substrate is a critical parameter that determines radiation beam shape as well as its power level because the phase of the diffracted surface wave contributes to the phase of total far zone electric field. At the bore-sight direction, the phase factors of these two radiation contributions are e^{-jkr} and $e^{-jk\sqrt{r^2+r_d^2}}$ respectively (k=2π/λ, where r_d is the radius of the dielectric circular plate or the distance between the centre and the edge of the dielectric substrate, r denotes the distance between the centre of the spiral and the far zone checking point). When dielectric material is finite-sized, dimension of the substrate r_d is frequency

21

dependent. Therefore the frequency-dependent phases make the two contributions add up vectorially: at some angles they constructively add but at other angles they deconstructively interfere each other. This explains how energy is deflected to side lobes and forms ripples in radiation patterns.

The effect of a ground plane on spirals has been studied intensively [30] [48-49] through analysis of the current distribution on spiral arms. Usually a ground plane is placed a quarter-wavelength of a specified frequency away, and the spiral antennas are concluded to exhibit standing wave characteristics. In the investigation conducted for this thesis, the ground plane was placed 5 mm away from the spirals (a quarter of wavelength at 15 GHz). Thus this distance for any frequency between 2 and 15 GHz is between $1/30\lambda_0$ and $1/4 \lambda_0$ and for all the other frequencies up to 18 GHz it is between $1/4 \lambda_0$ and $1/3 \lambda_0$. Thus four cases, $1/10 \lambda_0$, $1/8\lambda_0$, $1/4 \lambda_0$ and $1/3\lambda_0$, have been investigated.
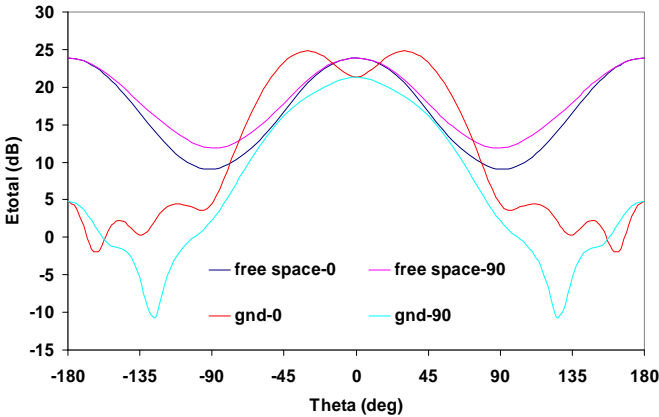
(a)
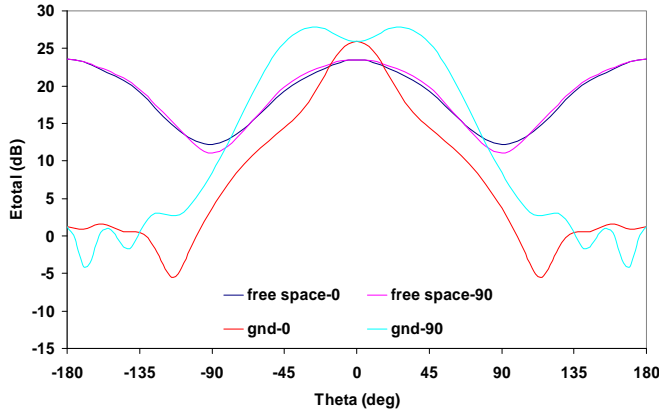
(b)
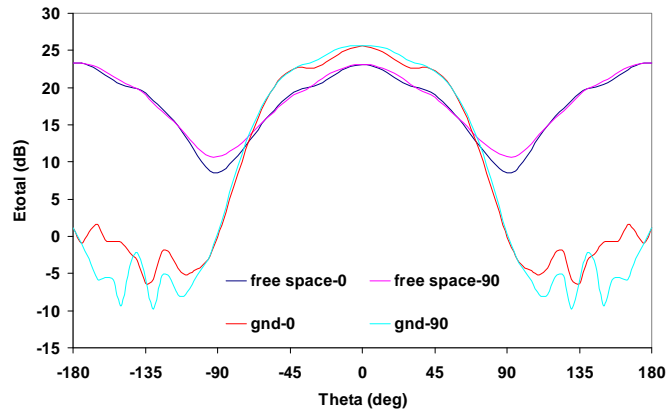
(c)
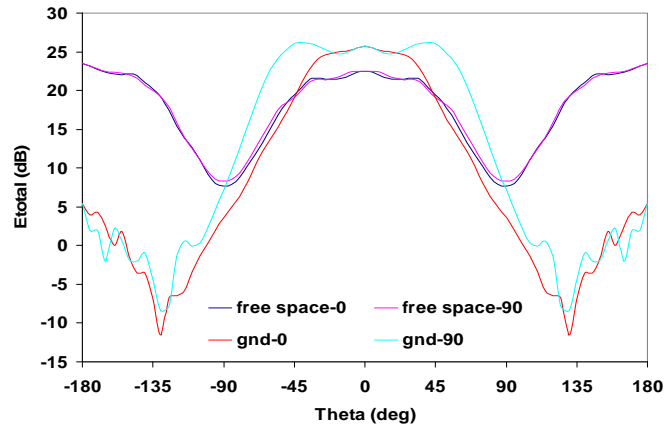
(d)

Figure 2.10   The far zone E_{total} of the spiral above the ground plane (a) $1/10\lambda_0$ (b) $1/8\lambda_0$ (c) $1/4\lambda_0$ (d) $1/3\lambda_0$

Figure 2.10 presents the total far zone radiated electric field E_{total} of the spiral with $\phi_{ed}=665°$ versus elevation angle θ ($-180°$ ~$180°$, denoted by 'Theta' in all the four charts) in two orthogonal cut planes (azimuth angle $\phi=0°$, $90°$) when the ground plane is underneath with four different distances. The variation patterns of E_{total} versus θ of the identical spiral in free space are placed in each chart for comparison. Figure 2.10 (c) and (d) show that the ground plane increases E_{total} ($\phi=0$) and E_{total} ($\phi=90°$) compared to that in free space on the certain ranges of elevation angle θ. A ground plane being $1/4 \lambda_0$ away from an antenna has been often studied and it is believed that the antenna's image in ground plane will have identical current distribution to the real one so that the radiated power doubles the contribution from the real antenna alone [40]. Figure 2.10 (c) displays E_{total} ($\phi=0$) and E_{total} ($\phi=90°$) vs θ ($-60°$ ~ $60°$) having similar the pattern as that in free space but 3 dB above. For the case of the ground plane being $1/3 \lambda_0$ away, the main lobe of E_{total} ($\phi=90°$) is wider but E_{total} ($\phi=0$) is sharper compared to the patterns in free space.

For the other two cases with distance less than $1/4 \lambda_0$ the patterns are more complex. When the ground plane is $1/10\lambda_0$ away both E_{total} ($\phi=0$, $\theta=0$) and E_{total} ($\phi=90°$, $\theta=0$) are lower than that in free space,

23

as seen in Figure 2.10 (a), but for the other θ they are not always lower. Although the patterns at the distance of $1/8\lambda_0$ in Figure 2.10 (b) demonstrate E_{total} ($\phi=0$, $\theta=0$) and E_{total} ($\phi=90°$, $\theta=0$) still higher that in free space, the main lobe of E_{total} ($\phi=90°$) is much sharper and shorter. Bower et al [67] pointed out that when the depth of a cavity goes below $1/8\lambda_0$ the antenna gain of the spiral will drop significantly. Although there is only a ground plane involved in this situation, $1/8\lambda_0$ is still a critical boundary.

It was also observed that ground plane disturbs the axial ratio of spiral antennas. L/λ_0 should be at least 3.8 to ensure the axial ratio of the spiral above the ground plane is below 3 dB on the entire intended frequency range. Figure 2.6 (a) and (b) show that L/λ_0 should be above 1.3 to achieve low axial ratio (<3 dB) in free space. The minimum length of a low-axial-ratio dual arm spiral is required 3 times longer than that in free space.
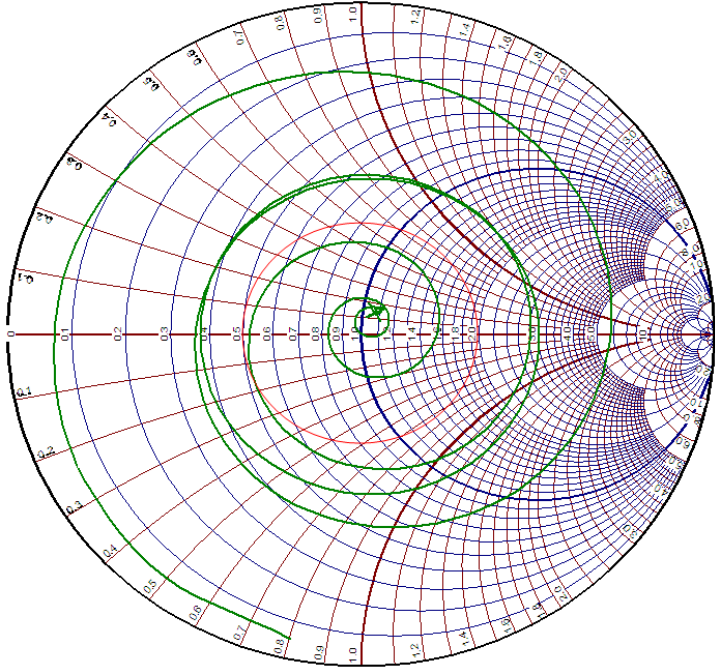
Figure 2.11   Smith chart of a microstrip spiral with $\phi_{ed}=665°$

Figure 2.11 shows on the range of 2 – 18 GHz the simulated input impedance of the spiral with $\phi_{ed}=665°$ on a grounded substrate ($\varepsilon_r=2.2$, 3.175mm thick). Within 2 – 10 GHz, the impedance locus of the spiral are out of the VSWR=2 circle, in other words, VSWR of the spiral is above 2 for each frequency. The curved line out of the circle suggests the response of a open-ended transmission line. In fact, the dual arm equiangular spiral etched on the grounded substrate with thickness much less than the wavelength of any frequency within 2 – 10 GHz (the thickness is about $1/50\ \lambda_{2GHz}$ or $1/10\ \lambda_{10GHz}$) is a curved open-ended microstrip line with variable width. This shows that when the substrate is less than 1/10 of the wavelength the spiral is acting as a microstrip line rather than radiating like an antenna.

2.2.3 Conclusion

Through structural investigations of dual arm spirals it can be concluded that in free space the length of a dual arm spiral antenna should be at least half of the wavelength at the lowest frequency of the intended range to achieve consistent impedance response, and the minimum length should be 1.3 times of wavelength to obtain low axial ratio. In free space, the far zone radiated power of a dual arm spiral at bore-sight direction showed periodic variation versus its ratio of length to wavelength. In addition, if the spiral is long enough the current in the second or third and even higher order active zone may contribute to the far zone radiated field and then change the shape of the radiated beam as well as the strength of the radiated field.

Compared to radiation behaviour in free space, a spiral on dielectric substrate and/or above a ground plane performs differently. The minimum length for a spiral to achieve converged input resistance and low axial ratio rises to 2 and 3.8 respectively when above ground plane. The ground plane reduces the strength of the total far zone radiated electric field at bore-sight direction when it is less than $1/8\lambda_0$ (λ_0 wavelength at the lowest frequency of the intended range) away from the spiral, but it strengthens the field magnitude by about 3 dB when the separation distance is up to $1/3\ \lambda_0$.

A spiral on grounded substrate shows standing wave characteristics at low frequencies because it is more like a curved open-ended transmission line when the substrate is much thinner than the wavelength (about 1/50 to 1/10). This standing wave characteristic shrinks the radiating bandwidth of a microstrip spiral dramatically. A technique is required to extend impedance bandwidth to the low end of the intended frequency range besides mere emphasis on deciding structural parameters.

2.3 Initial proposed solution to remove standing wave characteristics of spiral backed by a ground plane

As seen in Figure 2.11, the spiral on grounded substrate has high VSWR on the range of 2-10 GHz. If viewed in the time domain, a short pulse fed to this type of spiral produces high distortion and the current on the antenna decays at a lower rate than that in free space. The most effective way to reduce the reflection is to attenuate the outward travelling current towards the end of the structure. The Archimedean dual arm spiral loaded with 200-ohm resistive load for each arm [68] was one of the applications employing resistive loading approach.

In order to remove the standing wave characteristics over 2-10 GHz, a novel spiral configuration with a split in the arm is proposed. The split will be filled with a thin film resistive layer (TFRL). It is proposed that this type of planar resistive profile attenuates the residual current on the designed spiral arms. In order not to disturb the frequency-independent features of the proposed spiral, the two curves forming the split should also be based on the equiangular equations (2.1). Figure 2.12 is the photo of the fabricated spiral with such a split and Table 2.2 lists the parameters and their values.

Figure 2.12   The fabricated single arm spiral with split

Table 2.2 The parameters and values of the spiral in Figure 2.12

Curve#	a	ρ_0 (mm)	Φ_{st} (°)	Φ_{ed}(°)
1	0.35	0.508	180	540
2	0.334	0.5	360	570
3	0.308	0.518	360	610

The simulated results in Ansoft Ensemble * show that the resistive film in the split changed the surface current (Jsurf[A/m]) distribution along the spiral arm at 2 GHz, as seen in Figure 2.13. In Ensemble the spiral is modelled as a 2-D copper object and the resistive film area is modelled as a 2-D object with assigned sheet resistance (300- 400 $\Omega/\square$). To simplify the simulation and fabrication of this type of antenna, the resistive film has uniform thickness distribution in the split.
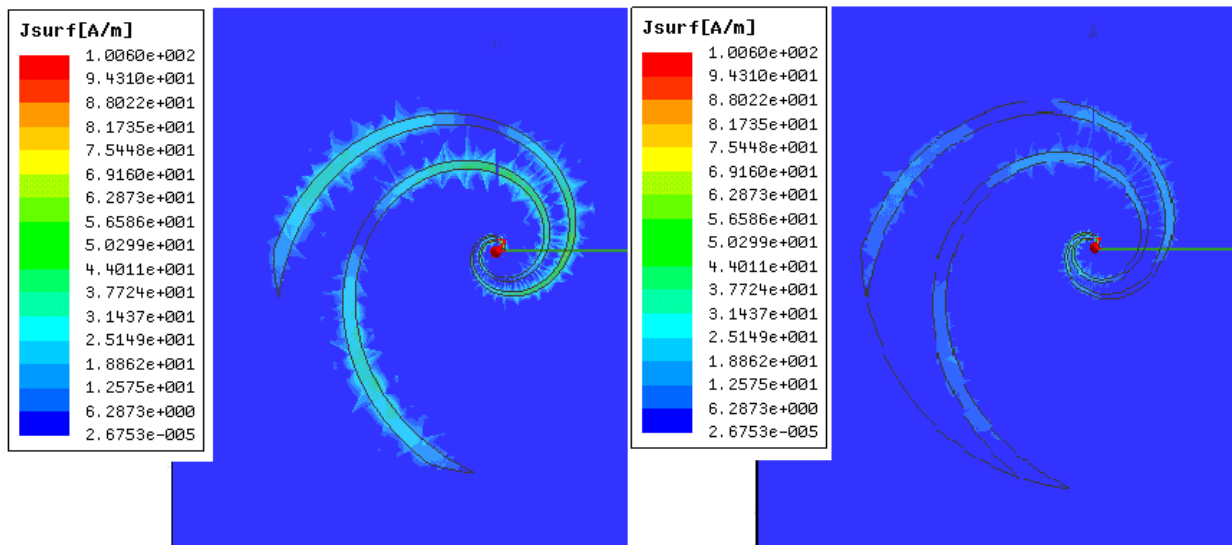
Figure 2.13   Comparison of current distribution of grounded spirals (a) without TFRL (b) with TFRL

2.3.1 Resistive material

Two types of resistive materials are commonly used to produce a thin film resistor: Nickel Chromium (NiCr) and Tantalum Nitride. NiCr alloy is used widely as resistance or heating material owing to its good oxidisation resistance and corrosion properties.

In NiCr alloy, the composition of Nickel and Chromium determines the bulk resistivity of the alloy. The conductivity of Chromium is 3.846×10^7 S/m and the conductivity of Nickel is 1.449×10^7 S/m. Thus Chromium is more "metallic" than Nickel so if the alloy contains more Nickel then it has higher resistivity. When Nickel accounts for 60% – 80% of the volume the resistivity of the NiCr alloy is within range of 200~400 µΩ·cm [69]. However another source quotes the bulk resistivity of the NiCr 80/20 film as 108 µΩ·cm and of NiCr 60/40 60 µΩ·cm [70]. Hence, it was necessary to make some samples of TFRL to find out the sheet resistance for different NiCr alloys.

In a regular three-dimensional conductor, the resistance R can be expressed as:

$$R = \rho \frac{L}{A} = \rho \frac{L}{Wt} \tag{2.7}$$

where ρ is the bulk resistivity, A is the cross-sectional area and L is the length. A also can be described by width W and thickness t while the conductor is a regular cross-sectional shape such as a rectangle.

Thus, resistance R can be rewritten as:

$$R = R_s \frac{L}{W} \tag{2.8}$$

R_s is then defined as the sheet resistance. Because it is multiplied by a dimensionless quantity, the unit is Ω. But usually Ω/□ is used because it gives the resistance in Ω of current passing from one side of a square region to the opposite side, regardless of the size of the square.

2.3.2 Thin film resistive layer samples

As introduced in 2.3.1, the split of the spiral is filed with thin film resistive layer (TFRL) and the required sheet resistance of the TFRL is within the range of 300 – 400 Ω/□. From the information above, the bulk resistivity of NiCr 80/20 alloy should be between 108 and 400 µΩ·cm, thus to make a TFRL with sheet resistance within 300 – 400 Ω/□ the thickness t should be between t_1 and t_2:

$$t_1 = \frac{bulk\ resistivity}{sheet\ resis\tan ce} = \frac{108 \mu\Omega \cdot cm}{400 \Omega / cm^2} = 2.7 nm \tag{2.9}$$

$$t_2 = \frac{bulk\ resistivity}{sheet\ resis\tan ce} = \frac{400 \mu\Omega \cdot cm}{300 \Omega / cm^2} = 13.3 nm \tag{2.10}$$

---

[*] Ansoft Ensemble is based on MOM and it solves 2-D or 2.5-D models by treating ground plane or substrate as an infinitely large object and then approximates by Green's function.

The thickness of NiCr alloy for thin film resistor manufacture usually varies between 100 and 10,000 nm. In order to complete the mixed configuration of spiral antenna, it was necessary to investigate the TFRL of NiCr alloy, e.g. how sheet resistance Rs changes with composition while thickness t is fixed; how sheet resistance Rs changes with t while the composition is fixed; and the behaviour of TFRL on different bases and the adhesion capability on different bases.

Two sets of TFRL samples were fabricated and their sheet resistance was measured. The first set consisting of 3 samples was all ceramic-based but the sputtered NiCr film had different volume composition (80/20, 70/30, 60/40 respectively). The second set (6 samples) had the same composition (80/20) but on different material base or of different thickness. Table 2.3 lists the details of these samples.

Table 2.3 TFRL samples

Sample No	average Rs (Ω/□)	Thickness t (nm)	Base material
1	951	7	Ceramic
2	566	10	
3	151	20	
4	952	10	RT/Duroid 5880
5	738	15	
6	131	20	

It can be seen from Table 2.3 when TFRL of the same thickness is deposited on a different base material, its sheet resistance is different. TFRL was deposited by sputtering Nickel and Chromium individually onto the target material in the vacuum cave. Usually the film should be at least 100 nm so that the particles of Nickel and Chromium are mixed well and uniformly distributed on the surface. The initial simulation in Ensemble suggested to achieve satisfactory absorption effect the TFRL with thickness of 20 nm is desirable. Therefore to deposit 20 nm NiCr with uniform thickness distribution is hardly possible with current sputtering facility.

(a)   (b)
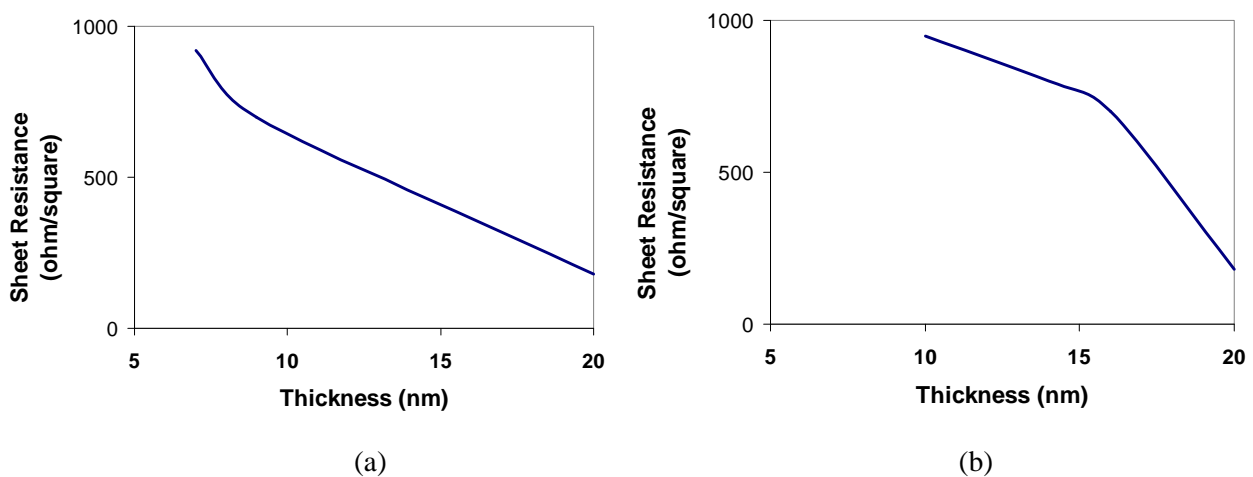
Figure 2.14   Sheet resistance vs thickness of TFRL (a) ceramic (b) RT/Duroid5880

28

2.3.3 Fabricated spirals with TFRL and measurement

Figure 2.15   Three fabricated spirals with TFRL (a) Model X with 20nm TFRL (b) Model Y with 18nm TFRL (c) Model Z with 15nm TFRL

Three spiral models, shown in Figure 2.15 (a)-(c), covered by TFRL with different thickness but the same composition (Ni80Cr20) were fabricated and measured. The thickness of TFRL deposited on these models was 20 nm, 18 nm and 15 nm respectively and the corresponding sheet resistance was about 200 $\Omega/\square$, 400 $\Omega/\square$ and 500 $\Omega/\square$. The models (a) and (b) were both fed by an impedance transformer, e.g. a tapered microstrip line etched onto a 100 mm long and 30 mm wide RT/Duroid 5880 slab. The transformer changed the characteristics impedance from 50 Ω to 100 Ω (matching the input impedance of the spiral antenna). The taper line was mounted to the back of the spiral antenna and the microstrip was connected with the inner end of the spiral via a conducting probe through the hole inside the substrate. The fabrication of this mixed structure was more complex than those made of copper cladding and substrate. The fabrication procedures of these antennas are listed in Appendix B.
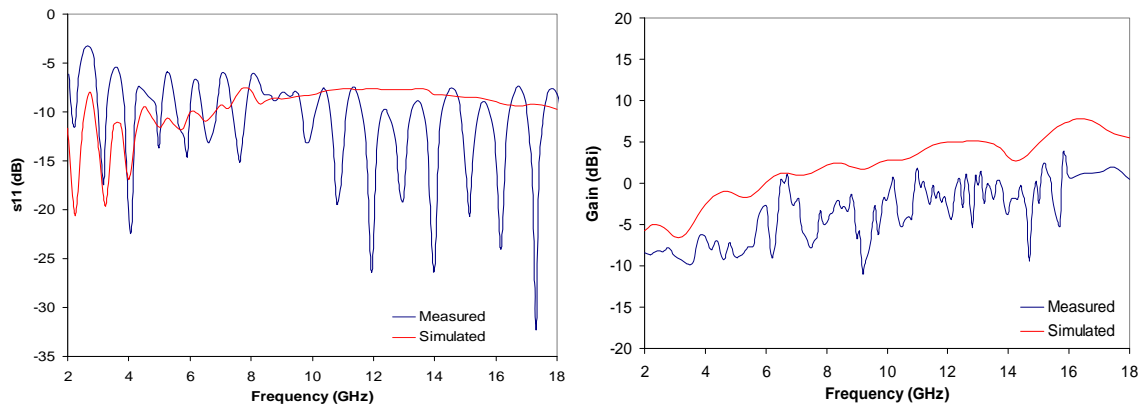
(a)
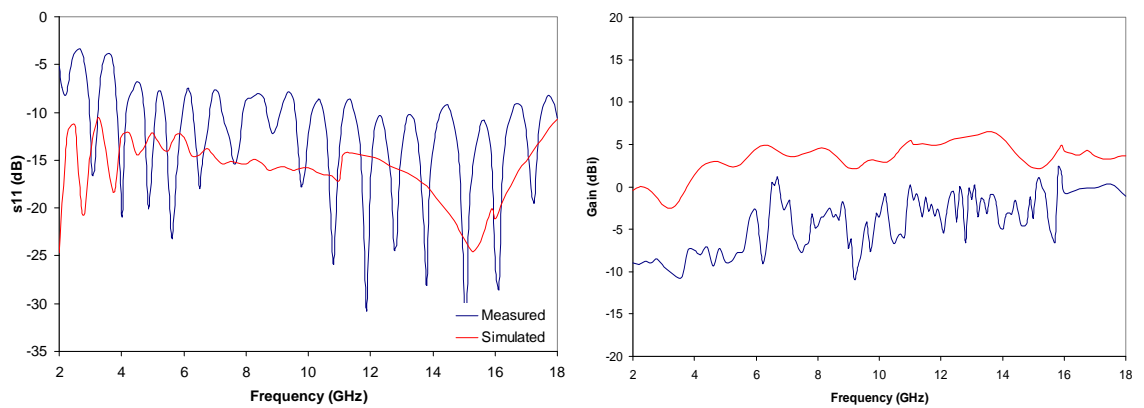
(b)
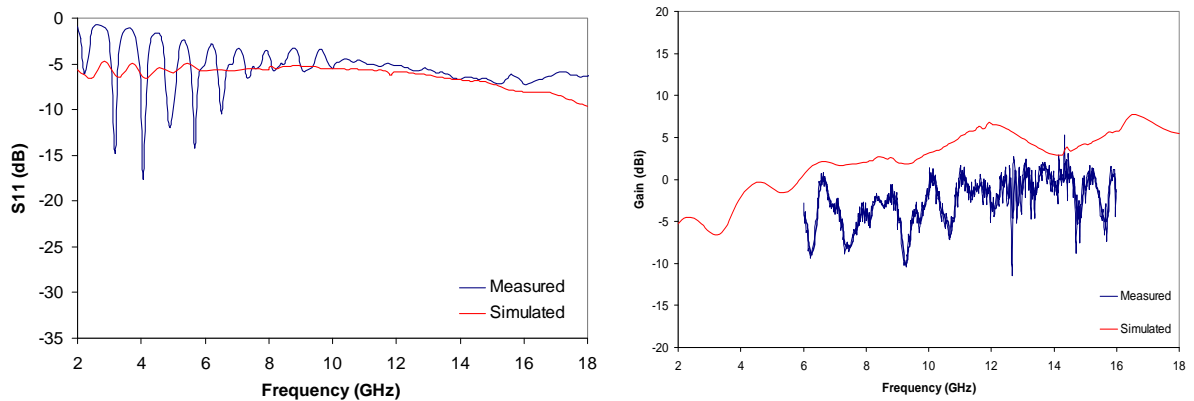
(c)

Figure 2.16   Simulated and measured results of the fabricated models (a) Model X, (b) Model Y, (c) Model Z

Figure 2.16 shows that the measured result of Model X or Y or Z did not match the simulated result for majority of the frequency range 2- 18 GHz; especially at low frequencies. In order to find out the reasons of the mismatch, first of all, the taper impedance transformer used to feed the models with 120 Ω was checked and its simulated S_{11} and S_{12} well agreed the measured results. Thus the simulation approach and the fabrication techniques applied to the antennas Model X/Model Y/Model Z were analysed.

1. in simulation

The initial simulation of the spiral with a TFRL-covered split was conducted using Ansoft Ensemble where TFRL was modelled as a two-dimensional object with impedance boundary described by sheet resistance (Ω/square). In order to verify the simulation, the same spiral models (Model X/Y/Z) were built in Ansoft HFSS where TFRL was modelled as a three-dimensional material box. With the simulating tool HFSS one more issue came forward. The fabricated spirals were etched from the 17 μm-thick copper layer laminated on the surface of RT/Duroid 5880 substrate. And the TFRL in the split, 20 nm thick, is about 1/1000 of the thickness of the copper layer. The contrast of thickness of these two layers made the simulation extremely time and resource consuming thus compromise had to be done and the accuracy of result was sacrificed. None of these two simulation tools could precisely predict S_{11} or antenna gain of these models.

2. in fabrication

As mentioned above, the spiral on RT/Duroid 5880 was etched from 17μm-thick copper layer and the TFRL in the split was only 20nm. To make them contact properly was the key technique in the fabrication. Appendix B list two sets of fabrication procedures that both aim at making the TFRL and metallic part of the spiral contact each other firmly and seamlessly. Furthermore the adherence of TFRL to RT/Duroid 5880 board was also an issue. Unfortunately, there have been no solutions to these two problems.

Besides, the measured value of sheet resistance of TFRL (the four-probe measurement approach referred to Appendix A) showed non-uniform resistance distribution on TFRL of the fabricated models. In the vicinity of the origin of the split, the sheet resistance was around 150 Ω/□. In halfway along the arm, the value was about 300 Ω/□. At the open end of the split, it was around 700 Ω/□. As mentioned above, it is hardly possible to deposit NiCr onto any base with uniform thickness distribution due to requirement of 20nm thick TFRL for the spirals.

In order to understand whether there is a contacting problem between the metallic part of the spiral and TFRL, a rectangular section (seen in Figure 2.17) was cut from Model Y (as shown in Figure 2.15 (b)) and scanned by scanning electron microscope (SEM), which images the sample surface by scanning it with a high-energy beam of electrons in a raster scan pattern The following three pictures show the scanned images with different resolution. Figure 2.18 (a) and (b) are the zoom-in pictures of Part I and part II indicated in Figure 2.17 with finer resolution (500 μm). In Figure 2.18 (a) the light colored parts with "bubbles" indicate laminated copper layer and the dark area is filled by TFRL. Figure 2.18 (b) shows similar "bubbles" which suggests rough verge of the copper cladding may cause contact problems between the copper and TFRL.

Figure 2.17   The cut part of Model Y in Figure 2.14

(a)   (b)
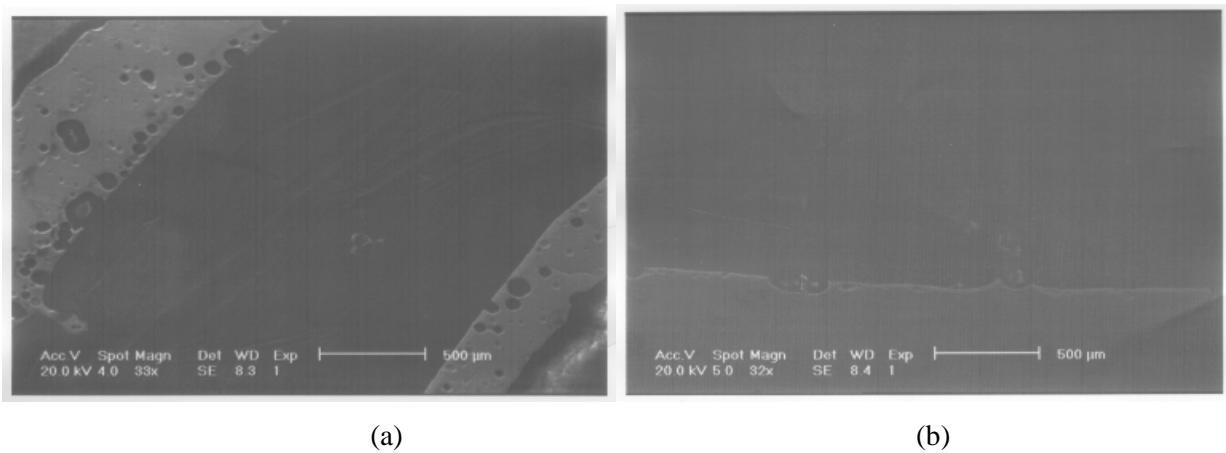
Figure 2.18   Detailed images at 500 µm resolution (a) Part I (b) Part II

2.3.4 Conclusion

As analysed above, it can be concluded that neither the simulation tool nor the fabrication technique of TFRL applied to the spiral antennas were sufficient enough to produce any realistic antenna. The modelling in both Ansoft Ensemble and Ansoft HFSS demonstrated that simulating such a hybrid configuration was extremely time and resource-intensive and it was nearly possible to validate the accuracy. From the fabrication aspect, TFRL is so thin that it is extremely difficult to obtain a resistive layer with uniform thickness distribution in the sputtering process on desired surface. In addition, whether there was contact problem between copper layer and TFRL had not been confirmed. Thick film resistive material may be an alternative which may make simulation easier. However, its paste may not stand the high temperature (about 800ºC) required for the layer solidification process [71]. Thus this type of resistive material can not be employed for real antennas.

2.4 Summary

In this chapter the RF antenna (2 – 18 GHz) was proposed to be designed as a microstrip equiangular spiral. The relevant structural parameters were explored through simulating a series of spirals in different

scenarios - free space, on substrate with or without ground plane. It was concluded that grounded dielectric substrate changes the radiation characteristics of the spirals, and this led to the necessity of introducing an impedance profile to the spiral configuration.

Three experimental spirals with TFRL were developed to explore application of TFRL to impedance bandwidth of a microstrip spiral antenna. Unfortunately, the investigation into TFRL applied to the spirals experiences difficulties in both simulation and fabrication processes. Thus TFRL applied to the spiral antennas had been ceased. Other techniques are still needed to remove the standing wave characteristic to extend the impedance bandwidth of microstrip spirals.

Chapter 3 Microstrip spiral antenna with embedded chip resistors

3.1 Introduction

Chapter 2 documented an investigation of the structural parameters of an equiangular spiral antenna on grounded substrate as well as an exploration of adopting TFRL technique to reduce standing wave characteristic with a microstrip spiral. The TFRL-covered split in the spiral arm was designed to attenuate residual current along the spiral arm and improve the return loss of the spiral over a low frequency range (2 — 10 GHz), but the design was finally abandoned due to the difficulties in both fabrication and simulation procedures.

As shown in the literature review in Chapter 1, chip resistors are employed to solve the problems with microstrip antennas because their lumped resistances can change current distribution in antenna systems. Chip resistors have also been used to make the Archimedean spiral antenna achieved 9:1 bandwidth [39] , therefore employment of chip resistors may be an alternative to TFRL. If chip resistors are a useful alternative to TFRL, it is essential to understand chip resistor application techniques including selection, simulation and fabrication. First of all, chip resistor distribution profile over spiral arms should be based on specified rules rather than random arrangement. A second issue is precise modelling of chip resistors working with the spiral arms. Lastly, the practical effect of chip resistors on fabricated spiral antenna should be repeatable and stable and attributable to fixed fabrication procedures.

In this chapter, section 3.2 describes an analysis of two microstrip equiangular spiral models (Model A and Model B) in the time domain to reveal the radiation characteristics of the microstrip spiral under pulse and harmonic excitation. Subsequently, rules guiding where chip resistors should be loaded are derived. In section 3.3, a chip resistor model simulated using HFSS was validated by simulating and fabricating a spiral antenna loaded with one pair of chip resistors. Sections 3.4 and 3.5 describe the configuration and performance of fabricated dual arm spiral antennas, loaded with embedded chip resistors. Section 3.4 is concerned with the spiral antenna fed by a vertically mounted broadband balun whereas, the spiral antenna demonstrated in section 3.5 utilises a compact balun.

3.2 Investigation of spiral antennas in time domain

Numerical analysis of antennas may be performed in either the frequency domain or the time domain. The popular methods of analysis — FDTD (Finite Difference Time-Domain) and FVTD (Finite Volume Time-Domain) — are good at solving complex electromagnetic problems in the time domain: they are capable of showing snapshots of field distribution within a limited space, which provides a lot of detail about how the EM field radiates or propagates.

Through parametric analysis in chapter 2, it was determined how radiation characteristics related to the structural parameters of the antenna and with what level of sensitivity. A microstrip spiral is different from a spiral in free space or backed by a cavity [33], because it shows standing wave characteristics due to the presence of the grounded dielectric substrate. Nevertheless, analysis of current density distribution on any spiral antenna should reveal the radiation physics of the spirals. Compared to Archimedean spiral

on which the current density distribution depends on radial distance ρ only, the current density distribution on equiangular spiral arms is a more complex function of two variables (radial distance ρ and angle θ).

The analysis in the time domain explained below aims to investigate the radiation mechanism of microstrip equiangular spiral antennas as well as derive particular rules of applying chip resistors on spiral arms to achieve the desired specifications. The specific tasks involved are to:

- find out how the current on spiral decays within a particular duration and how the duration is affected by spiral configuration, dielectric substrate and ground plane
- identify the active zones of the microstrip equiangular spiral to maximise its far field radiated power
- investigate standing wave patterns and how they are related to length of spiral and thickness of substrate when ground plane is present
- determine loading rules for chip resistors arrangement to improve impedance bandwidth and the far field radiation performance of the spiral antenna.

3.2.1 Using XFDTD to model a spiral antenna

Since being introduced by Yee [72] in 1966 the FDTD (finite difference time domain) method has been employed to analyse a variety of antennas. Nowadays mathematical modelling using the FDTD method can be performed using a commercial software package, such as XFDTD, to accelerate and improve the accuracy of antenna analysis and design.

Here, two spirals — Model A and Model B — with different lengths described by the same equiangular equations given below (3.1) were designed to implement the investigation in XFDTD v 6.3.

$$\rho_1 = \rho_0 e^{a\phi}$$
$$\rho_2 = \rho_0 e^{a\left(\phi - \frac{\pi}{2}\right)} \tag{3.1}$$

where ρ_1, ρ_2 in (3.1) are the radial distances between the centres of the spirals and the points with angle ϕ, a is the expansion rate (a positive constant) and ρ_0 is the radial distance of the starting point of the spiral arm.

$$L_i = \int_{\phi_0}^{\phi_{ed}} \rho_0 e^{a\phi} d\phi = \frac{\rho_0}{a}\left(e^{a\phi_{ed}} - e^{a\phi_0}\right)$$
$$L_x = L_i + \rho_0 e^{a\phi_{ed}} \cdot \frac{\pi}{2} \tag{3.2}$$

L_i and L_x are the distances along the inner edge and external edges between the starting point and the ending point of the equiangular spiral.

The ϕ_{ed} of Model A is 4π and that of Model B is $3.7\,\pi$. The other structural parameters are the same: a=0.35, ϕ_0=0.3π, ρ_0=0.508 mm. The assignment of these values was based on the outcome in section 2.2 in chapter 2. After the ϕ_{ed} of Model A and Model B is substituted into expression (3.2) their L_i and L_x can be obtained. For Model A, L_i= 118 mm and L_x=178 mm: for Model B, L_i=84 mm and L_x=128 mm.

Usually two types of excitation may be imposed on the feeding point of an antenna in the time domain — pulse and harmonic excitation. Pulse excitation is used to reveal the broadband characteristics

of an antenna. Harmonic excitation can be used to reveal the current distribution pattern at any particular frequency after the current distribution obtains steady status. The following analyses (3.2.2 and 3.2.3) are based on both of these two types of excitation.

In order to implement the investigation plans outlined in 3.2.1, Model A and Model B were placed on 3.175 mm thick dielectric substrate (RT/Duroid 5880, 130 mm×130 mm) backed by ground plane or nothing. The case of being in free space is used for comparison.

In XFDTD, both of the dual arm spiral's arms are connecting with two conducting probes penetrating through substrate and the pulse or harmonic voltage is applied between the probes at the other end. The input resistance given in XFDTD is 170 Ω (in free space) or 140 Ω (with substrate).

3.2.2 Pulse excitation

A modulated Gaussian pulse is used to analyse the broad characteristics of an object and in its expression f_m is relevant to the intended band:

$$V = e^{-\left(\frac{4}{\beta\Delta t}\right)^2 (t-\beta\Delta t)^2} \cos(2\pi f_m t) \qquad (3.3)$$

where β is pulse width and Δt stands for time step. And

$$f_m = \frac{f_{\max} - f_{\min}}{2}$$

$f_{\max}, f_{\min}$ are the high and low end of the frequency range. And

$$\beta = \frac{4}{\sqrt{\alpha}\Delta t}$$

$$\alpha = \frac{20 f_m^2 \pi^2}{x \ln 10} \qquad (3.4)$$

In fact Δt depends on the cell size after a model is meshed into 3-D rectangular cells. To ensure stability, the Courant condition should be followed:

$$v\Delta t \leq \frac{1}{\sqrt{\frac{1}{(\Delta x)^2} + \frac{1}{(\Delta y)^2} + \frac{1}{(\Delta z)^2}}} \qquad (3.5)$$

In this investigation the frequency range of interests is 2 — 18 GHz, cell size is 0.4 mm (the minimum dimension of Model A and Model B), and Δt in XFDTD is 0.385 ps.

3.2.2.1 Current density (J) distribution of a spiral antenna

It is necessary to introduce the quantified parameters to depict the response of the spiral antenna to the pulse and then to evaluate its radiation performance. In XFDTD, simulation results include return loss, far zone electric field and most importantly, 2-D snapshot images that record current density J distribution over the spiral arms with resolution of 0.4 mm that may clearly and completely portray the entire current decaying process. These pictures with huge amount of information had to be processed and then critical information outlining spiral radiation behaviour – shown as follows — can be extracted from the raw data.

Soon after the pulse excitation the induced surface current started to appear from the inner ends of spiral arms and expand along the arms. Current density J distribution over the spiral arms varied with

time until all current was extinct after the antenna finished radiating. In XFDTD the snapshots of current density J distribution over the spiral were captured and saved as data files which were imported to MatLAB for further processing. Figure 3.1 illustrates the contour line picture of current density J distribution on Model A on a grounded substrate at the 83rd time-step about the moment of 0.032 μs. The contour lines represent the locations of equal magnitude of normalised current density J and they embrace seven different colour blocks which indicate discrete levels of current density J strength by colours (the relationship map of seven colours displaying current density J range between ─30 dB to 0 is on the right side). The colour blocks are showing the strength of current density J along the contour lines by colors, for example, red block outlines the area where J is between -5 dB and 0 dB. In addition, along the line between any two neighbouring colour blocks the magnitude of J is represented by colder colour, as seen rainbow scale in the right corner at the bottom in Figure 3.1, the sequence from warm color to cold color is: red, brown, yellow, green, cyan, navy blue and blue. .
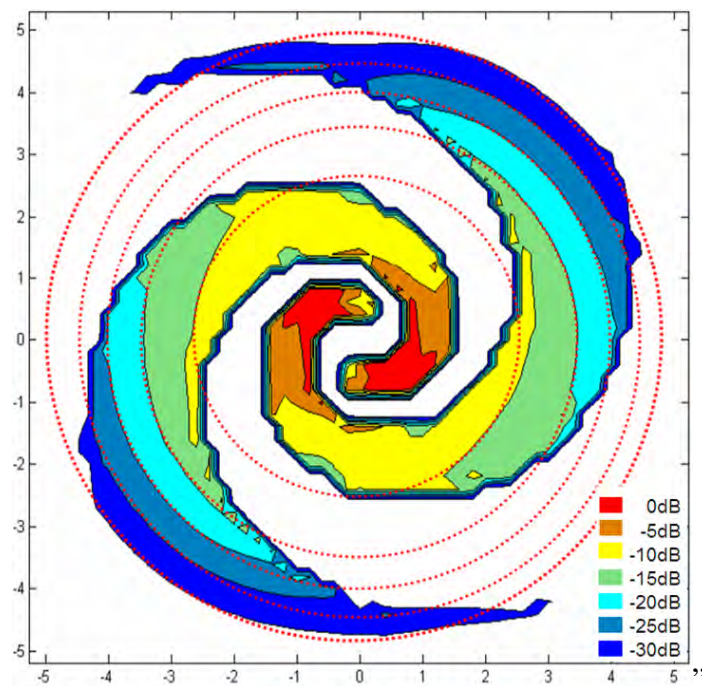
Figure 3.1   Current density contour plot at the moment of 0.032 μs

It is more interesting to recognise that in this picture the five red dashed circles are overlapping with the five contour lines than only to know the current density distribution. The radii of the set of circles in Figure 3.1 are about 2.2 mm, 2.8 mm, 3.3 mm, 3.6 mm and 4.7 mm. The almost perfect overlapping implies that the pulse induces current homogenously and the current diverges evenly outward over the spiral surface as soon as the applied pulse starts to work on the spiral; however, such circular contours only remained for 10 time-steps and then it was disturbed. Also after about 0.5 μs the current gradually concentrates on the internal and external verges of the spiral arms where the current is at least 10dB stronger than all the other areas.

The radius of the biggest circle indicated by the red dotted line in Figure 3.1 was equal to the distance along which the induced current travelled outward from the centre of the spiral. The dielectric substrate made the pulse transmission slower than in free space, as seen in Figure 3.2. At the same moment, in free

space (at 0.035 µs) the outer circle's radius is 6.83 mm and on substrate (at 0.037 µs) 4.97 mm, which is unique for both of the cases when ground plane is present or absent. The ratio of these two radii is about the value of $\dfrac{1}{\sqrt{\varepsilon_{eff}}}$, where ε_{eff} represents the effective permittivity of dielectric material and here it is about 1.81 when the microstrip line width is about 4 mm on 3.175 mm thick RT/Duroid 5880 substrate. It also can be seen that ground plane does not change the size of the area occupied by current.

(a)   (b)   (c)
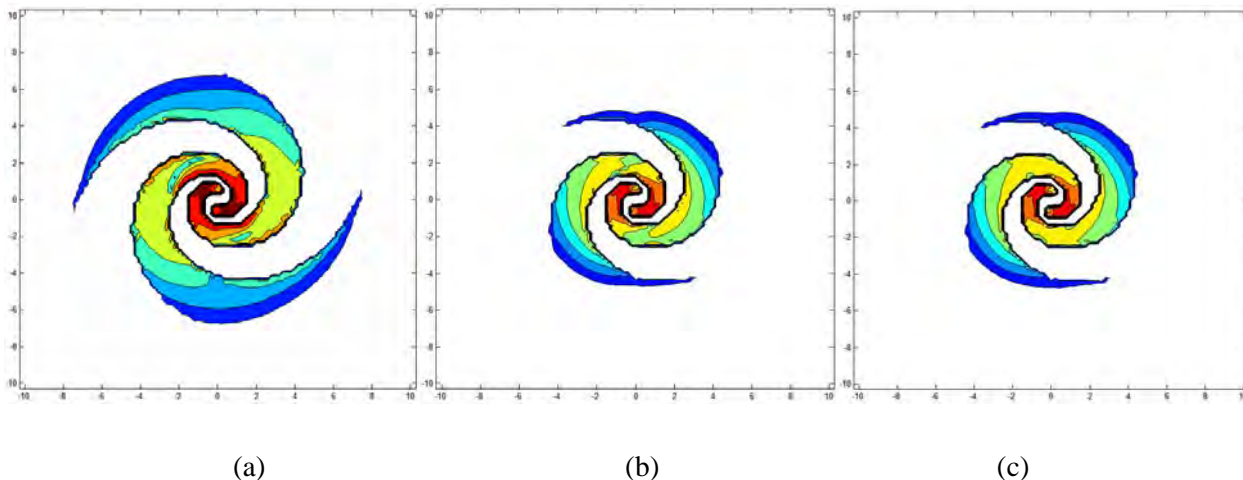
Figure 3.2   Current density J contour plots of Model B (a) in free space (b) on substrate only (c) on grounded substrate

(a)   (b)   (c)
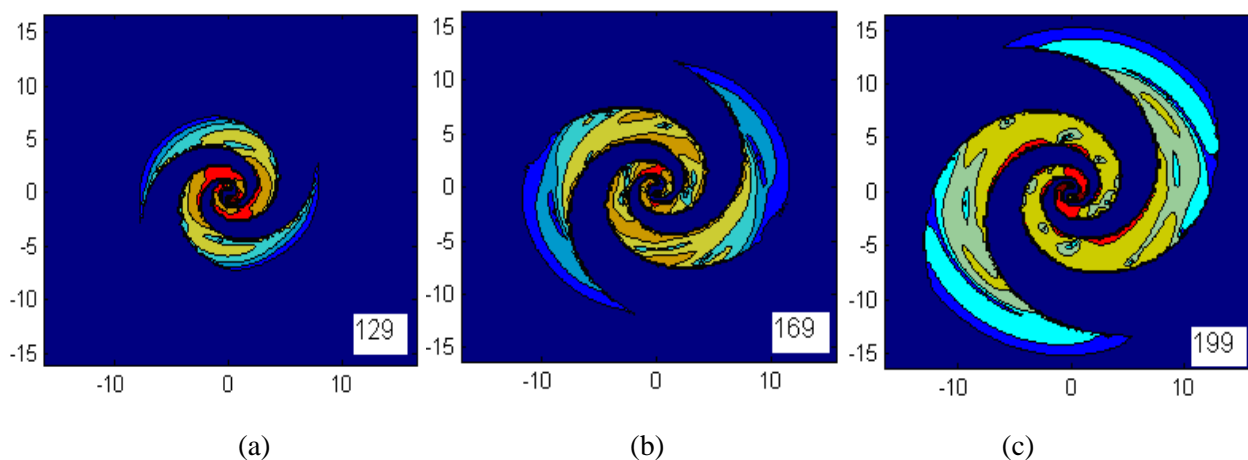
Figure 3.3   Repetitive coupling in free space (a) 0.050 µs (timestep 129) (b) 0.065 µs (timestep 169) (c) 0.077 µs (timestep 199)

It is noticeable that current distribution ─ indicated by the red colour which corresponds to strong current strength ─ disappears and appears within the vicinity of the spiral centre several times for both of the models either in free space or on substrate. Figure 3.3 depicts contour lines of current density J on the spiral arms at the three moments: 0.05 µs, 0.065 µs and 0.077 µs in free space. It can be seen that the strong current in the vicinity of the spiral centre disappeared at the 0.065 µs but came back at the 0.077µs. In general understanding, the spiral is a travelling wave antenna in free space and the current excited by the pulse fed near the centre of the spiral should be travel along the spiral arm until it reaches the end of

the arm. Hence, once the current leaves the centre there should be no more current distributed in the area. First of all, if the repetitive appearance of the current was caused by the dispersion in transmission the separation the arrival time of low frequency and high frequency components should be much shorter than the duration between 0.05 μs and 0.077 μs time-step which is 0.027 μs. Thus dispersion is not the reason. The real reason is that the current may be coupled to the adjacent area located on the other arm. The coupling is particularly strong in the vicinity of the spiral centre as soon as the pulse is fed into the antenna due to two facts. One is that at beginning of current being excited on the spiral arm the transient current is very strong. The other fact is that in the area near the centre of the spiral the two arms are closer than all the other areas. Observations on the area of strong current density in other time frames also confirm the repeatedly occurrence of the coupling of the travelling current between the adjacent arms of the spiral. However the colour-filled contour plots are not detailed enough to reveal the mechanisms; further quantifying expressions are required.

3.2.2.2 Maximum current density J_{max}

J_{max} vs. time

A quantifying parameter J_{max}, which represents the maximum magnitude of current density J over the spiral arm at a specified moment, is analysed to depict current transmission, reflection and dissipation progress [48] from which broadband radiation feature and other characteristics such as dispersion can be recognized.
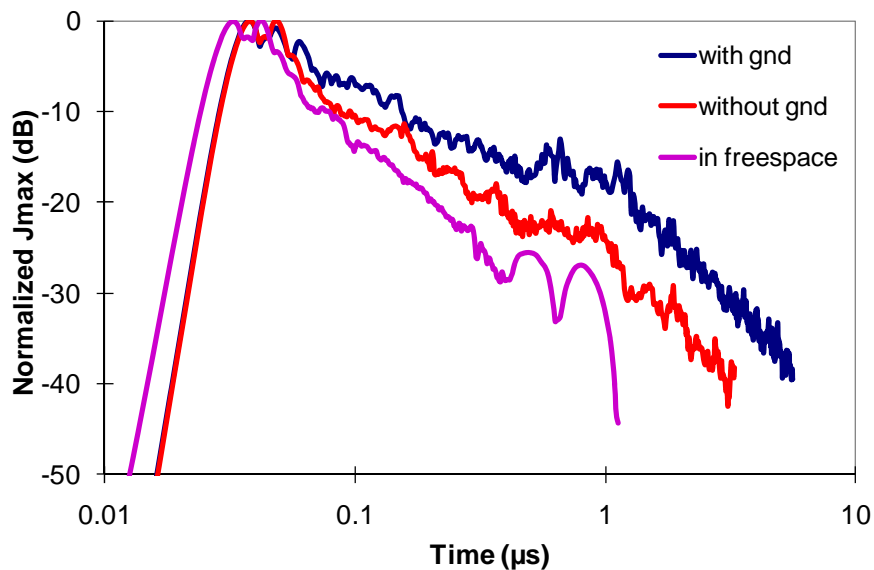
Figure 3.4   Normalized J_{max} on Model B vs. time in free space, on thick substrate with and without ground plane

J_{max} may vary with time and radial distance. Figure 3.4 indicates that normalized J_{max} changes with time on Model B in free space, on substrate only and on grounded substrate. The label "with gnd" indicates the scenario in which the spiral is on the grounded substrate and "without gnd" refers to substrate without ground plane on the back (the substrate are both 3.175 mm thick). For each case J_{max} at each moment is normalised by the maximum J_{max}, for instance, the maximum J_{max} occurred at about 0.032μs) when Model B is in free space.

With the case of free space, indicated by purple line in Figure 3.4, within a very short time (less than 0.1μs) J_{max} climbs up to the peak. In fact, there are two successive peaks of similar heights and the separation of 0.01μs between them is caused by the dispersion in transmission. After the peaks J_{max} linearly drops to about −30 dB then returns in the form of another two successive sub-peaks (−25.5 dB at 0.49 μs and −26.9 dB at 0.80 μs). It is believed that these two sub-peaks are the reflections of those two peaks at the very beginning and the separation of about 0.31 μs is much longer than the previous separation of 0.01 μs due to dispersion added up on the travelling route. After experiencing multiple reflections and the continuous radiation, the current on spiral becomes weaker and weaker until fading out 1.13 μs after the moment of the pulse fed. In Figure 3.4, blue and red lines show that the presence of the dielectric substrate delayed the two peaks, the two sub-peaks and the entire decay progress of J_{max}. It took 3.27 μs for the current on the spiral on the substrate without ground plane to fade out completed. With the case of grounded substrate, the ground plane exacerbates the delay on top of the effect of dielectric substrate without ground plane by 2.31 μs (it took totally 5.58 μs for the current to fade out). Model A has similar patterns in these three scenarios; however, the difference is that longer length of Model A prolongs the decay process of the current. Although dielectric material does delay the transmission of the current on or in it, it is not the only reason making the delay of the entire decay progress of the current on Model A or Model B. The reason is explored and explained by presenting J_{max} versus radial distance.
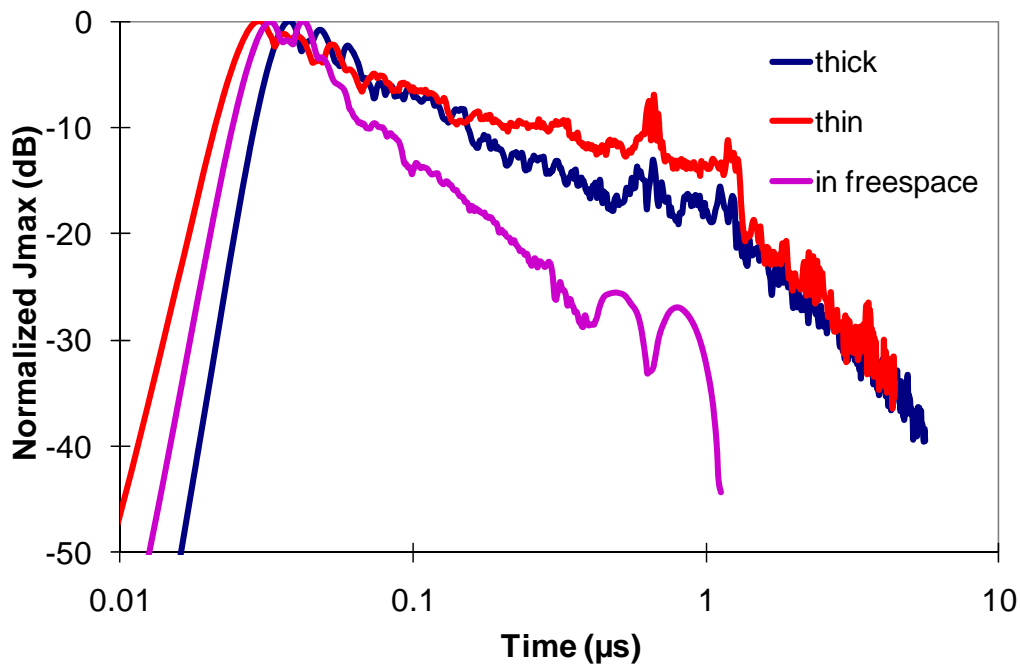
Figure 3.5   The normalised J_{max} on Model B vs. time

Model A and B on grounded substrate were particularly studied since the proposed antenna was a microstrip spiral. Two grounded substrates with different thickness (3.175 mm and 1.575 mm) were considered. How the thickness affected J_{max} decaying is presented in Figure 3.5 with the response in free space as reference. For these two cases, it took similar time period for the current decay to the ignorable value (−40 dB) and their response patterns are also very similar except that within 0.15 μs − 1.65 μs.

Within this range, J_{max} of the spiral on the thin substrate is about $3-6$ dB higher than that on thick substrate at the same moment. It is known that how fast the current on the spiral decreases in time domain determines the bandwidth of the spiral in frequency domain. Thus from the difference over the duration between 0.15 µs and 1.65 µs it can be identified that thick grounded substrate makes the spiral achieve broader bandwidth than the thin substrate. In addition, high J_{max} of the spiral on the thin grounded substrate must be related to a type of coupling between the spiral and the ground plane since the spiral is closer to the ground plane. The coupling is clarified and analysed below.

J_{max} *vs. radial distance*

It can be seen from the plot of J_{max} vs. Time, such as Figure 3.4 and 3.5, only the value of J_{max} at each moment is known, however, where the location of maximum current density J is still unknown. In order to obtain more details of current distribution in the spatial domain, J_{max} vs. distance was introduced. Figure 3.6 demonstrates J_{max} versus radial distance for the three cases of spiral in free space, on substrate and on grounded substrate. The radial distance refers to the distance between the location of maximum J_{max} and the centre of the spiral. In (a), the case of free space, at five moments the location of J_{max} moved abruptly from one location to another. For example, at the moment of 0.064 µs the spot of strongest current density J changes from 7 mm to 5 mm away from the spiral centre. The only explanation for why spot of J_{max} jumps back towards the centre is the cross-talking between spiral arms. Another interesting phenomenon is that in Figure 3.7 - the zoomed chart of the red rectangular area in Figure 3.6 (a) - it can be clearly seen that at three moments 0.304 µs, 0.368 µs and 0.396 µs the bright spot transfers back from end of spiral to a particular location on the spiral arm. The three moments are very close and they occur after the moment (0.3 µs) when travelling current reaches the end of the spiral. In this scenario, the reflected current interacts with the forward current, which is still travelling outward before reaching the end of the spiral due to dispersion, and the superimposition changes bright spots rapidly. From this point then until the moment 0.61 µs, the maximum spot goes back to the centre of the spiral. About 0.037 µs later it does not go beyond 12 mm before it comes back to centre again, then it remains in the circle of 5 mm radius until it decays to 0. It should be noted that there is a fairly smooth variation slope with J_{max} decreasing from -10 dB to -20 dB and radial distance changing from 2.5 mm to 29 mm. Over this period the current travels progressively along the arm with less cross-talking between arms until it extinct.

Compared to the response of spirals in free space to the pulse, Model B on grounded substrate (3.175 mm thick) or substrate only has much more complex responses (as shown in Figure 3.6(b) and (c)), from which it is hardly possible to identify those moments when the back-and-forth changes happened. The only information revealed was that in Figure 3.6(c) the mono-decreasing line across the entire spiral arm was suggesting the bright spot with the highest current density J value proceeds along the spiral arm steadily without evident returns. As contrast, within the same time slot the decreasing trend in Figure 3.6(b) has more back-and-forth lines covering the radial distance between 6 mm and 15mm. This complexity of variation lines should be related to effect of the ground plane. Obviously — with the presence of ground plane — there is much more transference of bright spots from the end of the spiral back to the spiral centre across the entire arm. As analysed above, since the cross-talk happens between neighbouring arms only, the big spatial leap of J_{max} location should not result from that. It was analysed

and concluded that the coupling between the real spiral and its image in the ground plane was the reason. This is also confirmed in the scenario of the spiral on thin grounded substrate.

The repetitive coupling on the spiral arms mentioned above reflected the concept of cross-talk between arms and coupling between real spiral and its image.

(a)

(b)

(c)
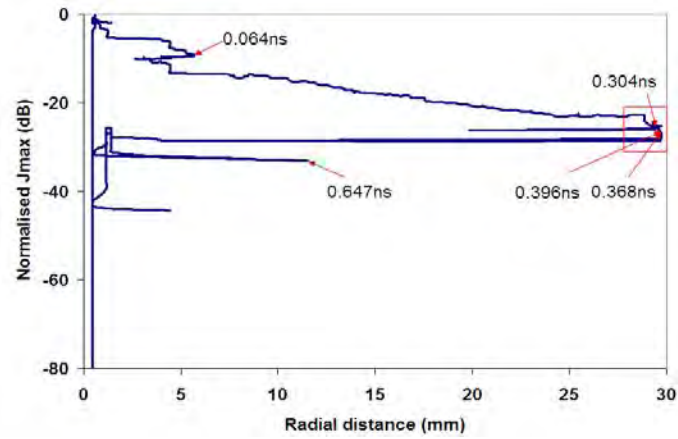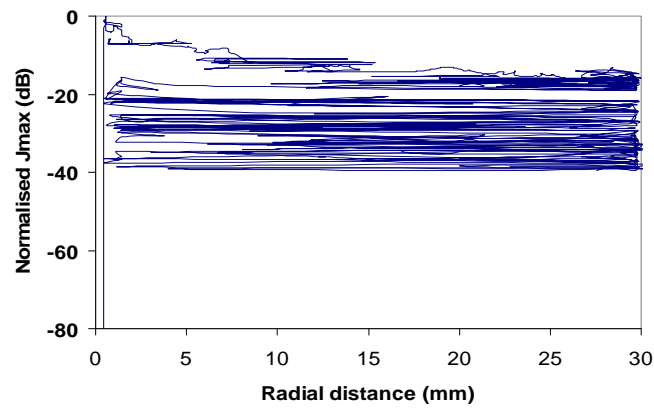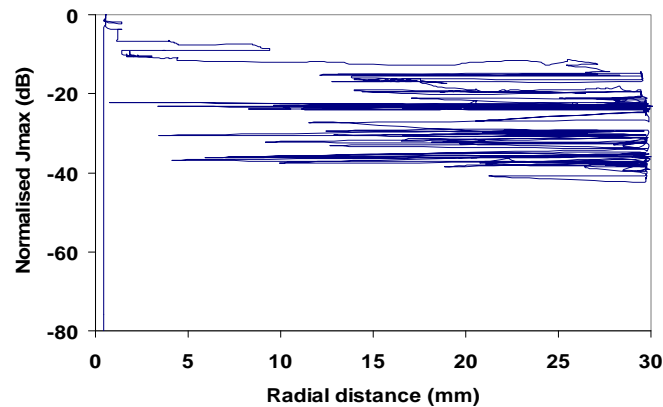
Figure 3.6 J_{max} vs. radial distance of Model B (a) in free space (b) on substrate backed by ground plane (c) on substrate only

Figure 3.7 J_{max} of Model B in free space vs. radial distance with higher resolution

Current density J distribution on spiral arms under pulse excitation was studied in the spatial domain and time domain. Three facts should be noted. Firstly, within a very short time the induced current expands from the centre of the spiral towards every direction with unique velocity thus the contour lines resembled circles. Secondly, after another several hundreds of time-steps (the duration depends on what scenario the spiral is in – in free space or on grounded substrate), the transmitting current starts to concentrate on the verges of the spiral arms and is reflected when it reaches the end of the spiral. Thirdly, analysis of J_{max} vs. radial distance clearly clarifies the phenomenon of cross-talking between arms existing in all the scenarios whether spiral in free space or on substrate or on grounded substrate. When the ground plane is on back of the substrate, coupling between the real spiral and its image in the ground plane affects decay of current on top of the crossing-talk.

3.2.3 Harmonic excitation

When the antenna is fed by a sinusoid wave with particular ω, the input transient voltage is:

$$V = \sin(\omega t) = \sin(2\pi f t) \tag{3.6}$$

Continuous harmonic excitation stimulates the propagation at a fixed frequency f along the spiral arms until steady state is reached. Harmonic excitation is often used to show frequency-dependent features of radiation mechanism; again, current density distribution forms a particular pattern in steady state.

43
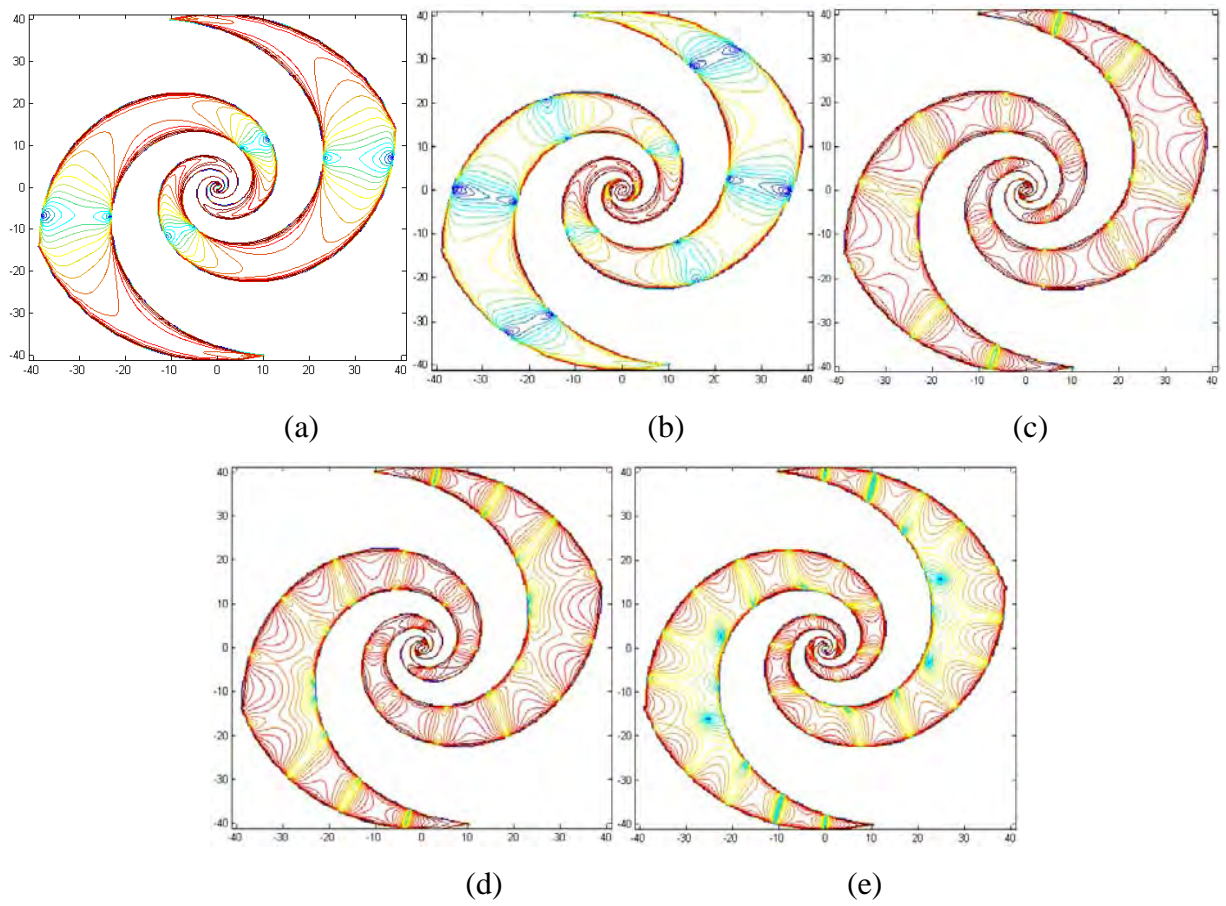
Figure 3.8   Current density J distribution at steady state of Model A (a) 2 GHz (b) 4 GHz (c) 6 GHz
(d) 8 GHz (e) 10 GHz
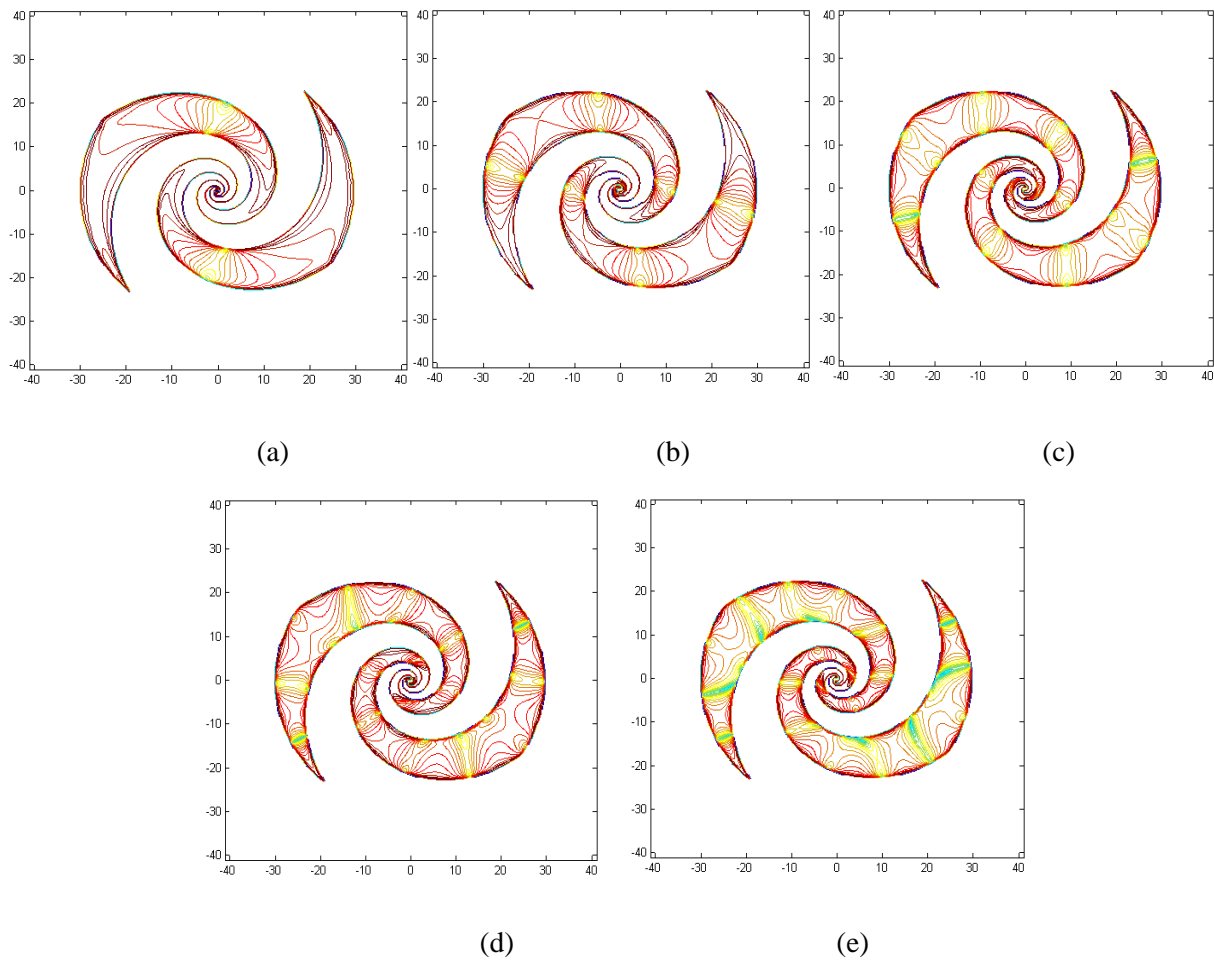
Figure 3.9   Current density J distribution of Model B at steady state (a) 2 GHz (b) 4 GHz (c) 6 GHz (d) 8 GHz (e) 10 GHz

Figure 3.8 and Figure 3.9 contain three contour plots of normalised current density J over the spiral arms of Model A and Model B respectively at 2 GHz, 4 GHz, 6 GHz, 8GHz, 10GHz. X and Y coordinates (unit mm) are shown on the plots of the axes. The figures show that the red lines gathered at the verges or at the points close to verges of spiral arms. The uniform distribution of these gatherings suggests that standing waves were established over the spiral appearing like the "hill" and the "valley". Usually these standing waves appear in pairs along the inner and outer edge of spiral arms and each pair of "hills" is partly merged. When the spiral arm is wide enough compared to the wavelength of a particular frequency, for example 8 GHz, the "hills" are separated clearly.

In the contour plots in Figure 3.8 and Figure 3.9, the blue spots mark the boundaries of adjacent sections of the standing waves. The number of standing wave sections is related to both the frequency of the harmonic wave and the total length of the spiral arm. The lengths of the sections of standing waves on spiral arms at different frequencies were obtained from Figure 3.8 and 3.9 and are listed in the statistics box plot Figure 3.10. It shows the size of the standing wave at different frequencies on Model A and Model B. Each label on the bottom shows that the gray box contains the readings of all Standing Wave length (SWL) on the spiral (Model A or Model B) at the frequency (2 − 10 GHz). For instance, the box above the label "2GHz_A" contains all the SWL readings of Model A at 2 GHz and the solid line in the middle indicates the average value.

45
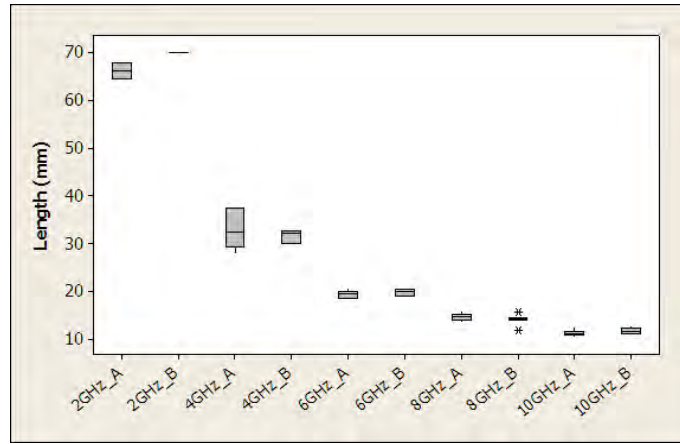
Figure 3.10   Box plot of Standing Wave Length (SWL) on Model A and Model B

It was observed that almost at every frequency the average value of standing wave length (SWL) of Model A was similar to the value of Model B. The table below shows the relationship between SWL on Model A and the wavelength at 2 – 10 GHz in free space.

Table 3.1 Standing wave length of Model A

Freq (GHz)	2	4	6	8	10
SWL (mm)	66	32	20	14	11
λ_g (mm)	101.1	50.6	33.7	25.3	20.2
SWL/λ_g	0.65	0.63	0.59	0.55	0.54

λ_g is expressed as $\lambda_0 / \sqrt{\varepsilon_r}$. It can be seen that all the ratios of SWL to λ_0 are slightly more than 0.5.

Usually on a transmission line, each section of standing wave should be half of the guided wavelength λ_g long at each frequency. From this perspective, a spiral on grounded substrate can be regarded as an open-ended transmission line at those frequencies whose corresponding wavelengths are much larger than the thickness of substrate. Due to this fact of the standing wave overweighing the travelling wave on a microstrip spiral within such a frequency range, the microstrip does not radiate.

3.2.4 Conclusions

Time domain investigation is used to understand the radiation physics of a microstrip spiral antenna, and further analysis derived chip resistor loading guidelines. The outcome of a quantitative analysis of the current density distribution on the equiangular spiral Models A and B helped to determine a chip resistor profile to apply to the spiral arms. Under pulse excitation the current expansion frontline resembled a circle, leading to *Rule 1* which states that chip resistor should be in pairs and in the same arc sharing the centre with the spiral. Over time, induced current gradually approaches the edges of spiral arm, leading to *Rule 2* − that chip resistor should be loaded by the edges of the spiral arm. In addition, reflection at the ends of the arms makes current strength bounce back and slows current decay duration. Thus *Rule 3* requires that a pair of chip resistors must be loaded at the end of each spiral arm. Furthermore, study of

current distribution at steady state confirmed that peaks of standing wave happen at the verges of spiral, and also the "first active zone" of a microstrip spiral is very different to that of a spiral in free space or backed by a cavity. This leads to *Rule 4* ─ chip resistors must be located out of the first active zone, and the size of this zone has to be determined in terms of the total length of the spiral and the frequency range of interest. The fact that standing waves established over spiral arms are dependant on frequency leads to *Rule 5* - chip resistors should be located at places where the standing wave is strong for most of the frequencies within the intended frequency range. The last rule, *Rule 6*, is that as few resistors should be applied to the spiral as possible. This important restriction comes from the consideration of the radiation efficiency of the microstrip antenna. A compromise must be achieved between the number of resistors and antenna efficiency. When chip resistors deteriorate standing waves by dissipating part of the current on the spiral arm, they also dissipate a certain portion of radiating energy, thus lowering the radiation efficiency of the antenna. Hence the goal of employing chip resistors on a spiral is to use the smallest number to minimise negative effects on the radiation efficiency of the spiral.

3.3 Chip resistor loading technique

When a spiral is located on grounded substrate with thickness of 3.175 mm (less than $1/10\lambda_0$ if f_0 is less than 8 GHz) it shows strong standing wave characteristics like those of transmission line does; thus chip resistors are required to operate at up to 8 GHz by changing current distribution on spiral arms. Although 2 – 8 GHz covers the low end of the intended frequency range, it is a super high frequency range for a variety of HF chip resistor products. Over this range, there are two other important considerations about employing resistors besides resistance range and the tolerance and temperature coefficient (TCR) of resistance. One factor is that the reactance of resistors becomes enormously high and the second relates to the modelling of chip resistor in computer simulation.

3.3.1 Chip resistor selection and modelling

3.3.1.1 Chip resistor selection

Theoretically resistors are frequency-independent, but in reality there is an additional contribution to the impedance by an inductance L and a capacitance C. The inductance results from trim cutting ‐ a common manufacturing technique for conventional resistors ‐ while the capacitance is formed by the ceramic dielectric of the resistor body and the metallic contacts [73]. The following figure is used to describe the resistance behaviour. It is known that the helical trim cutting produces high inductance of up to 22 nH [74]. Compared to conventional resistors, an HF resistor has low inductance resulting from smooth groove cutting (instead of the trim cutting techniques such as helical trim, pulsed trim and meander trim) in the resistive layer to achieve a target resistance value. Table 3.2 displays L, C and R of three products by VISHAY Company.
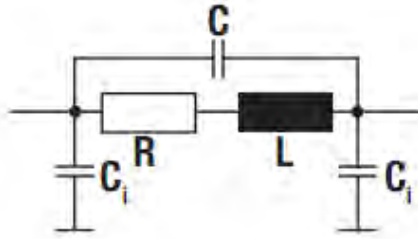
Figure 3.11　　Resistor substitution circuit [73]

Impedance Z of such a resistor with substitution shown in Figure 3.11 is described by the following equation:

$$Z = R \cdot \frac{1 + j\omega \dfrac{L}{R}}{1 - \omega^2 LC + j\omega RC} \tag{3.7}$$

Table 3.2 The impedance of HF chip resistor products [75-76]

Product name	L (nH)	C (fF)	R (Ω)
MMA 0204 HF			100
MCT 0603	0.875	35	100
MCT 0603	0.8	55	150

Thus

$$\frac{|Z|}{R} = \sqrt{\frac{1 + \left(\omega \dfrac{L}{R}\right)^2}{1 + (RC)^2}} \tag{3.8}$$

Based on an RF behaviour plot of Z/R of these products from the manufacturer, MCT 0603 150Ω was selected.

3.3.1.2 Chip resistor modelling

HFSS is a 3D EM simulation program enabling all the elements to be modelled as 3D objects or 2D boundaries (finite conductivity boundaries for metallic objects and impedance boundaries for impedance). Chip resistors are typically manufactured using thin film technology and are mixtures of thin film resistive layers, metal and dielectric material. In theory, all these elements of a chip resistor should be precisely considered when chip resistor is being modelled [77] in simulation software, but chip resistors are usually located at the place where current is weak. Thus it may be described as a 2D rectangular object with a lumped RLC (resistance, inductance and capacitance) boundary provided by HFSS.

3.3.2 Validation models of spiral with chip resistors

In order to validate chip resistor modelling, a single arm spiral with a split and a pair of chip resistors loaded at the ends of the two branches (Figure 3.12) was fabricated and measured. The spiral model was

48

fed by an impedance transformer which is a tapered microstrip line converting the characteristics impedance from 50Ω to 100Ω.

Figure 3.12   The single arm spiral with split loaded by one pair of resistors
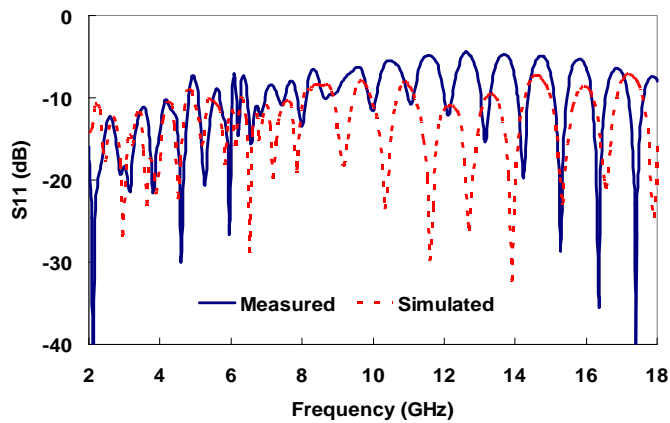
Figure 3.13   The simulated and measured S_{11} of the spiral

Figure 3.13 presents the simulated and measured results of the spiral shown in Figure 3.12. The modelling of the spiral loaded by chip resistors accurately predicted S_{11} of this complex structure within 2 – 6 GHz and there is slight discrepancy between simulated and measured result at the frequencies within 6 – 8 GHz. Unfortunately the modelling did not achieve similar results to measurement over the range of higher frequency. A possible reason is that the real reactive part of the chip resistor is much higher than the value provided by the manufacturer after it is loaded to the spiral on the grounded substrate.
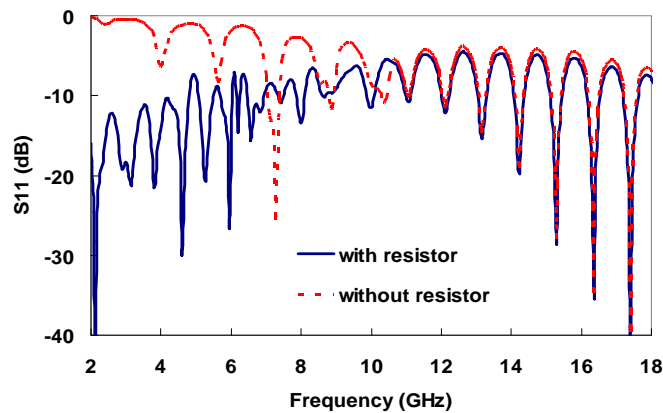
Figure 3.14   Measured S_{11} of the spiral with/without resistors

To verify the hypothesis all the loaded resistors were removed from the fabricated spiral antenna. Figure 3.14 shows that S_{11} measurements of the spiral with and without resistors are very similar over a

49

high frequency range. This pattern displays that the chip resistors are ineffective at higher frequencies (above 10 GHz). In addition, simulated results of the spiral with chip resistor were similar with measured results at lower frequencies. Hence the modelling of the chip resistor may be ignored at frequencies above 10 GHz and modelling of spiral with chip resistors at up to 10 GHz can be conducted and repeated on other similar spiral models with confidence.

3.3.3 Summary

The validation of chip resistor modelling by developing a single arm spiral loaded with one pair of chip resistors confirms that the chip resistor loading technique can effectively improve the impedance bandwidth of the microstrip spiral. Meanwhile the modelling method may be efficient and accurate in predicting the spiral antenna loaded by chip resistors up to 10 GHz and for higher frequencies modelling of chip resistor need not be included in the simulation due to the very high effective reactance of the loaded chip resistor.

3.4 The dual arm spiral antenna with a vertical balun

3.4.1 The configuration of the antenna

This dual arm spiral antenna is prototyped on Model A which was analysed in the time domain (refer to section 3.2). It is etched on a square Rogers RT/Duroid 5880 ($\varepsilon_r = 2.2$) board which is 130 mm by 130 mm and 3.175 mm thick. Twelve 150 Ω MCT 0603 HF chip resistors connect the edge of the arms to the ground plane via pins inside the substrate. The arms have identical chip resistor distribution. The fabricated model is shown in Figure 3.18.

3.4.2 Initial arrangement of chip resistors and optimisation

Initially the arrangement of chip resistors over the spiral arm was based on the loading rules concluded in 3.2. One of the rules refers to deciding locations of chip resistors according to current density contour lines at steady state, as displayed in Figure 3.8 (a) - (e). Ideally all the frequencies up to 10 GHz should be considered thus there should be at least 20 pairs of chip resistors are required if one pair is assigned for each section of the standing wave. However, the sixth rule says the number of resistors should be low enough not to affect radiation efficiency too much. The compromised arrangement of chip resistors should be done between radiation efficiency of the spiral and necessary absorption of residual current along the spiral arm. As seen in Figure 3.15 (a) - (c), only 2, 4 and 6 GHz are considered and the red or yellow or blue colour blocks display the area along whose boundaries the chip resistors should be loaded for 2 GHz or 4 GHz or 6 GHz. In addition, the chip resistors should be within the overlapped area of two or three different coloured blocks to ensure absorb current for two or three frequencies simultaneously. Under these two restrictions, their initial locations are determined and indicated by red dots in Figure 3.16 where the number "45" displays the distance of 45 mm between the spiral centre and the border.
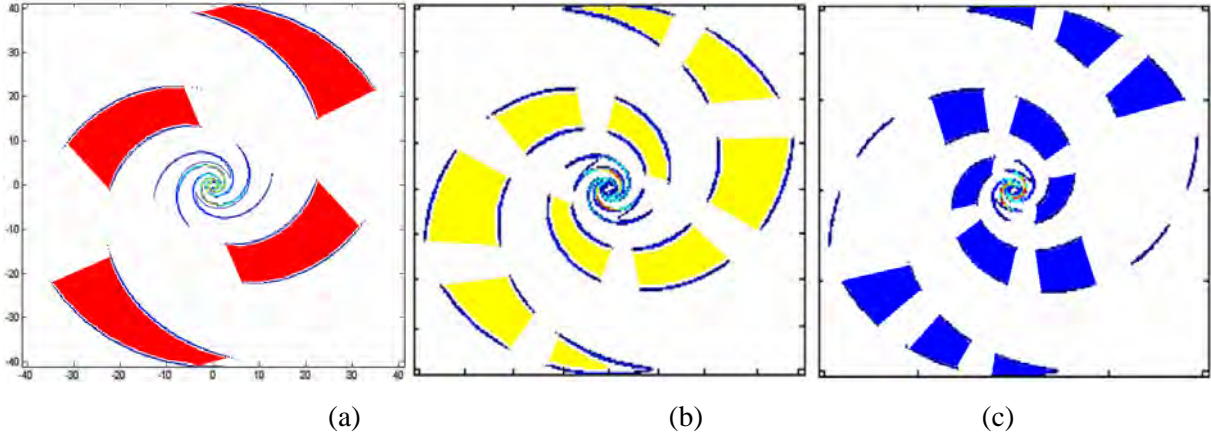
Figure 3.15   The initial chip resistor loading area at (a) 2 GHz (b) 4 GHz (c) 6 GHz
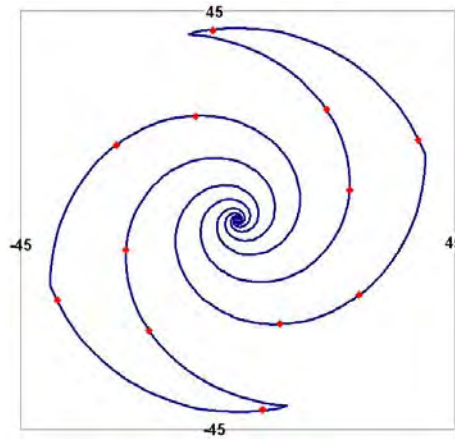
Figure 3.16   The initial chip resistor arrangement on the spiral

The initial model's simulated S_{11} of below -10 dB at most of the frequencies are very impressive, however, its antenna gain and axial ratio are less satisfactory. The axial ratio of a good circularly polarised antenna should be below 3dB over the designed frequency range and azimuth, elevation angular range. In order to achieve better Gain and axial ratio, all the loading locations of chip resistors are optimised with each set of competing options decided within the vicinity of each initial location.

In the optimising process it has been revealed from the comparison of the simulated results that axial ratio was much more sensitive to the chip resistor locations than the antenna gain. Thus to achieve low axial ratio, the optimisation requires tuning of the parameters of the locations of chip resistors.

3.4.3 The vertical taper balun

In Chapter 2 it was mentioned that this antenna was designed as working at mode 1 under which the characteristics Z_0 between two probes for odd mode in free space is 60π Ω and Z_0 becomes lower, about $130 - 140$ Ω, when the spiral is placed on dielectric substrate. Thus a balun was needed to feed the balanced port with Z_0 of 130 Ω. As mentioned in section 2.2 of chapter 2, characteristics impedance in the case of grounded dielectric material substrate is proportional to $1/\sqrt{\varepsilon_r}$ so that it was expected to be around 126.7 Ω. In fact in initial simulation the centre of the input impedance locus of the dual arm spiral converges to 130 Ω.

51

3.4.3.1 Taper balun

Duncan and Minerva introduced a taper balun to work with balanced aerials in 1960 [78]. Later, different taper designs were developed to achieve smooth transition between transmission lines and keep the ultra wide operation band such as the balun [79] with reduced length, microstrip to non-coplanar paired-strips tapered balun [80], microstrip to CPS transition [815] and CPW to CPS balun [82-83]. Taper baluns are inherently broadband devices due primarily to the natural potential difference between signal and ground conductors. There are two basic circuit implementations for the taper balun [84]. The inline-tapered balun requires a gradual taper in both the top and bottom conductor widths. The input end resembles microstrip and the output end is a pair of equally wide strips providing a balanced port. Over such a transition structure, two modes which are odd (differential) mode and even (common) mode propagate independently and the characteristics impedance is different for each mode. This type of transition structure has fewer dimensions than the other circuit implementation [85].
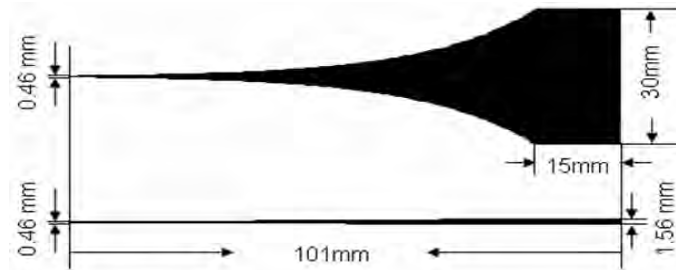
Figure 3.17   The tapered vertical mounted balun

A prototype inline-tapered balun was constructed for the dual arm spiral. It was designed to convert the unbalanced microstrip port to balanced paired strip-lines as well as change the characteristics impedance of 50 Ω to 130 Ω. As seen in Figure 3.17, the balun is made of patterns etched on both sides of a 101 mm by 30 mm RT/Duroid 5880 (high frequency laminated dielectric material) slab which is 0.508 mm thick. The upper pattern consists of the rectangle (30 mm by 14 mm) and a line of width exponentially decreasing from 30 mm to 0.46 mm. The bottom pattern linearly decreases from 1.56 mm to 0.46 mm. The upper pattern functions as the ground plane for the bottom pattern at the one end and then becomes its parallel strip line. These two patterns work together transforming characteristic impedance from 50 ohms at one end to 130 ohms at the other end with odd mode. In the fabricated antenna model, the balun was mounted vertically to the back of the spiral. Its length (101 mm) adds extra dimension to the spiral antenna system, however as a temporary testing balun it was purely used to provide the spiral with the requested balanced power source.

3.4.4 Simulation and measurement

(a)   (b)
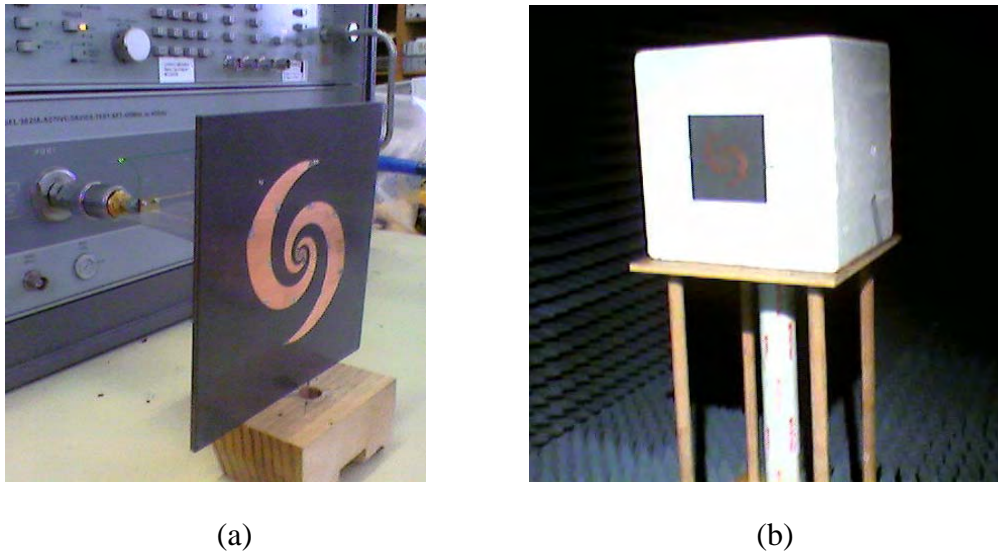
Figure 3.18   Fabricated spiral antenna (a) on scalar network analyzer (b) in anechoic chamber room

The fabricated dual arm spiral antenna model with the vertical testing balun was measured using the scalar network analyser as shown in Figure 3.18 (a). Its gain and radiation patterns are measured in the anechoic chamber room using VNA (vector network analyser), as shown in Figure 3.18 (b). Figures 3.19 - 3.22 show the measured and simulated S_{11}, gain, axial ratio and radiation patterns.
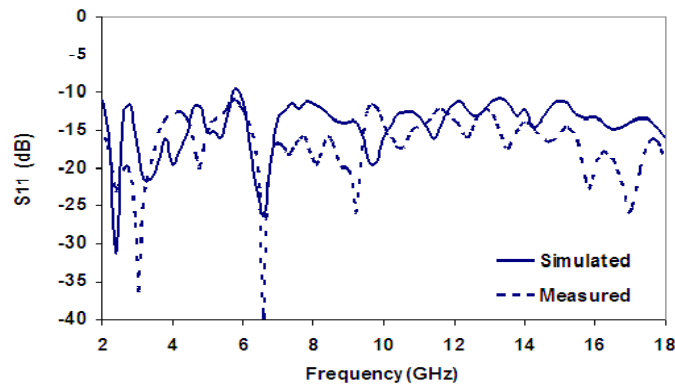
Figure 3.19   Measured and simulated S_{11} of the spiral antenna
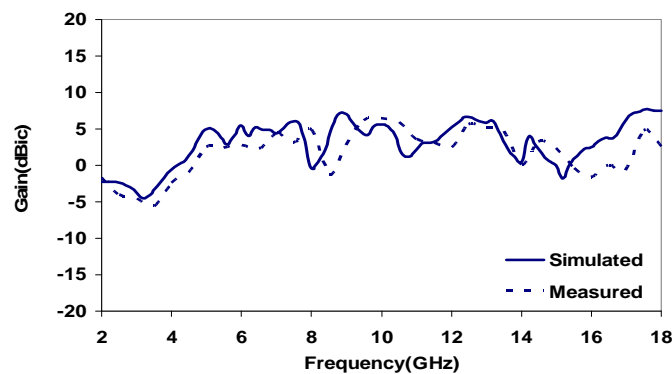
Figure 3.20   Measured and simulated gain of the spiral antenna
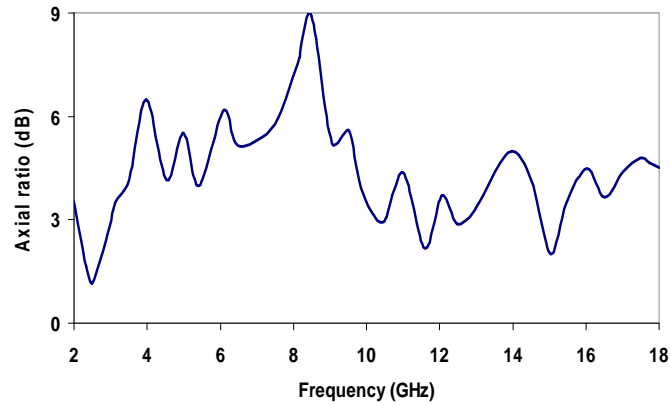
Figure 3.21   Measured axial ratio of the spiral antenna

Figure 3.19 shows that the measured and simulated S_{11} of the spiral antenna are both below −10 dB over the entire frequency range of 2 to 18 GHz and show reasonable agreement, although the difference extends to about 10 dB at some frequency points.

Figure 3.20 portrays the simulated and measured bore-sight gain of the spiral antenna. Once again the measured and simulated gain follow a similar trend, but the measured result was typically lower than simulated result. From 2 to 5 GHz the gain was below 0 dBic, a result of energy dissipation by the chip resistors. From 15 to 17 GHz the measured gain again drops to around 0 dBic due to surface wave generation.

Figure 3.21 displays measured bore-sight axial ratio of the spiral antenna. In order to measure the axial ratio, the spiral antenna was kept in a fixed position and the source antenna (a linear polarized horn) was rotated every 15º over 180º. The difference between the maximum and minimum received signal levels was then recorded. It is seen that the bore-sight axial ratio changes with frequency, ranging from about 1 to 9 dB. The peak at 8.5 GHz corresponds to the null at the gain measurement of Figure 3.20. The cause of this phenomenon needs to be investigated further, however it is postulated that this gain null may be a result of the physical configuration of the transition through the ground plane. Generally the axial ratio of a circularly polarized antenna should be less than 3 dB, thus the axial ratio of this spiral may require further improvement.

(a)

(b)

(c)

(d)

55
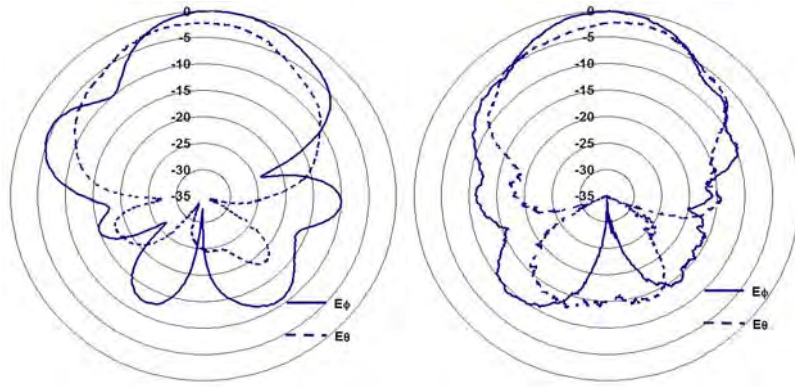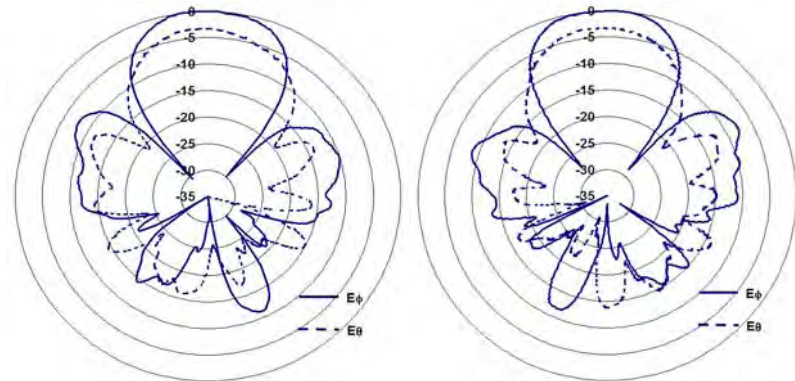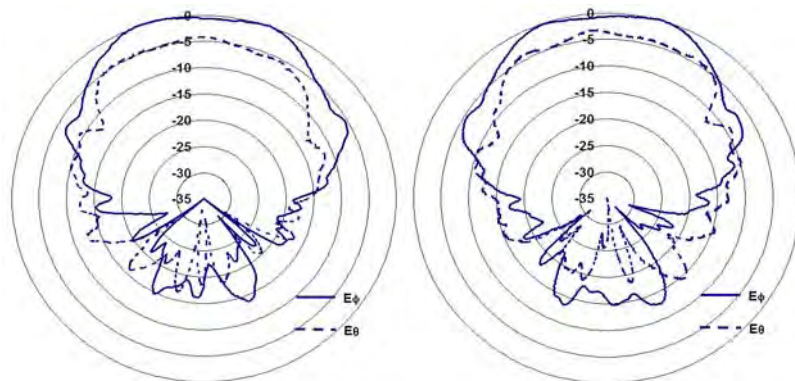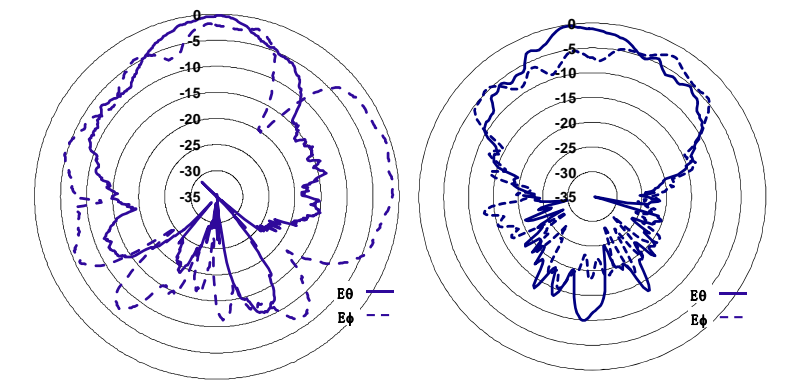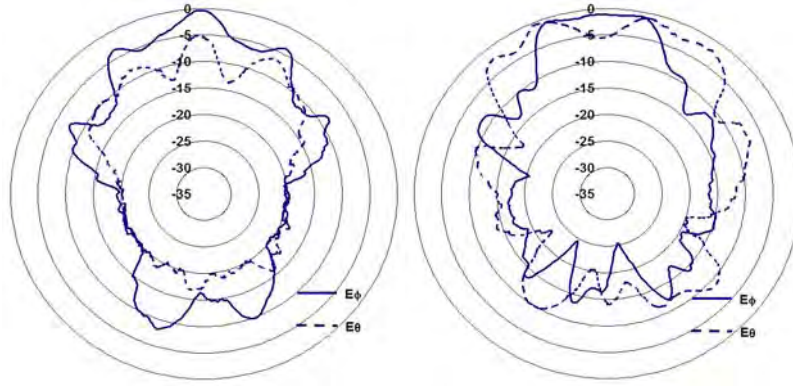
(e)

Figure 3.22   Normalised measured E_ϕ and E_θ of the spiral at both ϕ cut planes (ϕ=0 and 90°) (a) 2 GHz, (b) 6 GHz , (c) 10 GHz, (d) 14 GHz, (e) 18 GHz, left column: ϕ=0 , right column: ϕ=90°

Figure 3.22 shows the normalized measured orthogonal components of far zone radiated electric field E_ϕ and E_θ at different frequencies across the impedance bandwidth of the spiral antenna in both ϕ cut planes (ϕ=0 and 90°). Figure 3.22 (a) to (c) show that the front-to-back ratio is more than 20 dB in both plane cuts, but reduces to around 10 dB at 14 GHz and 18 GHz. In this structure, there is a circular clearance of 1.5 mm radius in the ground plane which allows the feed connection. The first active region of the spiral antenna at these higher frequencies is about the size of the clearance: therefore, part of the radiated field is coupled through the clearance contributing to the backward radiation. There are also strong ripples in radiation patterns, particularly at higher frequencies (Figure 3.22 (d) and (e)), which are caused by the diffracted surface waves. Selecting a thinner substrate for the spiral antenna will reduce the severity of the ripples.

3.4.5 Conclusion

The simulated and measured S_{11}, gain and radiation patterns for a dual arm spiral antenna with a vertical balun were presented in this section. The dual arm spiral antenna achieved 9:1 bandwidth with fairly good axial gain. The design has potential for those applications that require ultra broadband, circular polarisation, and low volume without using any microwave absorbing material.

The next step was to extend the work described to date by developing a compact balun to implement a completely low-profile antenna system.

3.5 The dual arm spiral antenna with a compact balun

3.5.1 The configuration of the antenna

This spiral has the same structural parameters as Model B (section 3.2): the structural parameters in expression (3.1) are a =0.35, δ=0.5π, ϕ_0=0.33π, ϕ_{ed}=3.7π and ρ_0=0.508 mm.
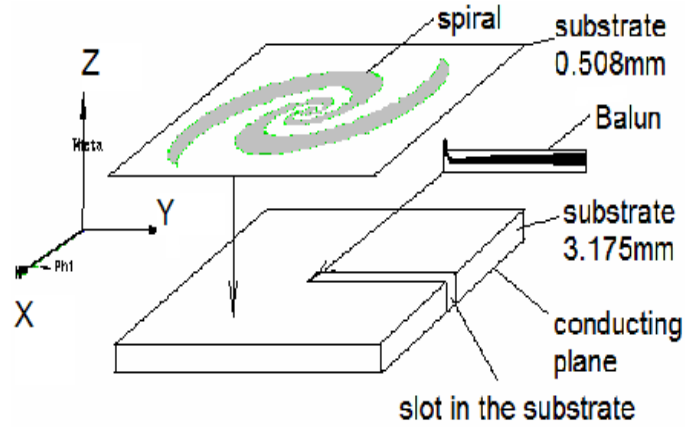
Figure 3.23   The configuration of the spiral antenna with embedded balun and chip resistors

Figure 3.23 shows how the antenna system is organised. The system contains one dual arm equiangular spiral antenna, a compact balun and several chip resistors. It consists of two RT/Duroid 5880 (ε_r=2.2) dielectric plates of different thickness, both 125 mm square. The spiral is etched on the thin layer (0.508 mm thick). The thick layer (3.175 mm thick), which is backed by a conducting plane, has a slot inside where the balun is placed with both of the output pairs connected to the starting ends of the spiral antenna. Compared to the spiral antenna introduced in last section 3.4, this antenna is placed on the slightly thicker substrate. Thus similar to the determination of chip resistor arrangement based on current distribution at low frequencies with the fabricated antenna introduced in section 3.4 (the six rules) the following pictures demonstrate how to determine chip resistor profile for this dual arm spiral.
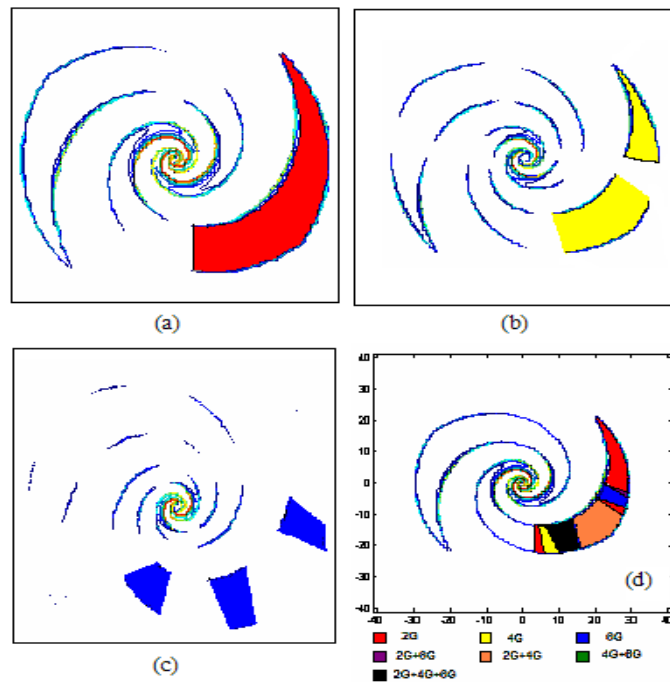
Figure 3.24   The loading 'map' of chip resistors
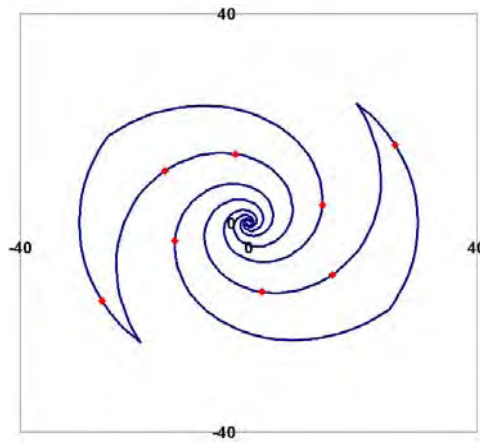
Figure 3.25   The initial chip resistor arrangement on the spiral

Figure 3.24 shows the process of determining the loading locations of the chip resistors which is similar to the process for the fabricated antenna introduced in section 3.4. Although residual current only appears on the edge of the spiral arms, in order to clearly demonstrate the overlapping areas which show the possibilities of appearance of strong residual currents, solid colour blocks are used. This picture is the loading 'map' which displays how the resistors should be placed in each area: the darker in colour the more necessary it is to put resistors in the 'block'. For example, if a resistor is put in the black block, it would effectively dissipate residual current while at 2 GHz, 4 GHz and 6 GHz. However this 'map' can not precisely specify the locations of chip resistors, thus further and finer tuning of the parameters is required to achieve the best layout of chip resistors.

The initial locations of the chip resistors, derived from the 'map' shown in Figure 3.24, are indicated by red dots in Figure 3.25. Optimisation of location in the vicinity of the initial arrangement of chip resistors above was also similar to that in section 3.4 but different because the number of chip resistors had been optimised. In this case, eight resistors made the spiral achieve good performance and also improved radiation efficiency of spiral antenna.

3.5.2 Compact balun

This balun consists of two lines etched on both sides of a slab of dielectric material 62.2 mm long, 2.39 mm wide, 0.508 mm thick and made of Rogers RO4003 (ε_r=3.38), as displayed in Figure 3.26.
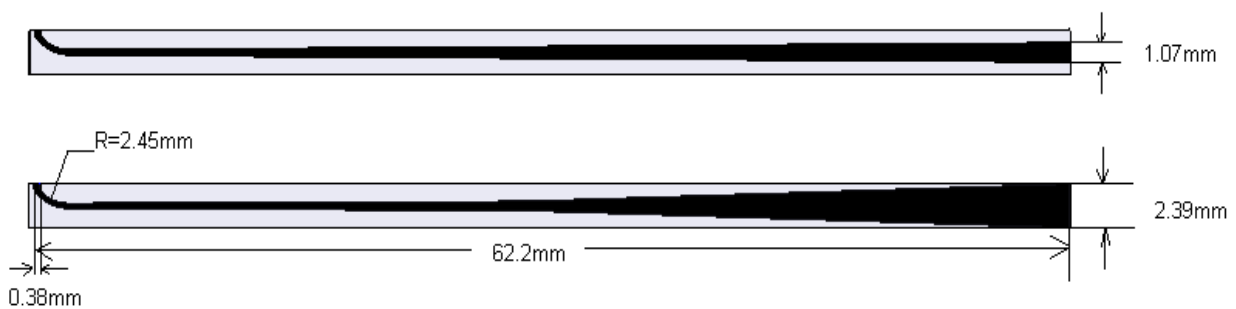
Figure 3.26   Profile of compact balun

Similar to the design of the vertically-oriented balun referred to in section 3.4, this compact horizontally-oriented balun is designed to provide a balanced source with 130 Ω characteristics impedance at differential mode. At the output port for differential mode, E vector directs from one strip line to another, thus these two ports have opposite potentials, while in common mode E heads outward from both strip lines so they have the same potential. The simulated coefficient of transmission from the unbalanced microstrip line input to the parallel strip-line output shows this transition structure permits odd model transmission and simultaneously blocks common mode transmission.

3.5.3 Simulation and measurement

The dual arm spiral antenna with the embedded balun was simulated and optimized using Ansoft HFSS v10.1.3. Its S_{11} was measured using the scalar network analyser. Its gain and radiation patterns were measured in the anechoic chamber room. Figure 3.27 shows the fabricated spiral antenna.
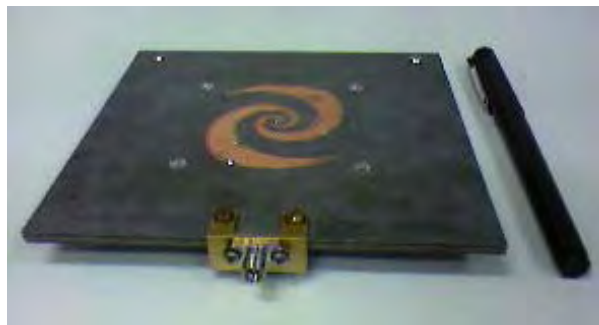
Figure 3.27   The fabricated antenna with the compact balun
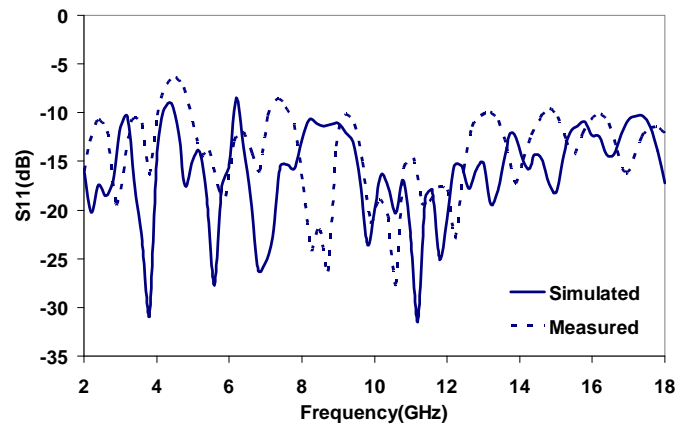
Figure 3.28   Simulated and measured S_{11} of the spiral
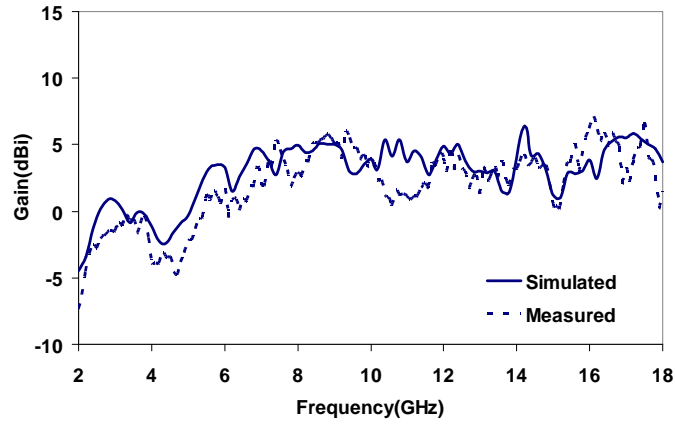
Figure 3.29   Simulated and measured gain of the spiral

Figure 3.28 shows the measured and simulated S_{11} of the spiral antenna. The measured results show S_{11} exceeds slightly -10 dB at several frequency points between 4 GHz and 5 GHz due to impedance mismatch at these frequencies.

Figure 3.29 shows the measured and simulated antenna gain of the spiral antenna which have very similar trend. It can be seen from the measured results that most of the gains are focused between -5 dBic and 6 dBic. From 2 to 6 GHz the measured antenna gain is low, however in the range of $6 - 18$ GHz it keeps above 0 dBic. From the comparison across the entire frequency range, the measured results are close to the simulated ones and the biggest difference is about 5 dB at 11 GHz due to missing including surface wave into the simulation.

(a)

(b)

60

(c)

(d)

(e)
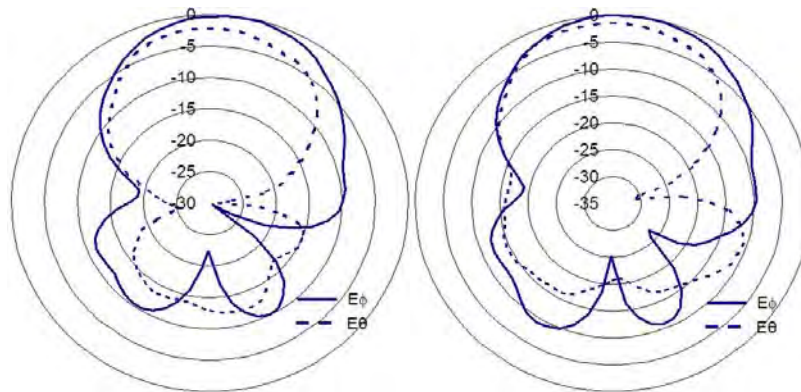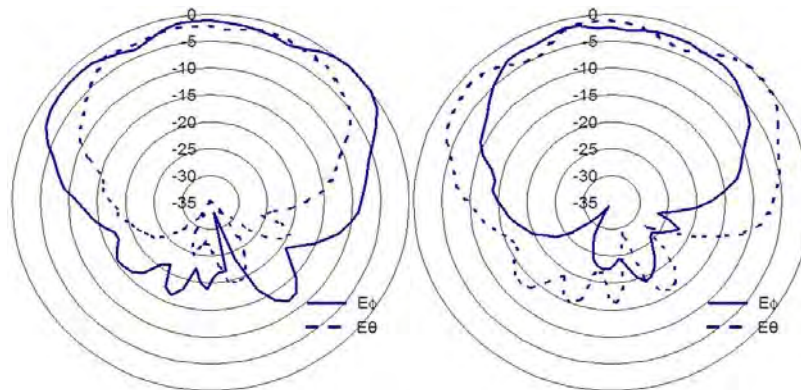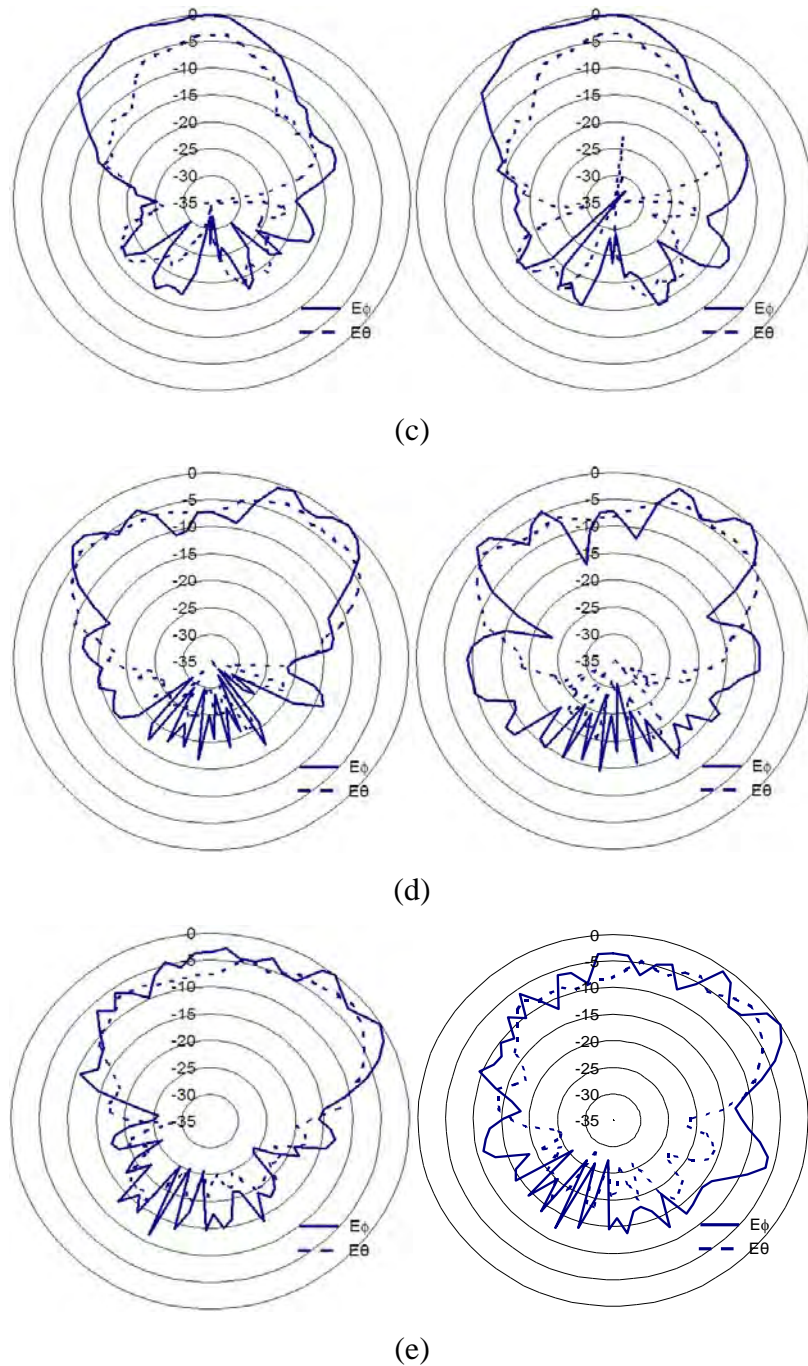
Figure 3.30   The normalised measured E_ϕ and E_θ at ϕ=0 and 90º (a) 2 GHz (b) 6 GHz (c) 10 GHz (d) 14 GHz (e) 18 GHz , left column: ϕ=0, right column: ϕ= 90º

Figure 3.30 (a) ─ (e) are normalised measured radiation patterns of E_ϕ and E_θ at ϕ=0° and 90° cut planes at 2, 6, 10, 14 and 18 GHz. There are some issues with these patterns. The first problem is that the radiation pattern is not symmetric at 14 GHz and 18 GHz, especially at 18 GHz the main beam lobe tilts noticeably. The second issue is that there are several ripples in the radiation pattern when the frequency is above 10 GHz.

The asymmetry at 14 GHz and 18 GHz is caused by the asymmetric balun under the spiral antenna. The simulated radiation patterns of the spiral antenna at 18 GHz with and without balun were compared showing that the presence of the balun affects the symmetry of the radiation pattern. In ϕ =90° cut plane the

balun affects the radiation pattern of the spiral antenna more than that in the $\phi = 0$ cut plane due to the fact of orientation of the balun in this plane.

The ripples in the radiation patterns are believed to be caused by the diffracted surface wave at the edges of the substrate. It is known that surface waves are likely to be excited on thick grounded substrate: in this model the thickness of the substrate is about $1/5$ λ_0 at the highest frequency 18 GHz.

3.5.4 Conclusions

The configuration of a compact dual arm equiangular spiral antenna which incorporates embedded chip resistors and an embedded balun was presented. The chip resistors were arranged according to the loading 'map' obtained from Section 3.5 and the arrangement was further optimised. The compact taper balun, which transforms characteristic impedance and provides balanced source, was embedded in the substrate further reduce the volume of the entire antenna system. The antenna model was simulated, optimised, fabricated and measured and results were presented. This compact spiral antenna is a promising broadband option that meets the initial goals of unidirectional radiation and extreme low profile. Nevertheless, there are problems with this configuration:

1. Asymmetry in radiation patterns especially at high frequency (due to the embedded balun);

2. Distortion in radiation patterns becomes severe when frequency exceeds 10 GHz due to the excited surface wave within the grounded substrate.

Fortunately there are solutions to these problems. The embedded balun can be moved to the back of the ground plane to avoid any effect on the spiral antenna. A thinner substrate may lower the severity of the ripples at high frequencies. This configuration had not been applied to the balun due to mechanic concerns about the balun being mounted onto the back of the ground plane. These solutions can be explored in future.

3.6 Summary

The design of a microstrip spiral antenna working at $2 - 18$ GHz began with the investigation of the radiation physics of dual arm equiangular spirals in the time domain. The cross-talk between spiral arms and the coupling between the spiral and its image in ground plane was identified. Also the current density distribution at steady state at a specified frequency shows the standing wave pattern on a microstrip equiangular spiral. The application of chip resistors to the microstrip spiral was employed to change the resonant characteristics at low frequencies. Hence chip resistor loading rules were developed as an outcome of the investigation. The techniques of applying chip resistors to a spiral configuration were investigated and studied in two stages. The first stage focused on the simulation technique employed with the mixed configuration containing chip resistor and spiral as well as chip resistor arrangement, and was conducted according to the loading rules initiated following investigations of the radiation physics of the spiral antenna. In the second stage, more fundamental investigation about the current behaviour was done in the time domain. The outcome was greater theoretical knowledge about spiral antennas on grounded substrate and practical techniques in spiral parameter optimisation and chip resistor loading.

Subsequently, two dual arm equiangular spiral antennas with embedded chip resistors were developed and measured. Their simulated and measured return loss, gain and radiation patterns were presented. The results show they are promising options for reducing spiral antenna volume ─ especially the spiral with embedded balun ─ compared to a standard cavity backed design. Nevertheless, the distortion in radiation pattern due to the generated surface wave propagating on substrate remains to be solved. The vertical balun added extra depth to the antenna system and the embedded balun tilted the main radiation beam, therefore the problems associated with the balun must also be solved.

Chapter 4 - A nested antenna system

4.1 Introduction

As outlined in Chapter 1, this research aimed to develop a nested antenna system which integrates two RF antennas and their feeding facilities. The main challenge of integration was to create a novel structure in which one antenna is invisible to the other within its own operating frequency range. In Chapter 3, two fabricated microstrip spiral antennas working over the frequency range 2 – 18 GHz were presented. Chapter 4 describes the design, simulation and optimization of another antenna (Antenna II) – physically smaller but operating over the range of high frequency (30 – 40 GHz), and nested to the host antenna system – based on the preceding structural parameter studies. The system integration involved determining the spatial layout of all the components (antenna elements and baluns), suppressing surface waves and minimising coupling between components. In the final section, the performance of the fabricated nested antenna system is measured and the results are analysed.

4.2 Design of a High Frequency Nested Antenna

4.2.1 Studies of the structural parameters

As mentioned in the literature review in chapter 1, the frequency range of 30 – 40 GHz belongs to the Ka band. Antennas designed for this range usually have small dimensions, so the fabrication and design of the antennas and their feeding facilities are difficult. To meet the specifications listed in Section 2.1 of Chapter 2, this antenna may be a spiral, microstrip patch or lens types and all these potential options have been analysed, simulated and compared. It was concluded that an Archimedean spiral is the best candidate that can achieve bandwidth of 10 GHz, wide main lobe and circularly polarisation as well as fit into the footprint of Antenna I.

Before deciding the detailed dimensions of the antenna, the structural parameters of the antenna need to be assessed (similar to the procedure followed for the equiangular spirals in Chapter 3). The curves forming an Archimedean spiral may be described as follows:

$$\rho = \rho_0 + a\phi$$
$$\rho = \rho_0 + w + a\phi$$

(4.1)

In the expressions above ρ is the polar coordinate of any point on the spiral arm corresponding to wound angle ϕ and ρ_0 is the polar coordinate of the starting point of the spiral. The growth rate a is a constant which determines how tightly the spiral is wound up and w is the width of the spiral arm. Because any realistic spiral should be truncated at both ends, ϕ is usually within the range of [0, ϕ_{ed}]. Similar to the equiangular spiral, the inner and outer radius define the upper and lower limit of the operating frequency range of an Archimedean spiral antenna. Spiral diameter should be at least λ/π [87]. The energy will be radiated from the origin outward along the spiral arm as circular polarisation; the amount of energy radiated, relative to the input energy which radiated on the "first pass", is related to the diameter of the spiral. The energy which is not radiated proceeds on to the terminals where it is

reflected and directed back to the origin. Of the energy reflected, some is radiated in the opposite sense. The combination of forward and backward current radiation will form an elliptically polarised field; in extreme case when D<λ/π it is linearly polarised.

Besides ρ_0, a, ϕ, w, parameter s is usually introduced to denote the space between the adjacent arms of any Archimedean spiral. For a dual arm spiral, s is the function of a and w:

$$s = \frac{2\pi \cdot a - w}{3} \qquad (4.2)$$

The number of turns n into which a spiral is wound is introduced to depict the size of an Archimedean spiral antenna and n relates to ϕ_{ed} as follows:

$$n = \frac{\phi_{ed}}{2\pi} \qquad (4.3)$$

Normally a spiral should be tightly wound to ensure the first radiation active zone is limited to a small area, thus w and s should be as small as possible. However, when s is too small the coupling between adjacent arms may become significantly stronger which causes slower decay of the current flowing along the spiral arm and makes bandwidth of the antenna narrower. Furthermore $\rho_0 = w = s$ should be specified to a spiral to meet the requirement of being self-complementary and may achieve constant input impedance [86]. It should be noted that the Archimedean spirals investigated in this chapter all are the self-complementary antennas.

4.2.1.1 Microstrip dual arm spiral

As introduced in Chapter 3, a microstrip spiral radiates unidirectional owing to the ground plane blocking backward radiation. The supporting substrate of a microstrip antenna must be thin enough and its permittivity should be low enough not to induce any higher mode surface waves. Thus in addition to the structural parameters a, w ($= s = \rho_0$), n (or ϕ_{ed}) of the spiral, d, ε_r of the substrate should be of concerns as they also affect the radiation performance of the microstrip spiral.
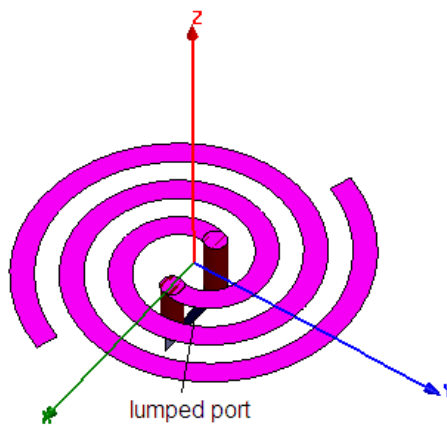
Figure 4.1   Dual arm spiral model

Figure 4.1 shows a dual arm spiral model simulated in HFSS. The curves forming the spiral are expressed by (4.1). Its progressive length L is expressed as:

$$L = \int_0^{\phi_{ed}} (1.5w + a\phi)d\phi = \frac{3}{2}w \cdot \phi_{ed} + \frac{1}{2}a\phi_{ed}^2 \qquad (4.4)$$

Accordingly ϕ_{ed} can be expressed using L:

$$\phi_{ed} = \frac{\sqrt{\frac{9}{4}\pi^2 + \frac{4L\pi}{w}} - 1.5\pi}{2} \tag{4.5}$$

The structural parameters involved are w, a and ϕ_{ed}. If the width of arm equals the space between arms then growth rate, ϕ_{ed}, is dependent on width, w, thus only two parameters, w and ϕ_{ed}, are of concern.

—0.2mm	
—0.25mm	
—0.3mm	
—0.35mm	
—0.4mm	
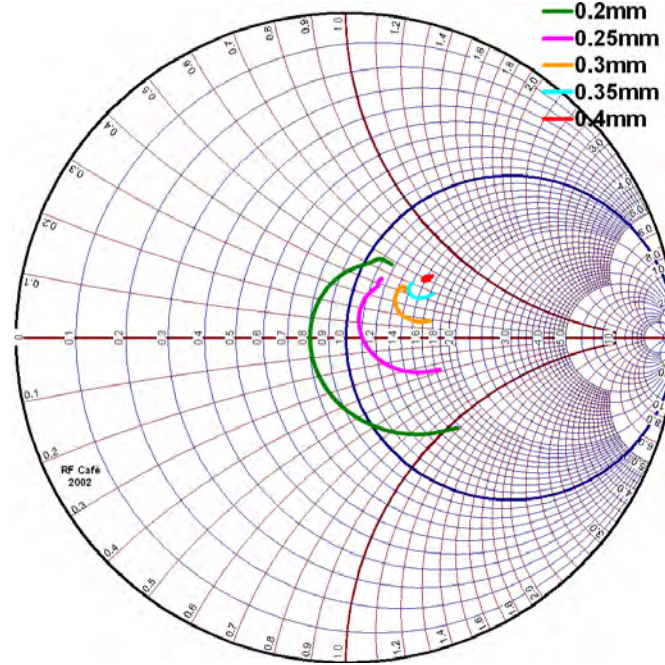
Figure 4.2   The input impedance of the spirals with varying arm width w

Figure 4.2 shows the input impedance of the spirals with different w in a smith chart normalised to 177 Ω. When w increases the impedance locus becomes smaller. The impedance locus of all the spirals except the one with $w = 0.2$ mm are within the circle representing return loss of 10 dB. If w is within $0.3 - 0.4$ mm, the reactance part of the input impedance of the spiral is pure inductance. From the dependence pattern of the input impedance of the spiral to its width w it can be concluded that the input impedance is sensitive to the minor change of the width w and it is not difficult to find out the optimum value by evaluating its impedance response in smith chart: all the spirals except the one with $w = 0.2$ mm are potential options.

Figure 4.3 shows the strength of the far zone total radiated electric field E_{total} (dB) versus azimuth angle θ varying from $-90°$ to $90°$. At the bore-sight direction E_{total} of all the spirals had similar magnitude in both ϕ cut planes and the difference of E_{total} is less than 1 dB. However at the end-fire directions ($\theta = -90°$ or $90°$) in both ϕ cut planes E_{total} of these spirals were significantly different. In $\phi = 0$ cut plane $w = 0.3$ mm has the strongest end-fire direction radiation and $w = 0.2$ mm is listed at the bottom. But in $\phi = 90°$ cut plane $w = 0.2$ mm or 0.4 mm ranks top of the list and $w = 0.3$ mm displays the lowest end-fire radiation. The difference of E_{total} between any two spiral options ranges from 2 dB to 8 dB. Thus from Figure 4.3 it can be seen that w affects the radiation along end-fire direction much more than the bore sight direction.
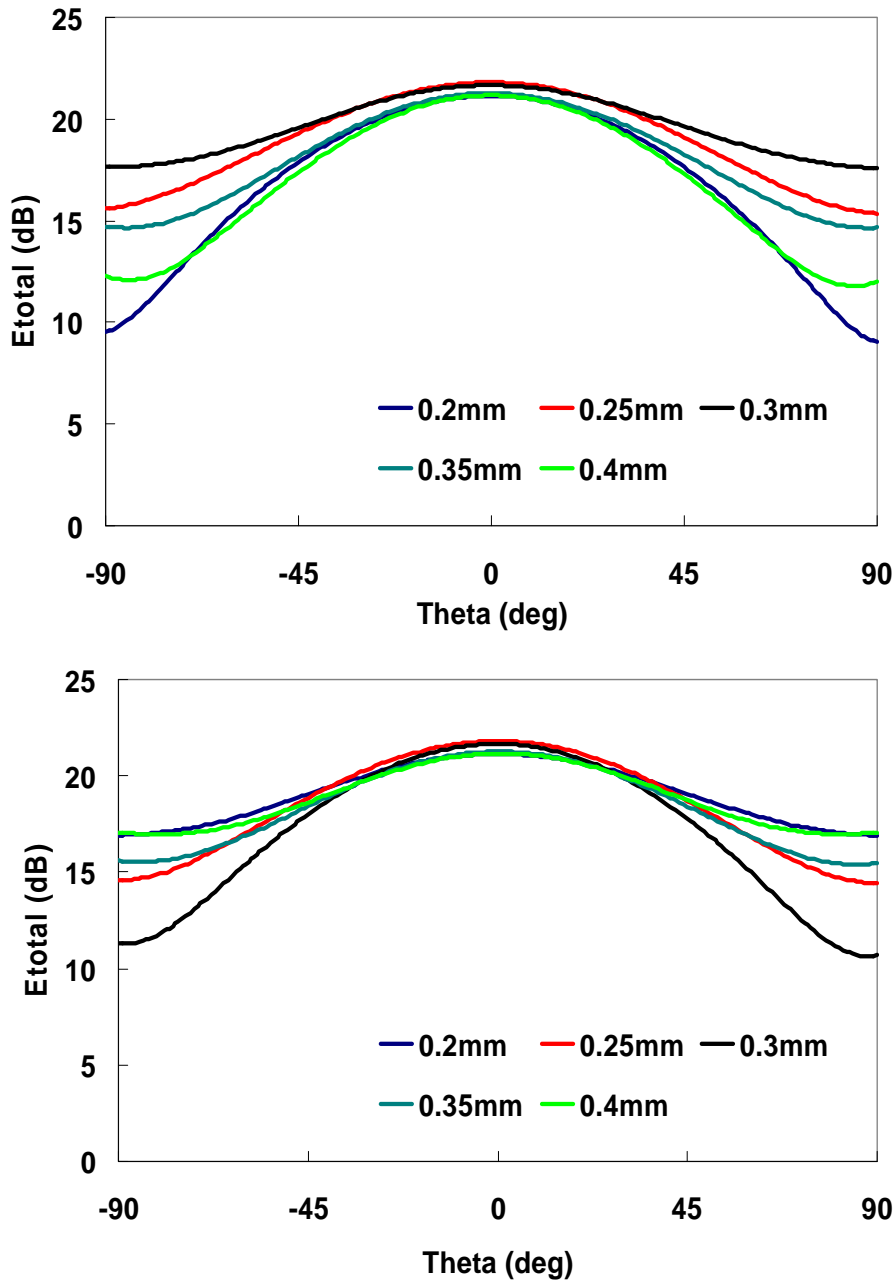
Figure 4.3   Radiation pattern of the spirals with varying *w* at 30 GHz (a) in $\phi = 0$ (b) in $\phi = 90°$ cut planes

A spiral with variable *L* and constant *w* is also investigated. Figure 4.4 shows the input impedance of the spirals with *L* of $1\lambda_0$, $2\lambda_0$, $3\lambda_0$ (denoted by "1 lambda", "2 lambda", "3 lambda" in the chart) within 30 – 40 GHz. The spirals with length *L* of $2\lambda_0$ and $3\lambda_0$ have very tight impedance locus over the frequency range compared to the one with *L* of $1\lambda_0$. The pattern demonstrates that the input impedance of the spiral is sensitive the change of *L* if it is not long enough. When *L* increases to a certain value, further increasing does not change the impedance response significantly. The conclusion may be used to help deciding the proper length for the spiral to achieve the certain impedance bandwidth.

67
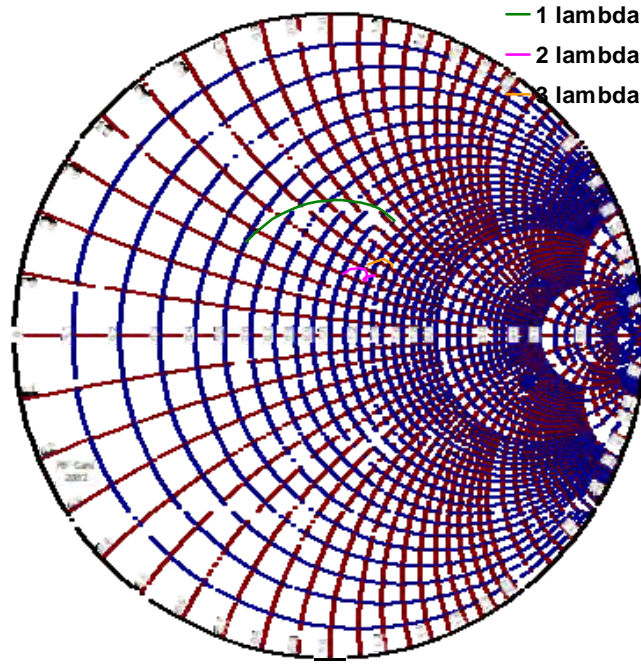
Figure 4.4   Input impedance of the spirals with w =0.3 mm and varying L

The far zone radiation E$_{total}$ of the spirals with fixed w and variable L show the similar pattern that at bore-sight directions the radiated power does not change significantly with L but it does at end-fire directions.

The preceding section described the investigation about the two parameters, w and L of dual arm Archimedean spirals in free space. It can be concluded that the input impedance is closely related to w and L. The increment of w and L both may tighten the impedance locus; however, they may affect radiation along end-fire direction significantly but only slightly affect the bore-sight radiation.

Considering dielectric substrate was involved with the design, it is necessary to explore how the presence of substrate affects the radiation behaviour of Archimedean spiral above ground plane. In this situation, the spiral with L =10 and w =0.3 mm is under investigation.

Several substrate of identical dielectric material with different thickness have been simulated. Similar to the impedance response of equiangular spiral antenna referred in Chapter 2, characteristics impedance of this Archimedean spiral on dielectric material compared to value in free space. Similarly the relationship between Z$_e$ and Z$_0$ within 30 − 40 GHz is described as:

$$Z_e = \frac{Z_0}{\sqrt{\varepsilon_{eff}}} \qquad\qquad (4.6)$$

Input impedance versus frequency and far zone total electric field versus azimuth angle θ on ϕ=0, 90° cut planes for different w were simulated and analysed. It was concluded that the input impedance of the spiral was very sensitive to w and it achieved very stable impedance response if w was within the range 0.25 − 0.35 mm. In radiation patterns, at any frequency radiated power level at bore-sight direction (θ = 0) is much more dependent on to w than at end-fire direction (θ = 90°).

As noted above, an antenna which works over 30 – 40 GHz may excite a high mode surface wave on or inside thick substrate. For a 1.575 mm thick RT/Duroid 5880 substrate, TE$_1$ cut-off frequency is 43.5

GHz. In order to determine the contribution of the surface wave to the radiation pattern of the dual arm Archimedean spiral antenna, four different thickness options — 0.508 mm, 1.016 mm, 2.032 mm and 2.54 mm – were considered.

(a)

(b)
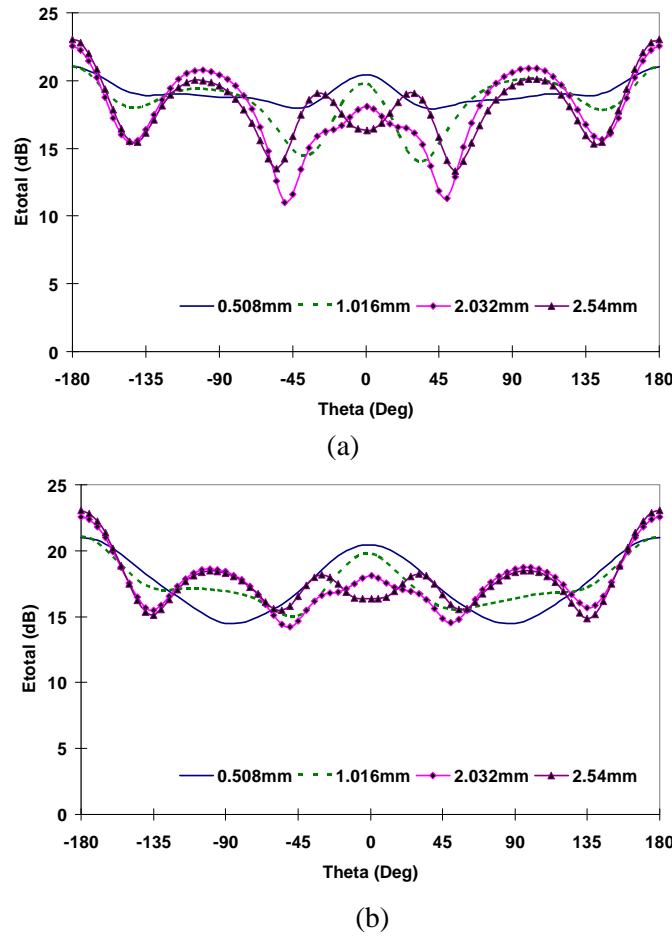
Figure 4.5   Radiation patterns of the spiral at 30 GHz (a) in ϕ=0 (b) in ϕ=90° cut plane

Figure 4.5 shows the radiation patterns of the Archimedean spiral on these substrates at 30 GHz in two ϕ cut planes (ϕ=0, 90°). It is interesting to see that the radiation at θ =±180° was stronger than that at bore-sight direction (θ = 0). θ = ±180° is backward direction going through the substrate. This asymmetric energy distribution implies that dielectric plate magnifies the radiation passing through: this may be explained as that dielectric material enlarges the electric length of any conducting object attached on it so that the effective radiation area is bigger than its physical size. The magnifying ratio depends on the permittivity and thickness of the substrate and the electric length of spiral (L/λ_0). For example, when the substrate is only 0.508 mm thick, the magnifying ratio is 2 (when L/λ_0 =1.3) and it becomes more than 4 for 2.54 mm thick substrate.

It can be concluded from the information revealed above that when dielectric substrate is involved the radiation patterns of the spiral may be distorted as ripples appear due to surface wave. In the meantime, radiation at bore sight may be magnified at a certain ratio depending on relative permittivity and thickness of the substrate. This conclusion may be useful for the determination of with initial value range of these parameters for further design

69

4.2.1.2 Dual arm spiral with cavity

As indicated above, grounded substrate does cause surface wave problem with Antenna II in Ka band. To avoid ground plane being placed close to Antenna II, an Archimedean spiral backed by a cavity is a very good solution. The spiral has to be etched on dielectric board (RT/Duroid 5880) and the substrate with thickness of 0.254 mm is strong enough to support the antenna. For the intended frequency range, 30 – 40 GHz, the size of cavity will not add extra dimension to the host antenna system even if it is a quarter of wavelength at the lowest frequency (the depth of the conventional cavity). As explained in section 4.2.1.1, when the width of spiral arm w is 0.3 mm and the total length L is 3 wavelengths of the lowest frequency (30 GHz), it achieves very good impedance bandwidth and radiation patterns. Since a cavity is proposed, its depth H is a new parameter.

Usually the cavity has the depth H of a quarter of wavelength at the centre frequency of the proposed frequency range. However, in this design the balun is required to feed the dual arm spiral operating over 30 – 40 GHz thus the restriction on the length of the balun is a half of wavelength at the lowest frequency (in this design the length is at least 5 mm). The spiral with a set of cavity whose depth H varies from 5.1 mm to 7.5 mm were investigated. In the smith chart – Figure 4.6 – the impedance locus of these models show that the locus is more and tighter with depth increasing. The response of the spiral with 6.7 mm deep cavity achieves the tightest impedance locus and its return loss should be below –10 dB over the entire range of 30 – 40 GHz. However, when H increases further the loop becomes loose again (not shown).
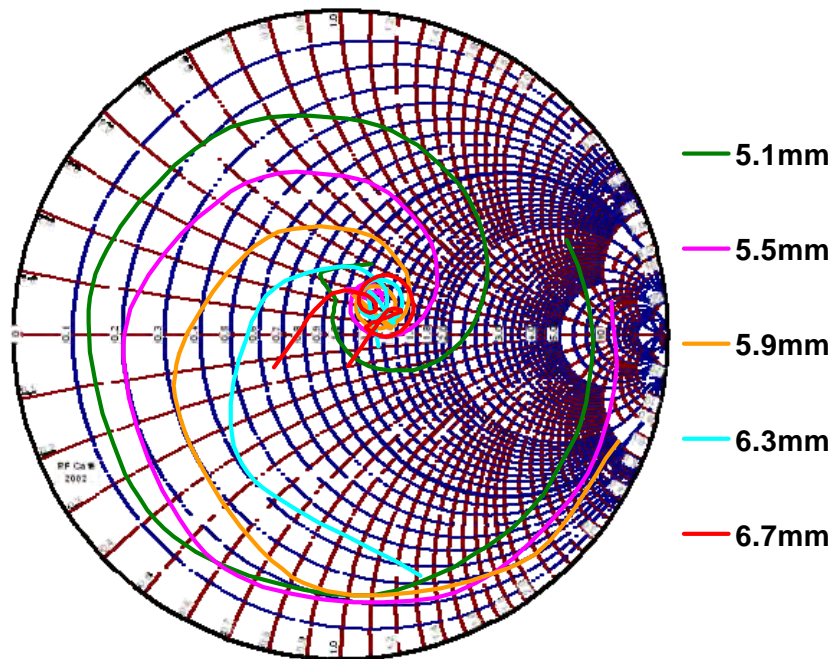
Figure 4.6   The effect of H on the input impedance of the dual arm spiral with cavity
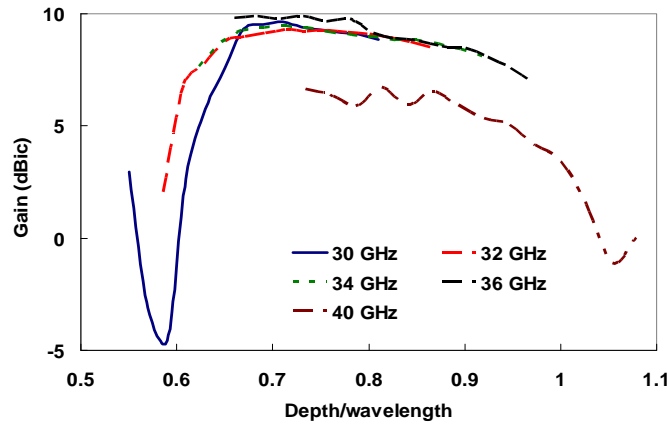
Figure 4.7   The effect of **H** on antenna gain of the dual arm spiral with cavity

H also changes antenna gain of the spiral. Figure 4.7 displays antenna gain of the spiral versus **H** (normalised by wavelength). In this chart, the simulated antenna gain of the spirals at the five frequencies (30 GHz, 32 GHz, ...,40 GHz) are shown and the results of five frequencies are sufficient to produce correct conclusion that is, to obtain stable antenna gain **H** should be within $0.7\lambda_0$ and $0.9 \lambda_0$. Accordingly **H** should be within the range of 5.25 – 6.75 mm.

4.2.2 The design of Antenna II

(a)

(b)   (c)
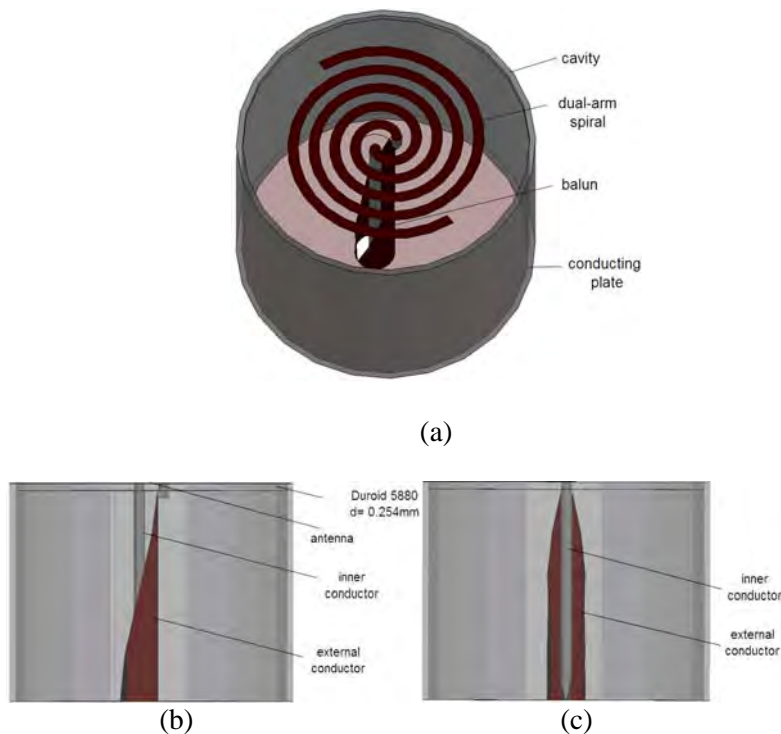
Figure 4.8   The configuration of the dual arm spiral with cavity (a) 3-D view of Antenna II including the cavity (b) (c) the side view of the balun of Antenna II

In order to avoid surface wave, in the meantime, and to achieve broad impedance bandwidth, the ground plane was placed far away from the spiral. Antenna II was designed as the dual arm Archimedean spiral backed by a cavity inside which the balun is placed. The cavity has another advantage which is that the cavity may avoid mutual coupling between Antenna I and Antenna II. Figure 4.8 displays the configuration of the dual arm spiral with the cavity.

71

Duncam type [78] developed utilizing a semi-rigid coaxial cable. Its external conductor is cut open whose cross-sectional view shows a sector removed. Along the rotation axis of the coaxial cable the removed sector varies from $\frac{1}{6}\pi$ to $1\frac{5}{6}\pi$ yielding the transition to a two-conductor line where characteristics impedance gradually changes from 50 Ω to 125 Ω. If the outer conductor is rolled off onto a plane, it becomes an isosceles trapezoid with two parallel sides of 0.35 mm, 4.21 mm and 6.7 mm high.

The investigation about the structural parameters of the Archimedean spiral has already given the value ranges for w, r_0, L of Archimedean spiral, thickness, ε_r of substrate and H of cavity. The overall optimisation of the spiral with all these parameters considered was conducted and the simulated results are displayed in Figure 4.9 and Figure 4.10 as follows.
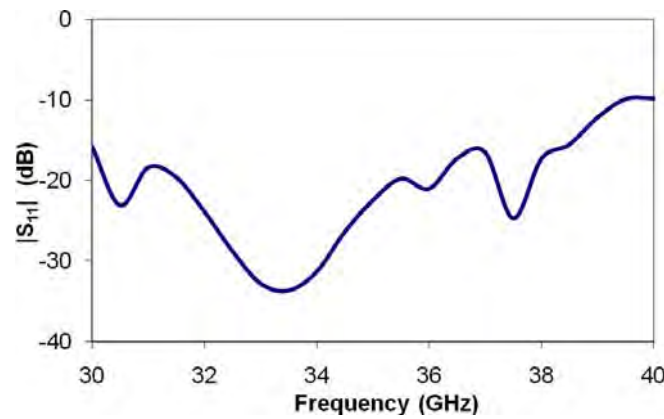
Figure 4.9   The simulated $|S_{11}|$ of the dual arm spiral with cavity
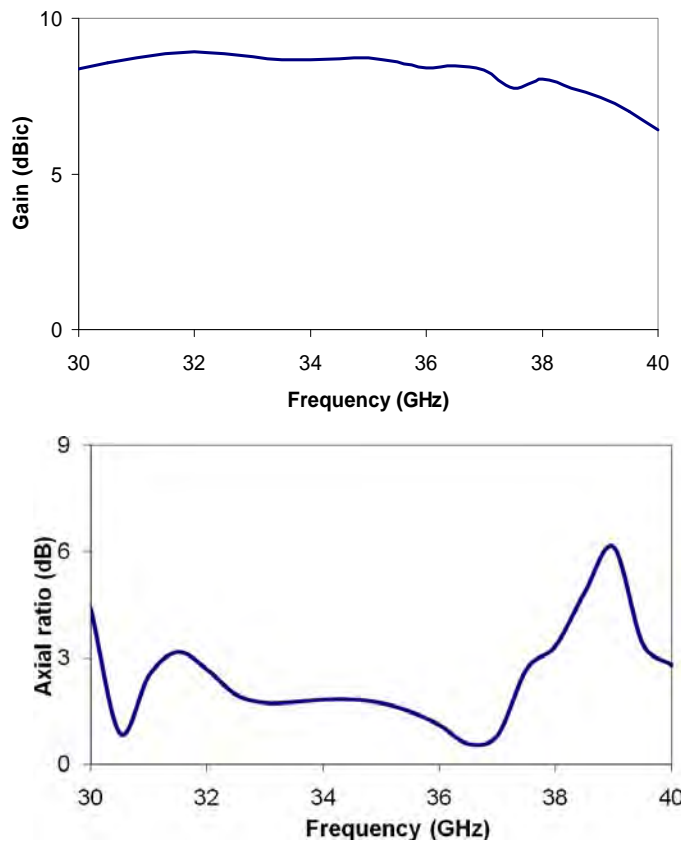
Figure 4.10   The simulated gain and axial ratio of the dual arm spiral with cavity

It can be seen that this antenna design has satisfactory S_{11} and fairly flat antenna gain with variation of only about 2 dB and its axial ratio is below 3 dB over about 3/4 of the frequency range.

(a)

(b)

(c)
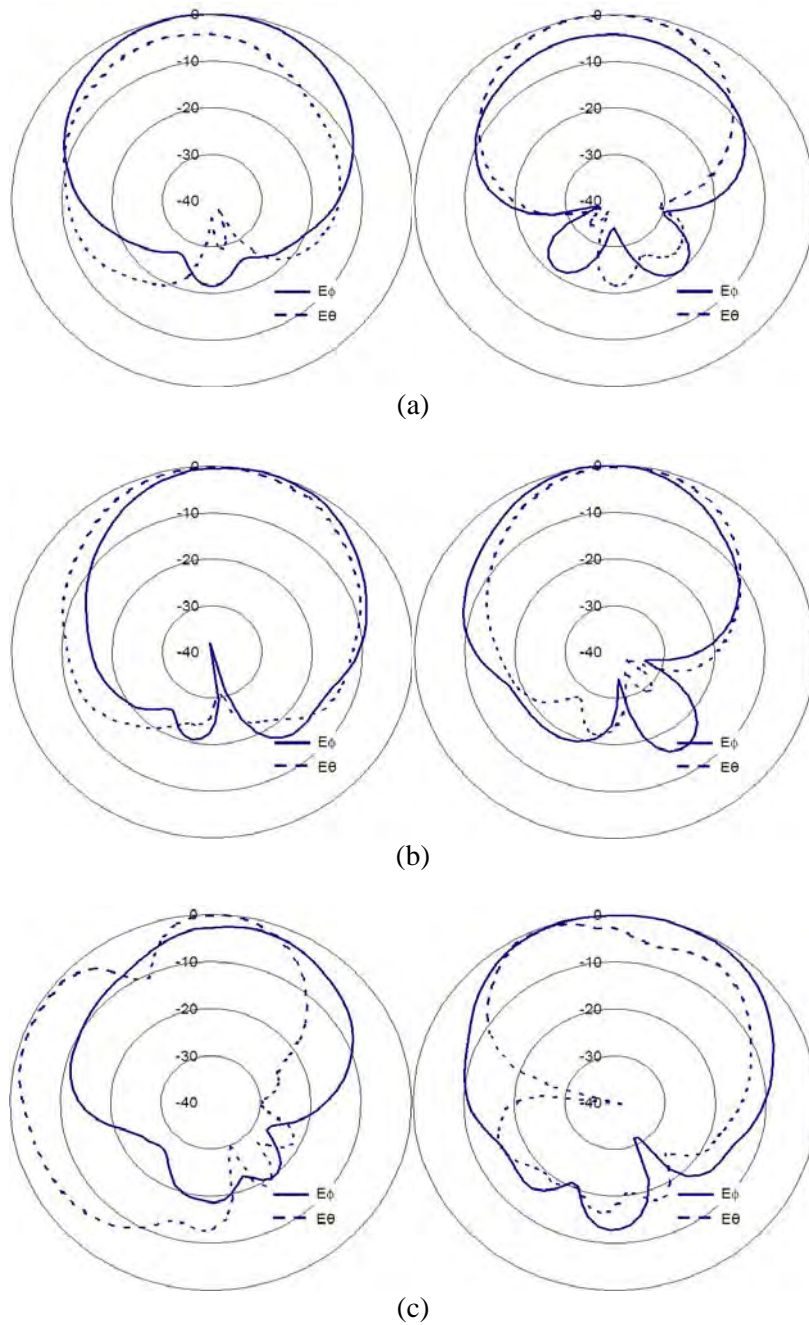
Figure 4.11   Normalized simulated E_ϕ and E_θ of the dual arm spiral with cavity at $\phi=0$, 90° cut planes

(a) 30 GHz (b) 35 GHz (c) 40 GHz

Figure 4.11 displays normalised simulated results of the far zone radiated electric field versus azimuth angle θ at two orthorgonal planes ($\phi=0$ and 90º). The spiral has achieved non-ripple radiation patterns at all indicated frequencies owing to the thin dielectric substrate and ground plane's being far underneath. However, the main lobe in the radiation pattern at 40 GHz is asymetric due to asymetric structure of the balun.

4.2.3 Conclusion

Through extensive exploration about structural parameter of Archimedean spiral antenna and cavity parameter, the simulated results of the designed Antenna II show that this dual arm spiral with cavity achieves the requested impedance bandwidth (30-40 GHz), good antenna gain (6-8 dBic) axial ratio of better than 4 dB, and non-distorted radiation patterns. Although at 40 GHz the spiral shows asymmetric radiation pattern due to asymmetry of its balun. The results are comparable with previously published spiral antennas.

4.3 Implementation of the nested system

4.3.1 Modification of the balun for Antenna I

As demonstrated in Chapter 3, the horizontally oriented balun for the second fabricated model has solved the problem of extra dimension caused by the vertical balun. Thus this design was subsequently applied to the nested configuration. The embedded balun deteriorates the symmetry of the radiation pattern of the spiral antenna especially at higher frequencies (above 10 GHz) but this problem may be solved by moving the balun from the slot inside the substrate to the back of the ground plane. The size of the balun itself is not a problem as it adds only about 3 mm extra height to the system.

The balun extended the previous curved output parallel strip lines to fill the increased gap between spiral and balun and its supporting dielectric slab needed to be modified accordingly. If the balun is placed underneath the ground plane, there should be a clearance in the ground plane allowing the feeding probes to go through. The critical parameters for this clearance are radius of clearance r_c and spatial coordinate x_c, y_c of clearance centre.

Figure 4.12   The configuration of the modified balun

Figure 4.14 shows the proposed modified balun for antenna I. The grey coloured parts are made of dielectric material Rogers RO4003 with thickness of 0.508 mm and relative permittivity of 3.38. The dark brown parts are thin conducting copper sheet laminated on Rogers RO4003.

4.3.2 System integration

In Chapter 3, two fabricated antennas with embedded chip resistors were introduced. One is fed by the vertical testing balun and the other uses an embedded balun. The latter is the better candidate to be nested to the antenna system, as displayed in Figure 4.13.

the small circular plate

Antenna #1

the balun for
Antenna #1

Antenna #2 and balun

(a)

(b)
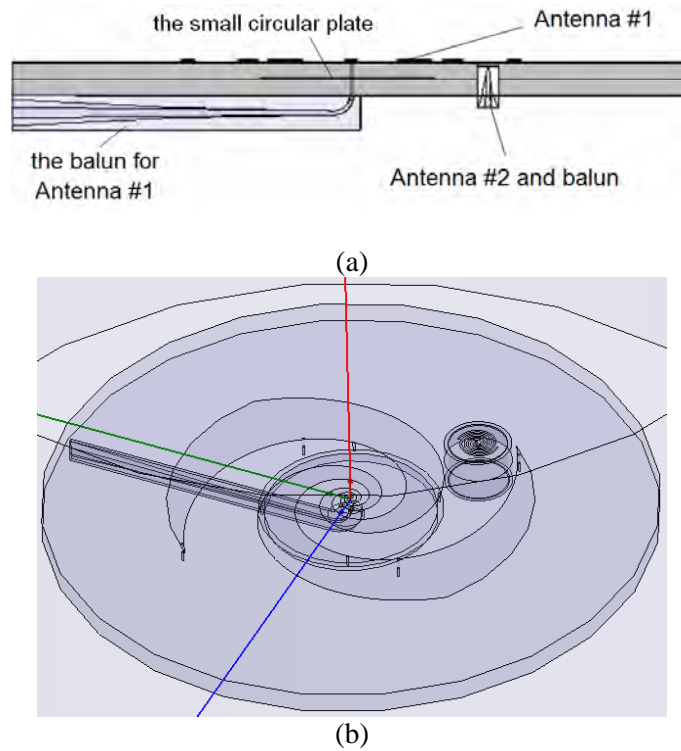
Figure 4.13   The configuration of the nested antenna system (a) side view (b) 3D view

The substrate on which Antenna I is located consists of three RT/Duroid 5880 layers and its total height is 3.658 mm. One of the layers is 0.508 mm thick and the others are 1.575 mm each. As shown in Figure 4.13 (a), the modified balun for Antenna I is underneath the ground plane. Antenna II is under the top thin dielectric layer and partly protruding from the ground plane. In addition, a small conducting circular plate is sandwiched between the two identical dielectric layers. Antenna I is loaded by four pairs of chip resistors loaded for each arm. Two pairs of them are shorted to the small conducting plate. In Figure 4.13 (b) shows that Antenna II is located between the two arms of Antenna I. The determination of the location was optimised based on the overall radiation performances of Antenna I and II.

The small circular conducting plate acts as the ground plane for the part of Antenna I and the lower ground plane takes care of the rest part of Antenna I. The stepped structure provides Antenna I with two different thickness of substrate. At high frequencies (between about 10 GHz and 18 GHz) the small conducting plate takes effect due to the small radiating zone around the centre of the spiral. As a result, the radiation patterns of Antenna I within this frequency range may be less distorted owing to thin dielectric substrate involved. At low frequencies (between 2 and 10 GHz), when the travelling current on Antenna I goes beyond the area above the small conducting plate, the low conducting plate starts to act as the ground plane for Antenna I. Hence at these frequencies the substrate working for Antenna I has twice thickness of the substrate in previous case. Thicker substrate increased the antenna gain at these frequencies. Although the small ground plane decreased antenna gain over the high frequency range, this reduced the variation between the maximum and minimum antenna gain compared to a substrate of uniform thickness. Nevertheless, this special configuration may cause a problem: the abrupt discontinuity of the small conducting plane may distort the radiation patterns.

To minimise these negative effect it is critical to determine the appropriate size of the small conducting plate based on the selection criteria: better return loss, more flat antenna gain vs. frequency

and smoother radiation patterns. Different radii – 12 mm < r < 17 mm – were simulated and r = 14 mm was selected as Antenna II has the most flat antenna gain versus frequency and the smoothest radiation patterns when r = 14 mm. In addition, it is also important to select the location where Antenna II is nested. The coupling between these two antennas should be considered. Through repeated simulation and optimisation the premium location for small antenna has been determined.

The size of the circular clearance in the low ground plane determines the characteristics impedance of the horizontally oriented balun at the feeding location thus it should be tuned to ensure the balun match the input impedance of the spiral.

4.3.3 Surface wave issues

Surface waves decrease the useful antenna radiation thus they reduce radiation efficiency and gain of antennas and also cause distortions in the radiation patterns, such as ripples and strong end-fire radiation or backward radiations.

There are many types of solutions to mitigate surface waves with microstrip antennas. One of the solutions is to remove part of the substrate underneath the antenna using micromachining technology [87]. Another approach is to arrange periodical loading for the substrate so that the surface wave dispersion diagram presents a forbidden frequency range about the antenna's operating frequency. In both solutions, surface wave cannot propagate so that more power is coupled to the radiated wave.

A periodically distributed EBG structure acts as a distributed LC (inductor and capacitor) network with resonant frequencies which are determined by the physical size of the lattice and the parameters of the substrate. Around the resonant frequencies, the surface impedance of the EBG array is very high so that it blocks the flow of surface waves. The centre frequency of the equivalent LC network is determined by:

$$f = \frac{1}{2\pi\sqrt{LC}} \qquad (4.17)$$

| (a) | (b) | (c) |
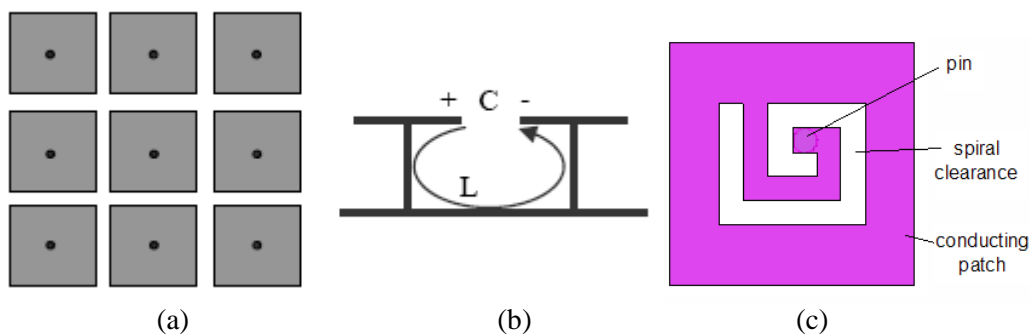
Figure 4.14   (a) A conventional EBG structure; (b) equivalent circuit of EBG structure; (c) the EBG structure with spiral aperture

Figure 4.14 (a) shows the conventional EBG structure on a grounded substrate. It is an array of square patches which are all shorted through the pins. In an EBG element array, the gap between the adjacent conducting patches introduces capacitance (C) and the pin provides inductance (L). The entire array can be described as an equivalent LC circuit, as shown Figure 4.14 (b).

Figure 4.14 (c) shows a novel EBG element profile [88]. Its operational mechanism is similar to that of conventional EBG structure. In this novel configuration the spiral branch replicates the performance of

a coplanar spiral inductor. Compared to the solid patch, the patch with spiral aperture has wider impedance bandwidth. Additional inductance is introduced by the branch and cascaded with the inductance formed by the plated via. It is easy to adjust the inductance amount by changing the windings of the spiral branch, e.g. by increasing the windings more inductance will be introduced.
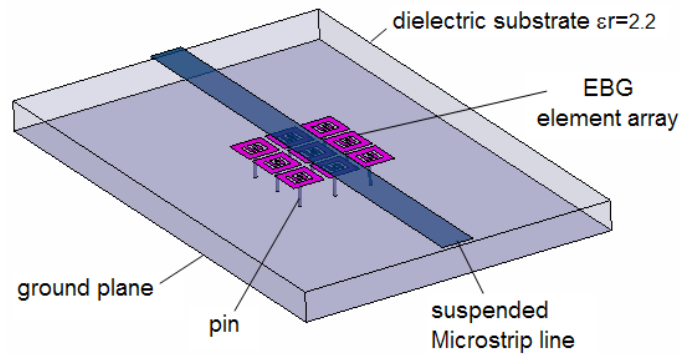
Figure 4.15   The suspended microstrip line with 3*3 EBG element array
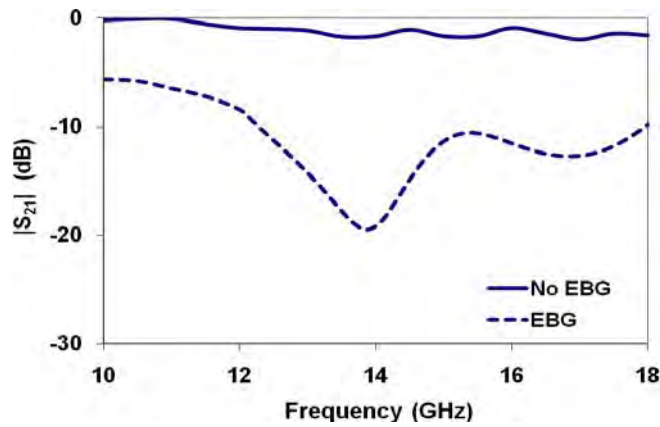
Figure 4.16   Simulated $|S_{21}|$

The suspended microstrip line measuring method [89] is usually employed to check if the EBG elements would stop surface wave propagating within proposed frequency range. As seen in Figure 4.15 the microstrip line is suspended above the 3*3 EBG element array and its simulated transmission coefficient S_{21} (dB) is indicated by the dashed line in Figure 4.16. The solid line indicating S_{21} of the suspended microstrip line without any EBG elements is the reference. Compared to this, S_{21} of the suspended line is much lower, below – 10 dB particularly from 12 GHz to 18 GHz, while EBG elements are present. This demonstrates that the EBG array efficiently prevents surface waves from propagation on the interface between air and dielectric material.

Using an EBG array introduces significant complexity to the fabrication of the antenna system. For example, thousands of shorted pins have to be inserted to the substrate. In order to simplify the fabrication, in this design, a two-row array of EBG elements was only arranged along the edge of the circular substrate of Antenna I for the purpose of reducing the contribution of surface waves to the end-fire directions at high frequencies (12 – 18 GHz). As shown in Figure 4.17, the EBG element was modified from a rectangle patch to one formed by arcs and straight lines.
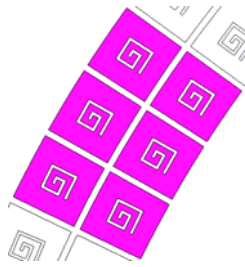
Figure 4.17   The curved edged EBG elements

The simulated results of the curved EBG elements were similar to that displayed in Figure 4.16. Therefore these modified EBG elements may be introduced to the nested antenna system to partly solve surface wave problem.

4.4 Fabrication and measurement

Figure 4.18   The fabricated nested antenna system

Figure 4.19   The fabricated balun for Antenna II

Figure 4.18 show both the front and the back pictures of the fabricated nested antenna system. Along the verge there are two rows of curved EBG elements (referred to the schematic profile in Figure 4.17). The external row of EBG elements were soldered to the ground plane of the antenna system by edges. On the back of Antenna I the modified horizontally oriented balun feeds Antenna I through the clearance in the small ground plane. Antenna II and its cavity were placed inside the substrate of Antenna I. The cavity of Antenna II was soldered to the ground plane. The balun of Antenna II was fabricated on the semi-rigid cable followed by K-connector. The small ground plane (referred to 4.3.2) and the big ground plane were soldered together. Figure 4.19 shows the fabricated balun for Antenna II.

The fabricated nested antenna system was measured separately within two frequency ranges. For 2 – 18 GHz, a 20 GHz Vector Network Analyser (VNA), two double-ridged horn antennas (working range up to 20 GHz) and the anechoic chamber room facilitated measuring antenna gain and radiation patterns. Within 30 – 40 GHz, a 40 GHz signal generator, spectrum analyser and two double-ridged horn antennas ETS LINDGREN Model 3116 were employed to measure antenna gain and radiation patterns. In the latter case, the horn antenna was 50 mm away from the tested antenna. This distance meets the far field condition (distance $\gg D^2/\lambda$, D ~ 12 mm, λ=10 mm for 30 GHz). In addition, some microwave absorbing foam was put behind the tested antenna to reduce the background noise.

(a)   (b)
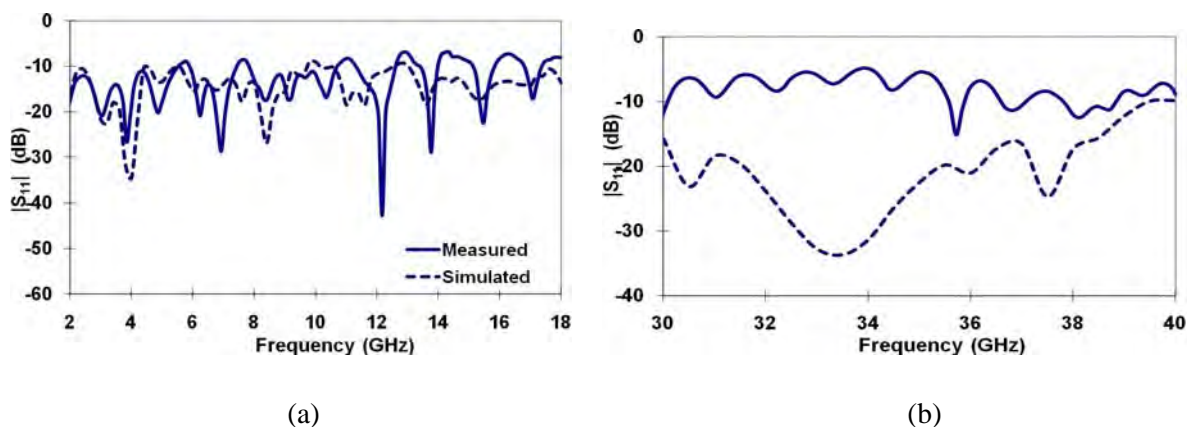
Figure 4.20   Measured and simulated S_{11} of nested antenna

Figure 4.20 (a) and (b) display the measured and simulated reflection coefficient ($|S_{11}|$) of the nested antenna system over 2 – 18 GHz and 30 – 40 GHz. The S_{11} of Antenna I is below −10dB over the majority of the frequency range. At 5.6 GHz, 7.6 GHz and within 10.8-11.1 GHz, 12.6 – 13.3 GHz, 14 – 15 GHz, 16 – 16.7 GHz and 17.4 – 18 GHz S_{11} is slightly above −10 dB. Over the frequency range of 2 – 10 GHz the measured and simulated results are close and the minor difference (less than 5dB) can be seen

at several frequencies. When the frequency is around 13 GHz, or within the range of 14.2 – 15.5 GHz or around 17 GHz, the measured S_{11} is higher than the simulated values by 5 – 6 dB due to the inaccuracy in fabrication.

Within the range of 30 – 40 GHz, the measured S_{11} of Antenna II is much higher than simulated results and at many points S_{11} is above −7 dB. This was determined to be a mismatch between the impedance provided by balun and the input impedance of Antenna II.

The fabrication of Antenna II is a difficult and complex procedure, which requires high accuracy in applied fabrication techniques. Over this frequency range, the antenna and the balun are both of small size and any minor offset to the designed value may cause big difference in electric performance. First of all, the external conductor was cut open and the size of the removed area should gradually increase linearly. Using a semi-rigid cable is difficult to make the linear change in the size of the removed area by manually cutting the conductor. The accumulated inaccuracy may make the impedance at the output end of the balun different to the simulated value. Secondly, the energy coupling from the balun to the Archimedean spiral is very sensitive to the connection between the balun and both arms of the spiral. If the connection contains extra solder, it may cause the discrepancies between the measured and simulated results.
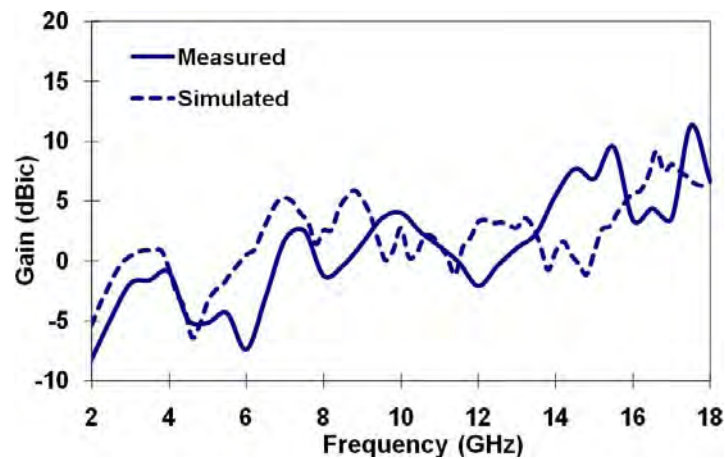
(a)
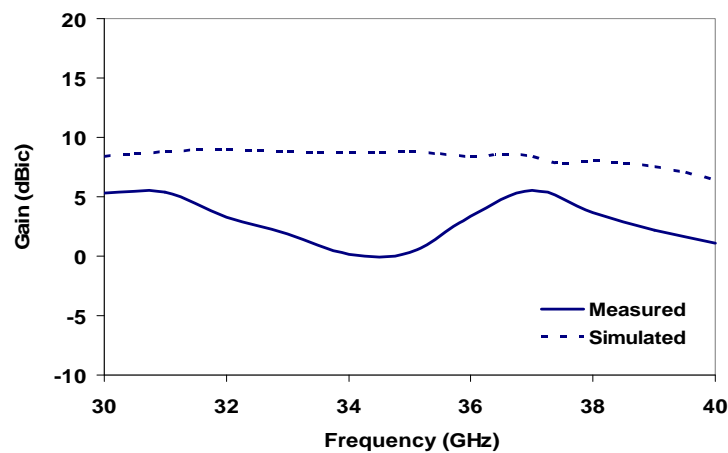
(b)

Figure 4.21   The measured and simulated antenna gain of the nested antenna (a) 2 − 18 GHz (b) 30 − 40 GHz

Figure 4.21 shows the measured gain of the nested antenna system, for 2 – 18 GHz and 30 – 40 GHz. It can be seen that over the frequency range of 2 – 7 GHz the total antenna gain is low, and it starts to rise above 0 dBic beyond 7 GHz. At about 12 GHz the gain drops to about −1 dBic. This antenna gain pattern is similar to that of the fabricated antennas introduced in Chapter 3. As analysed in section 4.3.2, the small ground plane will make the antenna gain drop slightly at high frequency (from 10 to 18 GHz). The measured antenna gain is higher than that expected within the range of 14 – 18 GHz. At 30 – 40 GHz the simulated antenna gain is relatively flat. Measured results show that around 34.5 GHz the gain of Antenna II drops as low as 0 dBic.

(a)

(b)

(c)
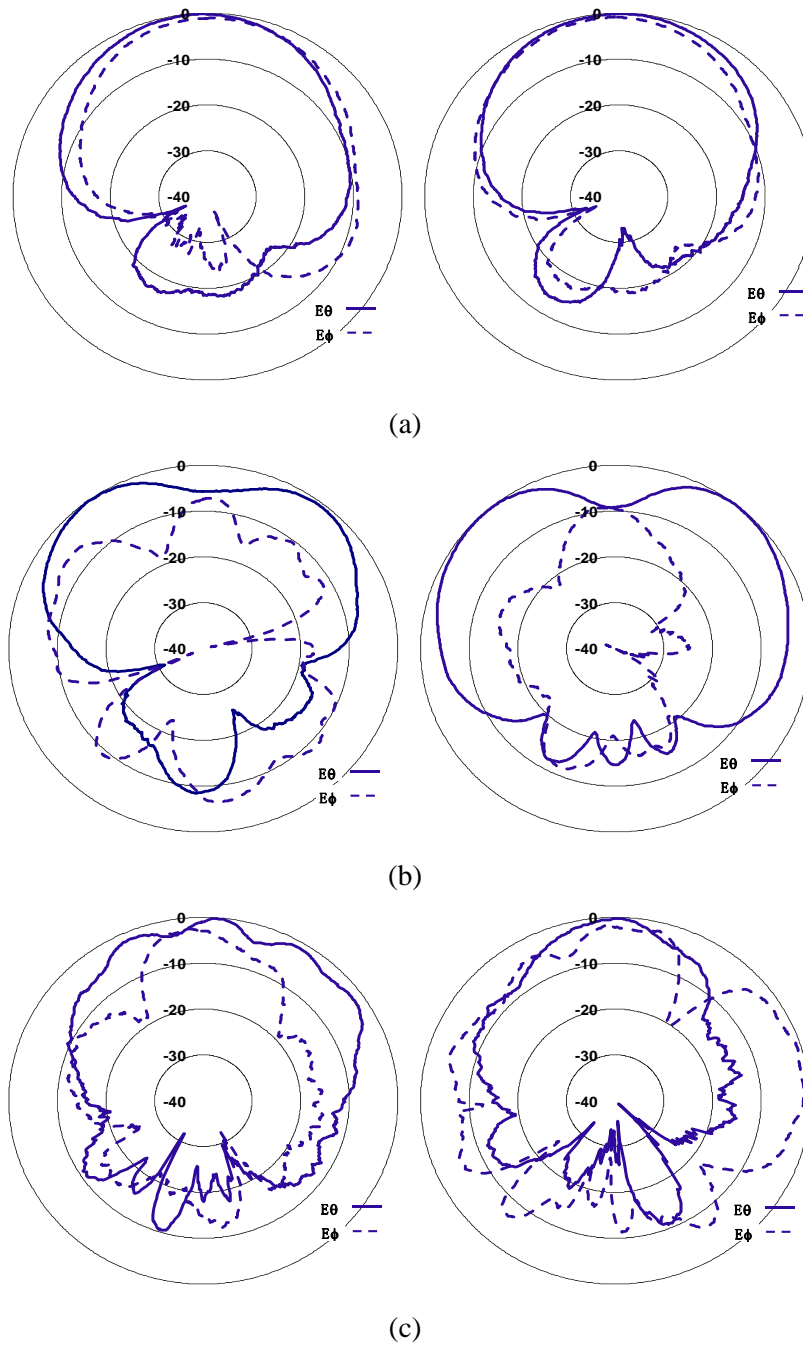
Figure 4.22   The normalised measured total far zone E field (Left: φ=0 and Right: φ=90º) (a) 2 GHz (b) 6 GHz (c) 10 GHz

(a)   (b)
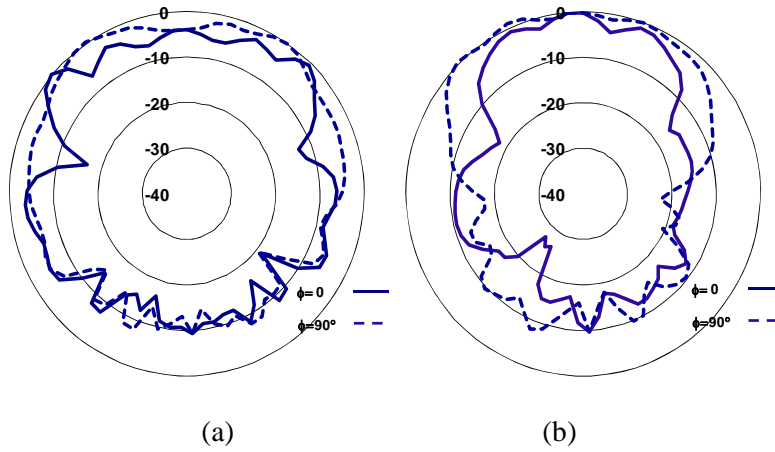
Figure 4.23   The normalised simulated total far zone E field (a) 14 GHz (b) 18 GHz

Figure 4.22 shows the normalised measured E_ϕ and E_θ at 2, 6 and 10 GHz in both ϕ=0 and 90° cut planes. At 6 GHz, as shown in Figure 4.24 (b), Eϕ at both ϕ cut planes has narrow beamwidth. Figure 4.23 only shows the simulated far zone radiated field at 14 GHz and 18 GHz without measured results because the power received from the antenna was not strong enough to accurately portray the radiation pattern. The simulated results show fairly smooth radiation patterns, however backward radiation is fairly strong due to the horizontal balun underneath and the clearance in the small ground plane.

ϕ=0 ϕ=90°

(a)

ϕ=0 ϕ=90°

(b)

82

$\phi=0$ $\phi=90º$

(c)
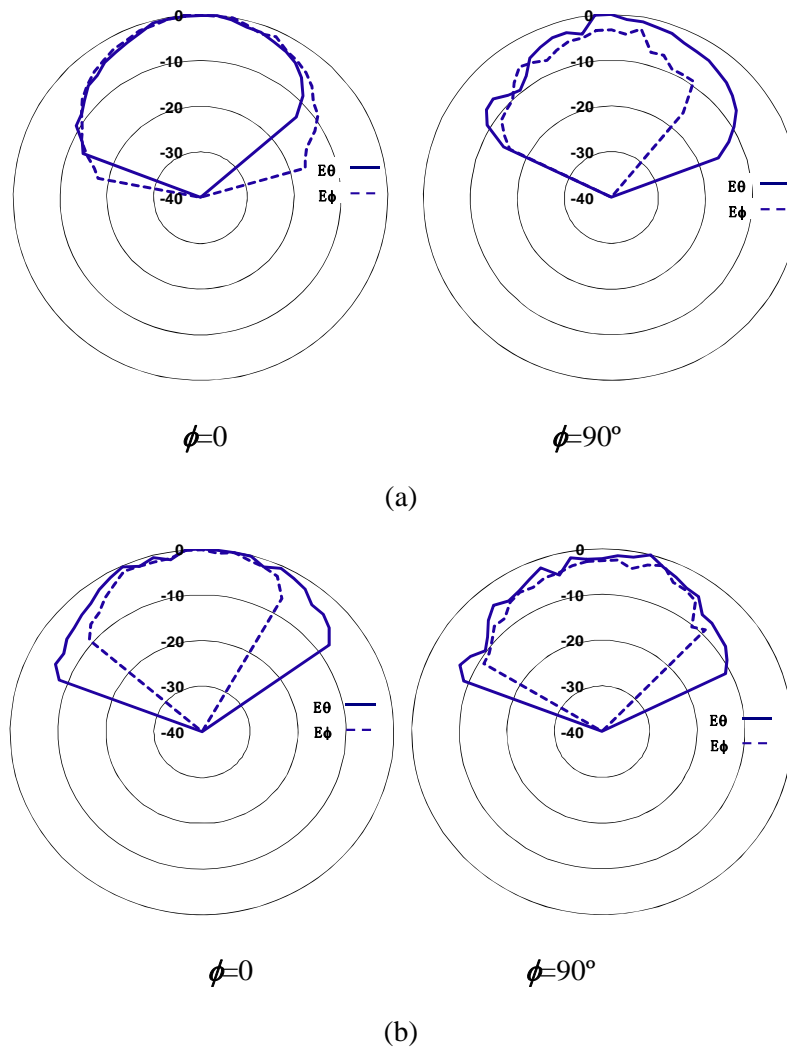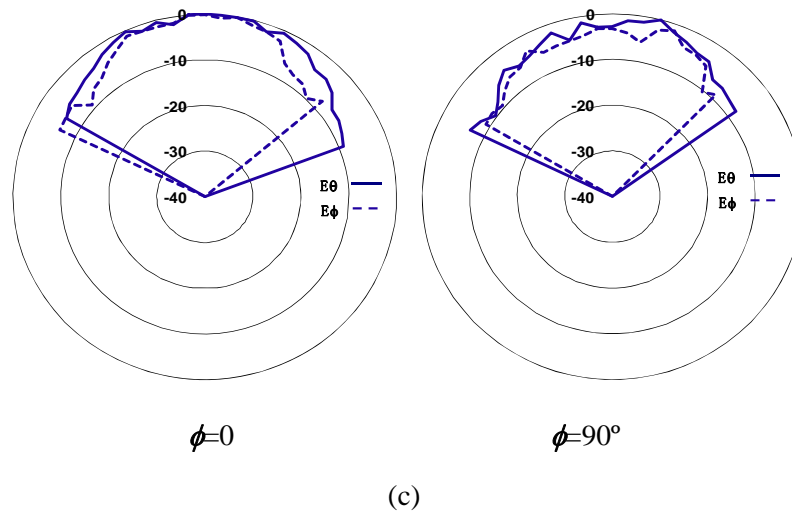
Figure 4.24   The normalised measured radiation patterns of the nested antenna system (a) 30 GHz (b) 35 GHz (c) 40 GHz

Figure 4.24 shows E_ϕ and E_θ at $\phi=0$ and 90º cut planes at three frequencies: 30 GHz, 35 GHz and 40 GHz. There was no strong signal received while the antenna model was being measured with azimuth angle θ within -80º to 80 º. Their values are similar to the background noise which is -40 dB after normalised. These radiation patterns are fairly smooth with fewer ripples even than the radiation pattern of Antenna I at much lower frequencies. They all have good circularly polarised characteristics especially at 30 GHz in $\phi=0$ cut plane E_ϕ and E_θ are very similar thus the corresponding axial ratio is very low for $\phi=0$ and a very broad range of azimuth angle θ. The main lobe of E_θ has fairly wide beamwidth at 30 GHz, 35 GHz and 40 GHz for both ϕ cut planes. Meanwhile the slight asymmetry in radiation patterns was observed. The asymmetry was caused by the asymmetric configuration of the entire antenna system and the location where Antenna II is nested to the system was far off the centre. Due to setup restrictions the results are presented only within $\pm45^0$ rotation angles.

4.5 Summary

A nested antenna system was designed and fabricated. The measured results of Antenna I showed that it achieved 9:1 impedance bandwidth, reasonable antenna gain and good radiation patterns. However, Antenna II has not achieved the satisfactory impedance bandwidth due to the mismatch between the feeding facility and the spiral antenna. In addition, asymmetry of the horizontal balun cause an asymmetry in the radiation patterns, and the discontinuity in the structure of the stepped ground plane also distorted the radiation.

The solution to solve the asymmetry of the horizontal balun is to develop another compact balun to replace the current balun of Antenna I. In order to avoid the discontinuity of the stepped ground plane the small conducting plane may be removed, however, the decision should be made based on the performance of the spiral after the symmetric balun is developed and introduced.

Chapter 5 Conclusions

Chapters 2 - 4 introduce the entire research and development process of this novel low profile ultra wideband nested antenna system containing Antenna I and Antenna II. Antenna I is a dual arm equiangular spiral with a compact balun designed for 2 - 18 GHz and Antenna II is a dual arm Archimedean spiral backed by a cavity operating on the range of 30 – 40 GHz. In Chapter 2 the structural parameter study initially introduced impedance profile (thin film resistive layer) to remove standing wave characteristic to expand impedance bandwidth of microstrip spirals. In Chapter 3, the investigations into the radiation performance of microstrip equiangular spiral antennas are conducted in both the time domain and frequency domain. In the time domain, the analysis about the current density distribution on the equiangular spiral arms revealed and visualised the radiation physics. As a result, six chip resistor loading rules for microstrip equiangular spiral antennas are generalised. In the frequency domain, over the frequency range of 2 – 18 GHz the relationship between the structural parameters and the antenna performances are explored by simulating a set of spirals. Two spiral antennas with the embedded chip resistors are developed. Finally, in chapter 4 Archimedean spirals are studied in different scenarios (in free space/on dielectric substrate/on grounded substrate) in the frequency domain over the frequency range of 30 – 40 GHz. Antenna II is nested into Antenna I system forming the nesting configuration.

5.1 Design and fabrication of low profile broadband antennas

The initial attempt to achieve a low profile wide impedance bandwidth microstrip spiral utilised a Thin Film Resistive Layer (TFRL) to attenuate the residual current on the spiral arms. The simulation and fabrication techniques of TFRL incorporated with microstrip spirals were explored and implemented. Due to the difficulties in simulating and fabricating an accurate model of a microstrip spiral with a TFRL, the investigation was stopped. However the attempt in TFRL application proved that impedance profile loading is able to expand the impedance bandwidth effectively and current distribution analysis may be used as the guidance of placing impedance loading to micrsotrip antennas efficiently.

The microstrip spiral antenna has standing wave characteristics at low frequencies. Chip resistor loading was proposed to change these resonant properties into broadband travelling wave characteristics. Chip resistor loading rules were deduced from the spiral investigations in the time domain. After validating the simulation and fabrication of spiral model with chip resistor loading, two dual-arm equiangular spiral antennas with embedded chip resistors were developed and measured. The measured return loss, gain and radiation patterns showed that they were promising options to replace the standard cavity backed design, particularly the spiral with an embedded balun. Nevertheless, the distortion in radiation pattern due to the generated surface wave propagating on substrate remained. Three tapered baluns, one vertically and the other two horizontally oriented, were developed to feed the dual arm equiangular spirals, as well as providing an impedance match between 50 Ω and 130 Ω. The compact horizontally-oriented baluns, either embedded in the substrate or located underneath the ground plane,

greatly reduced the height of the overall antenna system and performed similarly, as compared to the vertical balun.

To minimise the surface wave issues in the Ka band, Antenna II is prototyped as a dual-arm Archimedean spiral antenna on thin dielectric material backed by a cavity. For the intended frequency range, 30-40 GHz, the size of cavity does not add extra dimension beyond that of the substrate thickness for Antenna I. The balun, in charge of providing the spiral with balanced source, is designed as a tapered semi-rigid cable where the outer conductor was removed gradually until it reduced to the diameter of the inner conductor. This balun transforms characteristic impedance from 50 Ω at K-connector to 130 Ω at the feed point. Although the measured results of Antenna II showed irregularities to the simulated results (in return loss and antenna gain), the measured radiation patterns showed wide main lobes without evident ripples.

5.2 Nested antenna system

The nested antenna system integrated Antenna I and Antenna II to one entity to make it operate in dual wide bands through the one aperture. It also has low volume and low weight with minimum coupling between the components. Antenna I was a dual arm equiangular spiral with chip resistors and horizontally-oriented balun. Antenna II, together with its cavity, was placed in the substrate of Antenna I partly protruding from the ground plane. An EBG array at the edge of the dielectric substrate was used to stop the propagation of surface waves within 12 – 18 GHz. The nested antenna system was fabricated and measured. The measured results of Antenna I showed that it achieved 9:1 bandwidth (2 – 18 GHz) and good gain performance. Antenna II didn't fully achieve satisfactory impedance bandwidth from 30 - 40 GHz. The configuration and fabrication of the nested antenna system is very complicated. It is believed that four factors are affecting its performance. The first one is that the small conducting plane between the two dielectric layers made abrupt discontinuity in the large ground plane. The second factor is the inaccuracy in fabrication (due to the small dimensions) of the cavity and balun of Antenna II causing an impedance mismatch between the balun and the antenna. A third possible reason is the asymmetry of the balun for Antenna I and asymmetric mounting configuration of Antenna II (it is mounted far away from the centre of the system) may cause asymmetry in the radiation patterns over both the frequency ranges.

5.3 Future work

It is feasible to improve the fabricated antenna models.In addition to the problems summarised in Section 5.1 and 5.2, as mentioned in 5.3 the radiation efficiencies of the fabricated microstrip spiral antennas over the low frequency range were very low due to energy loss in the chip resistors and energy transmitted inside the grounded substrate. This is a problem inherent to the microstrip antenna family. In addition, it should be restated that surface waves generated by dielectric material distorted radiation patterns of the spirals especially for frequencies beyond 10 GHz. Because of the low radiation efficiency the microstrip spiral antennas such as Antenna I suffered low antenna gain over 2-8 GHz. Furthermore, the axial ratio of Antenna I could also be improved further. Possible solutions to these issues are:

- If a microstrip antenna is selected as the prototype a EBG or PBG (photonic band gap) structure to replace the ground plane could be a viable option. This may mitigate energy loss due to chip resistor loading, and low radiation efficiency due to the nearby ground plane.

- To address issues associated with the compact balun, it is possible to use a multilayer coupled line structure to implement a compact, broadband balun behind the ground plane of Antenna I. This could ensure that the balun integrated into the antenna system avoids fragility and EMI problems.

- Lastly, a four arm printed spiral antenna [21] is believed to radiate almost perfect circular polarisation. It could be a potential candidate to implement the techniques in this thesis to solve high axial ratio issues.

Appendix A: Four-Point Probe Manual.

1.1 Introduction

The purpose of the 4-point probe is to measure the resistivity of any semiconductor material. It can measure either bulk or thin film specimen, each of which consists of a different expression. The derivation will be shown in this tutorial.

The 4-point probe setup used in the EECS 143 instructional lab consists of four equally spaced tungsten metal tips with finite radius. Each tip is supported by springs on the other end to minimize sample damage during probing. The four metal tips are part of an auto-mechanical stage which travels up and down during measurements. A high impedance current source is used to supply current through the outer two probes; a voltmeter measures the voltage across the inner two probes (See Figure 1) to determine the sample resistivity. Typical probe spacing s is about 1 mm.
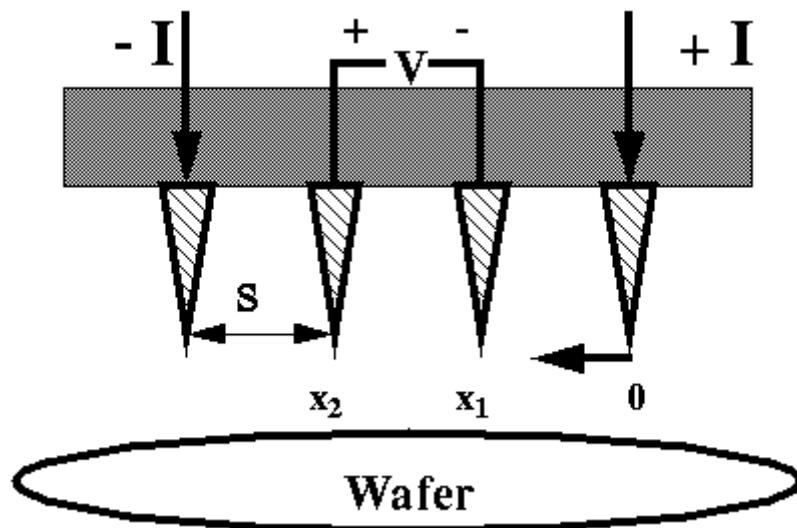
Fig. 1 Schematic of 4-point probe configuration

1.2 Theory

For a very thin layer (thickness $t \ll s$), we get current rings instead of spheres. Therefore, the expression for the area

$$A = 2\pi x t$$

The derivation is as follows:

$$R = \int_{x_1}^{x_2} \rho \frac{dx}{2\pi x t} = \int_{s}^{2s} \frac{\rho}{2\pi t} \frac{dx}{x} = \frac{\rho}{2\pi t} ln(x) \Big|_{s}^{2s} = \frac{\rho}{2\pi t} ln2$$

Consequently, for R = V/2I, the sheet resistivity for a thin sheet is:

$$\rho = \frac{\pi t}{\ln 2}\left(\frac{V}{I}\right)$$

Note that this expression is independent of the probe spacing s. Furthermore, this latter expression is frequently used for characterization semiconductor layers, such as a diffused N+ region in a p-type substrate. In general, the sheet resistivity

$$R_s = \rho / t$$

can be expressed as:

$$Rs = k\left(\frac{V}{I}\right)$$

where the factor k is a geometric factor. In the case of a semi-infinite thin sheet, k = 4.53, which is just $\pi / \ln 2$ from the derivation. The factor k will be different for non-ideal samples.

1.3 Operation Procedures

The following steps should be taken in the following sequence:

1) Turn on the voltmeter, set the mode to DC and voltage range to 200 mV.

2) Place wafer onto the probe stage.

3) Flip the toggle switch located atop the probe station from "NEUTRAL" TO "DOWN".

4) Watch the probe casing lower until the probes stabilize on the wafer.

5) Return the toggle switch of the probe station to the "NEUTRAL" position.

6) Turn on the current source by turning the black switch "S1" to the "ON" position.

7) Set the current to the desired level, and proceed with measuring the voltage across the inner two probes. Map the wafer.

8) When measurement is finished, shut off the current source by turning the switch "S1" to the "OFF" Position.

9) Flip the probe station toggle switch from "NEUTRAL" to "UP".

10) Wait until the probe casing is all the way up, then set the toggle switch back to "NEUTRAL".

11) Turn off voltmeter.

James Chan, Spring 1994
The University of California

Appendix B: Fabrication procedures.

1. cut a board of Roger Duroid5880 (of thickness 3.175 mm) with requested dimensions (blue photo resist on both sides)

2. expose one side of the board with a negative film covering for 70 seconds

3. expose the other side of the board for 70 seconds

4. leave the exposed board in the developer solution for 3~5 minutes

5. brush back and forth with a soft brush until the photo resist in the exposed area being removed

6. place the board in the etching tank until all exposed copper is removed

7. leave the board in the stripper solution for 3~5 minutes

8. scrub with a hard brush until all remained photo resist is removed

9. so far the antenna with cut and copper ground plane underneath has been gained

10. spin photo resist AZ1512 on the antenna side

11. bake it at 90°C for 20 minutes

12. expose the TFRL (thin film resistive layer) area with a negative film over the antenna side under UV(ultraviolet) light for 20 seconds

13. remove the photo resist in TFRL area with developer solution AZ400K for 20 seconds

14. bake it at 110°C for 20 minutes

15. deposit 20 nm NiCr on antenna side using e-beam technology in vacuum room

16. wash away the unwanted TFRL which is on photo resist with Acetone

17. drill a hole of diameter 0.4 mm using micro-driller

18. make the impedance transition line on Roger Duroid5880 with thickness of 0.508 mm and dimensions of 30 mm×100 mm(copper ground plane underneath as well)

19. solder the antenna board, transition board and coaxial line connector together

Reference

[1] Roy, A.; Ghosh, S.; Chakrabarty, A., "Radiating element characteristics effect on the scanning performance of phased array antenna for tracking purpose" , *Industrial and Information Systems, 2nd International Conference,* 2007, pp.175 – 180

[2] Zmuda, H.; Toughlian, E.N.; Payson, P.; Klumpe, H.W., III, "A photonic true time delay processor for Global Positioning System (GPS) null steering", *Aerospace Conference, IEEE Proceedings.*, Vol.5, 1998, pp.311 – 317

[3] Balanis, Constantine A., " Antenna theory : analysis and design", Hoboken, NJ : John Wiley, 2005

[4] Dyson, J., "The equiangular spiral antenna", *IRE Transactions on Antennas and Propagation*, Vol.7, No.2, 1959, pp. 181 – 187

[5] Kaiser, J. "The Archimedean two-wire spiral antenna**",** *IEEE Transactions on Antennas and Propagation*, Vol.8, No.3, 1960, pp. 312 – 323

[6] Peyrot-Solis, M.A.; Galvan-Tejada, G.M.; Jardon-Aguilar, H., "State of the art in ultra-wideband antennas", *Electrical and Electronics Engineering, 2nd International Conference,* 2005, pp.101 – 105

[7] Bialkowski, Marek E, "Modelling of Planar Radial-guide Antennas", *14th International Conference on Microwaves, Radar and Wireless Communications*, Vol.1, 2002, pp.205 – 217

[8] V.H. Rumsey, "Frequency independent antennas", Academic Press, 1966

[9] Mayes, P. E.; Deschamps, G. A.; Patton, W. T., "Backward wave radiation from periodic structures and application to the design of frequency-independent antennas," *Proc. IRE,* Vol.49, 1961, pp. 962 – 963

[10] Dyson, J.D.; Bawer, R.; Mayes, P.E.; Wolfe, J.I., "A Note on the Difference Between Equiangular and Archimedes Spiral Antennas (Correspondence)", *IRE Transactions on Microwave Theory and Techniques,* Vol.9, Issue 2, 1961, pp. 203 – 205

[11] Khalil, K.; Abd-Alhameed, R.A.; Excell, P.S., "Dual-band quadrifilar square spiral antenna for satellite-mobile handsets", *(ICAP 2003). 12th International Conference on Antennas and Propagation,* Vol.1, 2003, pp.186 – 189

[12] Gschwendtner, E.; Wiesbeck, W. , "Ultra-broadband car antennas for communications and navigation applications", *IEEE Transactions on Antennas and Propagation*, Vol.51, No. 8, 2003, pp.2020 – 2027

[13] Morgan, T., "Spiral antennas for ESM", *Antennas and Propagation Society International Symposium*, Vol.24, No.6, 1986, pp.777 – 780

[14] Nikawa, Y.; Shima, M.; Mori, S.; Okada, F., "A Flexible Spiral Antenna for Medical Application", *Microwave Conference, APMC '92*, Vol.1, 1992, pp.217 – 220

[15] Penno, R. P. ; Pasala, K. M., "Angle Estimate with a Multi-Arm Spiral Antenna," *IEEE Aerospace Conference Proceedings*, Vol.3, No.3, 1999, pp. 6 – 13

[16] van Genderen, P.; Nicolaescu, L.; Zijderveld, J., "Some experience with the use of spiral antennas for a GPR for landmine detection", *International Radar Conference Proceedings*, 2003, pp. 219 – 223

[17]   Sego, D.J., "Ultrawide band active radar array antenna for unmanned air vehicles", *IEEE National Telesystems Conference Proceedings*,1994, pp.13 – 17

[18]   Chang, Dau-Chryh; Lee, Hisn-Chung; Lee, Shih-Hung, "The study of spiral antenna for radar imaging", *4th International Conference on Microwave and Millimeter Wave Technology Proceedings*, 2004, pp.11 – 13

[19]   Shively, D., "Spectral Domain Analysis of Square Spiral Microstrip Antennas", *IEEE Antennas and Propagation Society International Symposium*, 1993, pp. 1466 – 1468

[20]   Volaskis, J.L.; Nurnberger, M.W.; Filipovic, D.S., "A broadband cavity-backed slot spiral antenna", *IEEE Transactions on Antennas and Propagation*, Vol.43, No.6, 2001

[21]   Corzine,R.G. ; Mosko, J.A., "Four-Arm Spiral Antennas",Norwood, MA, Artech House, 1990

[22]   Muller, D.J.; Sarabandi, K., "Design and Analysis of a 3-Arm Spiral Antenna", *IEEE Transactions on Antennas and Propagation,*Vol.55, No.2, 2007, pp.258 – 266

[23]   Stinehelfer, H.E., "Microstrip Distortion Analysis", *ARFTG Conference Digest-Spring, 19th ARFTG*, Vol.1, 1982, pp.108 – 110

[24]   Albani, M.; Menniti, F.; Schippers, H.; Maci, S., "Pattern distortion for patch antennas on finite and faceted ground planes", *IEEE Antennas and Propagation Society International Symposium*, Vol.1, 2002, pp. 770 – 773

[25]   Song, Zhaohui; Liu, Meijia; Ding, Zhiyong, "An improved design of microstrip Archimedeam spiral antenna" , *International Conference on Microwave and Millimeter Wave Technology, 2007*, pp. 1 – 4

[26]   Wang, J. J. H.; Tripp, V. K., "Design of Multioctave Spiral-mode Microstrip Antennas", *IEEE Transactions on Antennas and Propagation*, Vol.39, No.3, 1991, pp. 332 – 335

[27]   R.SIVAN-SUSSMAN, "Various modes of the equiangular spiral antenna", *IEEE Transactions on Antenna and Propagation*, 1963, pp.533 – 539

[28]   Huffman, Julie A.; Cencich, Tom, "Modal impedances of planar, non-complementary, N-fold symmetric antenna structures", *IEEE Antennas and Propagation Magazine*,Vol 47, No.1,2005, pp.110 – 116

[29]   Dyson, J., "The unidirectional equiangular spiral antenna", *IEEE Transactions on Antennas and Propagation,* Vol.7, No.4, 1959, pp. 329 – 334

[30]   Nakano, H.; Nogami, K.; Arai, S.; Mimaki, H.; Yamauchi, J., "A spiral antenna backed by a conducting plane reflector**,** *IEEE Transactions on Antennas and Propagation,[legacy, pre – 1988]*, Vol.34, No.6, 1986, pp.791 – 796

[31]   Filipovic, D.S.; Siah, E.S.; Sertel, K.; Liepa, V.V.; Volakis, J.L., "A thin broadband cavity-backed slot spiral antenna for automotive applications", *IEEE Antennas and Propagation Society International Symposium,* Vol.1, 2001, pp.414 – 417

[32]   Acree, M.A.; Prata, A., Jr., "Archimedean spiral-mode microstrip antenna with improved axial ratio", *IEEE Antennas and Propagation Society International Symposium*, Vol.2, 1999, pp.1232 – 1235

[33]   Afsar, M.N.; Wang, Yong; Hanyi, D.A, " New wideband cavity-backed spiral antenna", *IEEE Antennas and Propagation Society International Symposium*, Vol.4, 2001, pp.124 – 127

[34]   Buck, M.C.; Filipovic, D.S., "Unidirectional spiral antenna with improved gain and WoW", *IEEE Antennas and Propagation Society International Symposium,* Vol.3A, 2005, pp. 541 – 544

[35]   Filipovic, D.S.; Siah, E.S.; Sertel, K.; Liepa, V.V.; Volakis, J.L, "A thin broadband cavity-backed slot spiral antenna for automotive applications", *IEEE Antennas and Propagation Society International Symposium*, Vol.1, 2001, pp. 414 – 417

[36]   Wang, J.J.H.; Tillery, J.K.; Acree, M.A, "Multioctave wideband mode-0 operation of spiral-mode microstrip antennas", *IEEE Antennas and Propagation Society International Symposium,* 1997 Digest, Vol.3, pp.1860 – 1863

[37]   Wang, J.J.H.; Hopkins, G.D.; Tripp, V.K. , "A new class of wideband low-profile, conformal antennas-its impact to wireless telecommunications", *Wireless Communications, 1992. Conference Proceedings., IEEE International Conference on Selected Topics* , 1992, pp.115 – 117

[38]   Li, R., Ni., G., "Numerical Analysis of 4-arm Archimedian Printed Spiral Antenna", *IEEE Transactions on Magnetics*, Vol 33, No. 2, 1997, pp.1512 – 1515

[39]   Schreider, L; Begaud, X.; Soiron, M.; Perpere, B., "Archimedean microstrip spiral antenna loaded by chip resistors inside substrate", *IEEE Antennas and Propagation Society International Symposium*, Vol.1, 2004, pp. 1066 – 1069

[40]   McFadden,M.; Scott Jr.,W.R., "Analysis of the Equiangular Spiral Antenna on a Dielectric Substrate", *IEEE Transactions on Antennas and Propagation*, Vol.55, No.11, 2007, pp. 3163 – 3171

[41]   Garg, Ramesh, " Microstrip antennas design handbook", Boston, MA : Artech House, 2001

[42]   Lai, Qinghua; Almpanis, G.; Fumeaux, C.; Benedickter, H.; Vahldieck, R., "Comparison of the Radiation Efficiency for the Dielectric Resonator Antenna and the Microstrip Antenna at Ka Band", *IEEE Transactions on Antennas and Propagation,* Vol.56, No.11, 2008, pp.3589 – 3592

[43]   Sabban, A., "A comprehensive study of losses in MM-wave microstrip antenna arrays", *27th European Microwave Conference, 1997*, Vol.1, pp. 163 – 167

[44]   Wang, H., Ji, Y., Hubing, T.H., Drewniak, J.L., van Doren, T.P.; DuBroff, R.E, "Experimental and numerical study of the radiation from microstrip bends," *IEEE International Symposium on Electromagnetic Compatibility,* Vol.2, No.8, 2000, pp. 739 –741

[45]   Nakano, H.; Tsuchiya, N.; Suzuki, T.; Yamauchi, J., "Loop and spiral line antennas at microstrip substrate surface", *Sixth International Conference on Antennas and Propagation,* 1989, pp.196 – 200

[46]   Champagne, Nathan J.; Williams, Jeffery T .; Wilton, Donald R. , "The Use of Curved Segments for Numerically Modeling Thin Wire Antennas and Scatterers", *IEEE Transactions on Antennas and Propagation*, Vol.40, No.6, 1992, pp. 682 – 689

[47]   He, Mang He; Xu, Xiaowen, "Maxwellian circuit models for analysis of printed spiral antennas", *IEEE Microwave and Wireless Components Letters,* Vol.15, No.11, 2005, pp. 769 – 771

[48]   Fumeaux, C.; Baumann, D., Vahldieck, R., "Finite-Volume Time-Domain Analysis of a Cavity-Backed Archimedean Spiral Antenna", *IEEE Transactions on Antennas and Propagation*, Vol.54, No. 3, 2006, pp. 844 – 851

[49]   Nakano, H.; Yasui, H.; Yamauchi, J., "Numerical analysis of two-arm spiral antennas printed on a finite-size dielectric substrate", *IEEE Transactions on Antennas and Propagation,* Vol.50, No.3, 2002, pp.362 – 370

[50]   Harrington, R.F., "Time-Harmonic Electromagnetic Fields" , New York, McGraw-Hill,1961

[51]   *S. B. de Assis Fonseca, A. J. Giarola,* "Microstrip Disk Antennas, Part 11: The Problem of Surface Wave Radiation by Dielectric Zkuncation", *IEEE Transactions on Antennas and Propagation*, Vol.32, No. 6, 1984, pp. 568 – 573

[52]   Bhattacharyya, A. K., "Effects of Ground Plane and Dielectric Truncations on the Efficiency of a Printed Structure", *IEEE Transactions on Antennas and Propagation*, Vol.39, No. 3, 1991, pp. 303 – 308

[53]   Schuster, C.; Fichtner, W., "Numerical analysis of surface waves on a grounded dielectric plane using the finite difference time domain method", *Electrical Performance of Electronic Packaging*, 1999, pp. 95 – 98

[54]   Bell, Jodie M.; Iskander, Magdy F, "A Low-Profile Archimedean Spiral Antenna Using an EBG Ground Plane", *IEEE Antennas and Wireless Propagation Letters*, Vol.3, 2004, pp.223 – 226

[55]   Leung, W.Y.; Biswas, R.; Cheng, Shi-Di; Sigalas, M.M.; McCalmont, J.S.; Tuttle, G.; Ho, K.-M,."Slot antennas on photonic band gap crystals", *IEEE Transactions on Antennas and Propagation,* Vol.45, No.10, 1997, pp. 1569 – 1570

[56]   F. Yang, and Y. Rahmat-Samii, "Microstrip antennas integrated with electromagnetic band-gap structures: a low mutual coupling design for array applications", *IEEE Transactions on Antennas and Propagation*, Vol.51, 2003, pp. 2936–2946

[57]   Sabbagh, Mahmoud A. El; Mansour, R., " Ultra-Wide Suppression Band of Surface Waves Using Periodic Microstrip-Based Structures, *IEEE Transactions on Microwave Theory and Techniques*, Vol.56, No. 3, 2008, pp.671–683

[58]   Wang, Chao; Yuan, Nao-chang, "The Application of HIS in Planner Spiral Antenna", *Radar CIE '06 International Conference* , 2006, pp. 1 – 4

[59]   Liu, T.H.; Zhang, W.X.; Zhang, M.; Tsang, K.F., "Low profile spiral antenna with PBG Substrate", *Electronics Letters*, Vol. 36, No.9, 2000

[60]   Zbay, E. O.; Michel, E.; Tuttle, G.; Biswas, R.; Ho, K. M.; Bostak, J.; Bloom, D. M., "Terahertz spectroscopy of three-dimensional photonic band gap crystals," *Opt. Lett.,* Vol. 19, 1994, pp. 1155

[61]   Chen, Hong-Twu, "Compact circular microstrip antenna with embedded chip resistor and capacitor", *IEEE Antennas and Propagation Society International Symposium*, Vol.3, No.6, 1998, pp.1356 – 1359

[62]   Nakano, H.; Mimnaki, H.; Yamauchi, J.; Hirose, K., "A low profile Archimedean spiral antenna", *IEEE Antennas and Propagation Society International Symposium, AP-S. Digest* ,Vol.1, 1993, pp. 450 – 453

[63]   Carver, Keith R.; Mink, James W., "Microstrip antenna technology", *IEEE Transaction on Antennas and Propagation*, Vol.AP-29, No.1, 1981

[64]   Alexopoulos, Nicolaos G.; Katehi, Pisti B.; Rutledge, D.B., "Substrate Optimization for Integrated Circuit Antennas", *IEEE Transactions on Microwave Theory and Techniques*, Vol.31, No. 7, July 1983

[65]   http://www.rogerscorp.com/acm/products/10/RT-duroid-5870-5880-Glass-Microfiber-Reinforced-PTFE-Composites.aspx

[66]   http://www.rogerscorp.com/documents/726/acm/RO4000-laminates-data-sheet-and-fabrication-guidelines-RO4003C-RO4350B.aspx

[67]   Bawer,R.; Wolfe, J. J., "The spiral antenna", *IRE International Convention Record*, Vol. 8, Part 1, 1960, pp. 84 – 95

[68]   Nakano, H.; Kikkawa, K.; Yamauchi, J., "A low-profile equiangular spiral antenna backed by a cavity with an absorbing strip", *Antennas and Propagation, EuCAP 2006 First European Conference* , 2006, pp.1 – 5

[69]   Zandman, F., "Resistor theory and technology", Park Ridge, N. J. SciTech Pub., c2000

[70]   Mola, D. Di; Brioschi, L.; Carrera, A.; Fusari, F., Lenzi, M.; Ongaro, G, "Unstressed Nickel Chromium Thin Films for Thermo-Optic Application", *Optoelectronic and Microelectronic Materials Devices Conference Proceedings* , 1998, pp.411 – 414

[71]   Email correspondence regarding thick film resistive paste

[72]   "Numerical solution of initial boundary value problems involving Maxwell's equation in isotropic media", 1966

[73]   Bluhm, Thomas, "Resistors in Microwave Applications", *Capacitor and Resistor Technology Symposium*, 1997

[74]   Laurich, W., "SMD Resistors Beyond UHF", *CARTS –EUROPE* , 1990, pp.41

[75]   Datasheet of MMU 0102 HF, MMA 0204 HF, MMB 0207 HF, Vishay company, "http://www.vishay.com/docs/28718/melfhf.pdf"

[76]   Datasheet of MCT 0603HF,Vishay company, "http://www.vishay.com/docs/ 28712/mct0603h.pdf"

[77]   Chramiec, Jerzy; Kitlinski, Marek, "Computer aided modeling of resistors used in MICs", pp. 496 – 499

[78]   Duncam, J.W.; Minerva, V.P., "100:1 bandwidth balun tranformer", *Proc. IRE*, Vol.48, 1960, pp.156 –164

[79]   Oltman, G., "The Compensated Balun", *IEEE Transactions on Microwave Theory and Techniques,* Vol.14, 1966, pp.112–119

[80]   Gans,M.; Kajfez, D.; Rumsey, R.H., "Frequency independent balun", *Proc. IEEE*, Vol.53, No.9, 1965, pp.647–648

[81]   Guo, Y.X.; Zhang, Z.Y.; Ong, L.C.; Chia, M.Y.W., "A New Balanced UWB Planar Antenna", *Wireless Technology, The European Conference*, 2005, pp.515–517

[82]   Lin, Yo-Shen; Chen, Chun Hsiung, "Lumped-Element Impedance-Transforming Uniplanar Transitions and Their Antenna Applications", *IEEE Transactions on Microwave Theory and Techniques*, Vol.52, No.4, 2004, pp.1157–1165

[83]   Mao, Shau-Gang; Hwang Chieh-Tsao; Wu, Ruey-Beei; Shen, Chun Hsiung, "Analysis of Coplanar Waveguide-to-Coplanar Stripline Transitions", *IEEE Transactions on Microwave Theory and Techniques*, Vol.48, No.1, 2000, pp. 23 – 29

[84]   Chung, Kyungho; Pyun, Sungho; Choi, Jaehoon, "Design of an Ultrawide-Band TEM Horn Antenna with a Microstrip-Type Balun", *IEEE Transactions on Antennas and Propagation*, Vol.53, No.10, 2005, pp. 3410 – 3413

[85]   Puglia, K.V., "Application notes: Electromagnetic simulation of some common balun structures", *IEEE Microwave Magazine*, No. 9, 2002, pp.56–61

[86]   Ghosh, D.; De, A.; Taylor, M.C.; Sarkar, T.K.; Wicks, M.C.; and Mokole, E., "Transmission and Reception by Ultra Wideband (UWB) Antennas", *IEEE Antennas and Propagation Magazine*, Vol.48, No. 5, October 2006., pp.67–99

[87]   "Microwave Engineering Online," http://img.cmpnet.com/edtn/europe/mwee/pdf/CAD.pdf, Jul. 2001

[88]   Yang, Li; Fan, Mingyan; Feng, Zhenghe, "A Spiral Electromagnetic Bandgap (EBG) Structure and its Application in Microstrip Antenna Arrays", *IEEE Asia Pacific Conference Proc.* 2005, Vol.3, pp.4

[89]   Fan, M.Y.; Hu, R.; Feng, Z.H.; Zhang, X.X.; Hao, Q., "Advance in 2D-EBG research", *J Infrared Millimeter Waves*, Vol.22, No.2, 2003

Publications

Fu, W.; Lopez, E.R.; Rowe, W.S.T., Ghorbani, K., "A Planar Dual-Arm Equiangular Spiral Antenna", , *IEEE Transactions on Antennas and Propagation*, Volume: 58 , Issue: 5, pp. 1775-1779. 2010.

E. R. Lopez, W. Fu, W. S. T. Rowe, K. Ghorbani, and A. Mitchell "Reconfigurable two-arm spiral antenna microwave photonic polarization diversity techniques", *Photonics Technology letters,* Vol. 21, No. 22, pp. 1668-1670, 2009.

Fu, W., Lopez, E.R.; Rowe, W.S.T.; Ghorbani, K., "A compact broadband spiral antenna", *Asia-Pacific Microwave Conference*, APMC 2008. Asia-Pacific, .

Fu, W., Lopez, E.R.; Scott, J., Rowe, W.S.T., Ghorbani, K., "Broadband Equiangular Spiral Antenna with Embedded Chip Resistors", *Asia-Pacific Microwave Conference*, pp 2059-62, APMC 2007.

Lopez, E.R., Lunn, T.; Fu, W., Ghorbani, K., Rowe, W.S.T., Mitchell, A., "Ultra-broadband Photonic Antenna System with Microwave Photonic Combination", *Asia-Pacific Microwave Conference*, pp. 2733-36, APMC2007.